1-30-2009

Paramagnetic resonance studies of bistrispyrazolylborate cobalt(II) and related derivatives

William Myers

William K. Myers
Candidate

Chemistry and Chemical Biology
Department

This thesis is approved, and it is acceptable in quality and form for publication on microfilm:

Approved by the Dissertation Committee:

, Chairperson

Accepted:

Dean, Graduate School

Date

Paramagnetic Resonance Studies of *Bis*trispyrazolylborate Cobalt(II) and Related Derivatives

BY

William K. Myers

B.A., Chemistry, Carleton College, 2003

Dissertation

Submitted in Partial Fulfillment of the
Requirements for the Degree of

Doctor of Philosophy
Chemistry

The University of New Mexico
Albuquerque, New Mexico

December, 2008

DEDICATION

In memoriam, Clifford Myers, 1900-1987

My grandfather graduated Summa Cum Laude with an A.B., Chemistry from Yale University, 1922S. He pursued a lifelong career in paper chemistry at Hollingsworth & Whitney, later becoming Scott Paper Co., subsidiary, Winslow, ME.

ACKNOWLEDGEMENTS

Many people have assisted me in the years leading up to this dissertation. First and foremost my advisor, Professor David Tierney, has generously funded and motivated what I have accomplished. Dr. Eiichi Fukushima and Dr. Andrew McDowell of Albuquerque Magnetic Resonance worked closely with me on several occasions to explain the construction and testing of NMR probes. Likewise, Dr. Karen Ann Smith has been a constant resource for insight and suggestions relating to my NMR research. For all things electromagnetic, my brother, John P. Myers, currently a Senior Design Engineer at Linear Technologies, Milpitas, CA, has taught essential principles and offered suggestions for the development of ENDOR instrumentation. Professor Brian Bennett of the Medical College of Wisconsin allowed me use of a Bruker BioSpin ELEXSYS X-Band ENDOR setup at the National Biomedical EPR Center. The help of Professor Charles Scholes of SUNY-Albany cannot be overstated. He helped resolve key issues regarding the NMR component of ENDOR cavities, provided one of his own Q-Band resonators for use at UNM, and granted me a position in his laboratory as a Visiting Research Scholar, starting March 1, 2008. Dr. Peter Doan of Northwestern University was helpful in explaining the implementation of pulse RF/CW ENDOR in the laboratory of Professor Brian Hoffman. Among many in the laboratory, I had the pleasure of working with Mr. R. "Matt" Breece, who has been a great partner in obtaining and analyzing EXAFS data at Brookhaven National Laboratory.

Were it not for the background of 15 months of research experience at Los Alamos National Laboratory, I would likely not be pursuing a Ph.D. in chemistry. I am grateful for the patience, wisdom, and generosity of Dr. Mary P. Neu, her then post-doctoral researcher Dr. Christy Ruggiero, and expert chemist, Mr. Sean Riley. They taught many essential lessons in chemistry research.

These years would not have been possible without the support and encouragement of Lorena O. Gutierrez, my parents, siblings, my many friends and associates in New Mexico, and my chemistry class of 2002 at Carleton College.

Paramagnetic Resonance Studies of *Bis*trispyrazolylborate Cobalt(II) and Related Derivatives

BY

WILLIAM K. MYERS

B.A., Chemistry, Carleton College, 2003

ABSTRACT OF DISSERTATION

Submitted in Partial Fulfillment of the
Requirements for the Degree of

Doctor of Philosophy
Chemistry

The University of New Mexico
Albuquerque, New Mexico

December, 2008

Paramagnetic Resonance Studies of *Bis*trispyrazolylborate Cobalt(II) and Related Derivatives

By

William K. Myers

B.A. Chemistry, Carleton College, 2003
Ph.D. Chemistry, University of New Mexico, 2008

ABSTRACT

Herein, a systematic frozen solution electron-nuclear double resonance (ENDOR) study of high-spin Co(II) complexes is reported to demonstrate the efficacy of methyl substitutions as a means of separating dipolar and contact coupling, and further, to increase the utility of high-spin Co(II) as a spectroscopic probe for the ubiquitous, but spectroscopically-silent Zn(II) metalloenzymes. High-spin (*hs*) Co(II) has been subject of paramagnetic resonance studies for over 50 years and has been used as a spectroscopic probe for Zn metalloenzymes for over 35 years. However, as will be seen, the inherent complexity of the electronic properties of the cobaltous ion remains to be exploited to offer a wealth of information on Zn(II) enzymatic environments. Specifically, ENDOR measurements on *bis*trispyrazolylborate cobalt(II) confirm the utility of the novel method of methyl substitution to differentiate dipolar and Fermi contact couplings. An extensive set of electron paramagnetic resonance (EPR) simulations were performed. Software was developed to implement an ENDOR control interface. Finally, proton relaxation measurements were made in the range of 12-42 MHz, which were accounted for with the large *g*-value anisotropy of the Co(II) compounds. Taken as a whole, these studies point to the rich complexity of the electronic structure of high-spin cobalt(II) and, when sufficiently well-characterized, the great utility it has as a surrogate of biological Zn(II).

TABLE OF CONTENTS

LIST OF FIGURES

LIST OF TABLES

Chapter 1

Introduction

The high spin cobalt(II) ion is of intrinsic interest due to the complexity of its ground state, with unquenched orbital angular momentum, magnetic anisotropy, orbital degeneracy, and low-lying excited states. Co(II) has been utilized for catalysts, notably the recent oxygen evolving reaction using a phosphate ligand.[1] The d^7 Co(II) ion has also found utility as a spectroscopic surrogate for the ubiquitous, yet spectroscopically-silent, d^{10} Zn(II) ion metalloenzyme binding sites. Co(II) generally adopts a similar geometry, and is often catalytically active.[2] The series of bistrispyrazolylborate complexes dealt with in this dissertation are six coordinate and highly symmetric, both traits that are unlikely in Zn(II) metalloenzyme sites. However, pyrazole mimics the nitrogen coordination of the imidazole side chain of the amino acid histidine.[3] Furthermore, the coordination of one trispyrazolylborate ligand has been shown to be a good mimic for the *tris*histidine motif that is common among Zn(II) metalloenzymes.[4]

In principle, the complex nature of the Co(II) ground state ought to offer a rich source of information on the structure and bonding of Co(II) in Zn(II) sites, but this information is often difficult to extract.[2] With this in mind, the Tierney laboratory is developing the idea of integrated paramagnetic resonance, the simultaneous application of EPR, ENDOR, and NMR. Initial studies led to a simple, but robust method of connecting room temperature paramagnetic NMR shifts with the ligand hyperfine interactions observed at 4K, separating dipolar and contact hyperfine interactions with selective methyl substitution.[5] In support of this effort, the author performed electron nuclear double resonance (ENDOR) measurements at both X-band (9.4 GHz) and Q-band

(34 GHz) microwave frequencies, extensive electron paramagnetic resonance (EPR) simulations, and FT nuclear magnetic resonance (NMR) measurements in the 12-42 MHz range.

With their ease of synthesis and chemical modification, *bis*trispyrazolylborate complexes of Co(II) are an excellent choice for fundamental paramagnetic resonance studies. So extensive are the applications and derivatives of the complexes that their creator, Trofimenko, has developed a system of nomenclature that will be used in this dissertation.[3] The general formula may be stated as $LM(RNp^{x,y,z})$, where L is a generic secondary ligand, M is the central cation, R represents the substitutions on the apical borons, N is the number of pyrazoles attached to the boron, having values of B, T, or Q, where B stands for bispyrazolyl; T for trispyrazolyl; and Q for tetrakispyrazolylborate, p is pyrazolyl, and finally, *x, y, z* represent non-proton substituents on the 3-, 4-, and 5-carbons of the pyrazole rings.

The series of methyl substitutions employed in this dissertation are shown in Figure 1.1.[5] All of the nuclei (^{59}Co, ^{14}N, ^{11}B, ^{13}C (*natural abundance*), and ^{1}H) have NMR signals, and if necessary may be isotopically enriched. The three-fold symmetry of the molecule renders all six pyrazoles and the two apical borons symmetrically equivalent. The series of compounds feature a common component of six pyrazolyl nitrogens coordinating the Co(II) and six non-coordinating pyrazolyl nitrogens bound on either end by negatively charged boron atoms. The 20 protons may be substituted with methyl or alkyl groups to remove the contact coupling and make quantifiable changes to the dipolar coupling.[5]

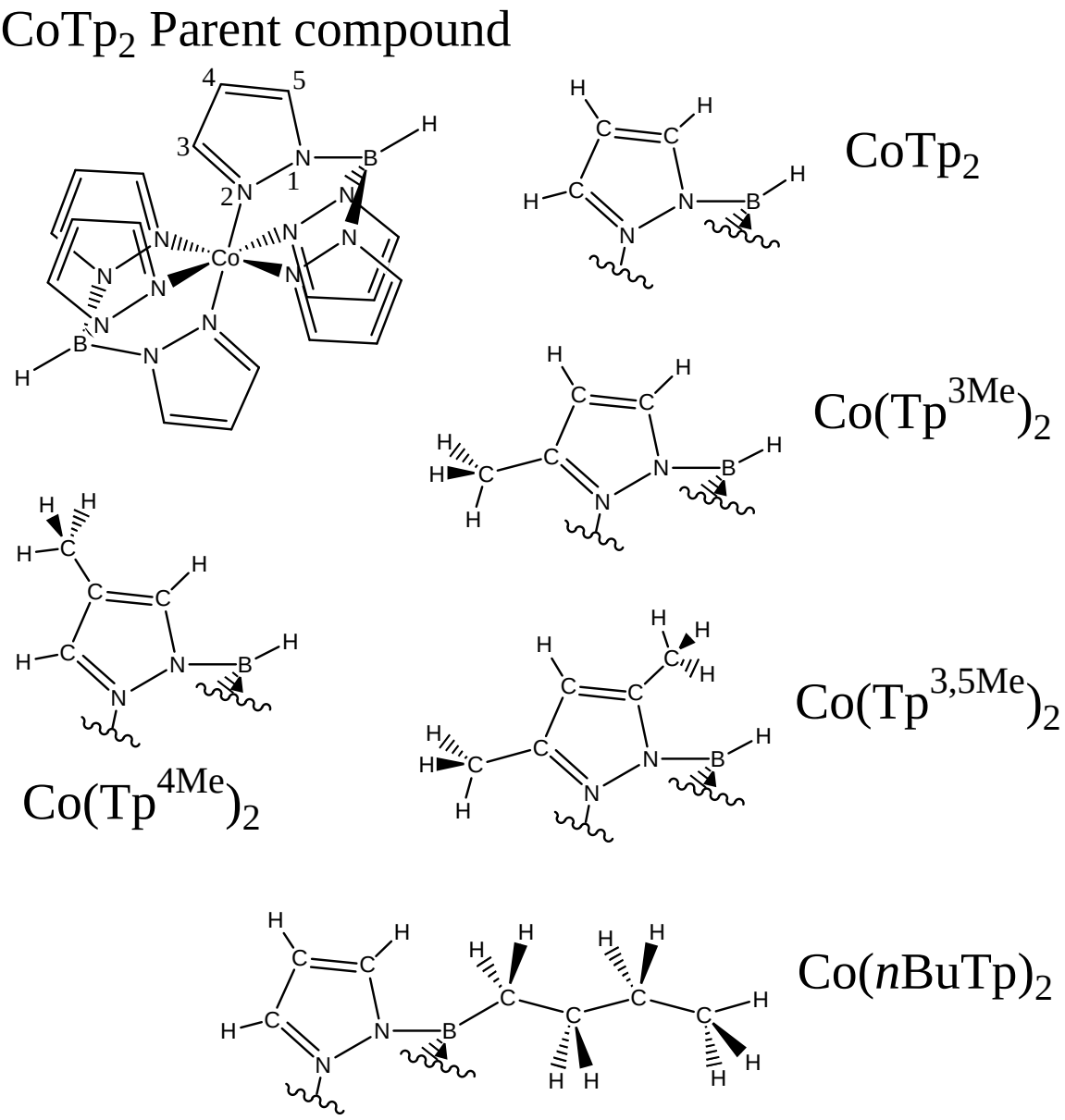

Figure 1.1 Scheme of pyrazolylborates studied in this dissertation. CoQpTp (*not shown*), is C_{3v} with one boron having a fourth, non-ligating pyrazole and the other, a standard proton.

The NMR shift equation that relates the removal of contact coupling by a methyl group substitution is given by the following:[5]

$$\delta_{\mathrm{H}}^{C} = \frac{\Delta\delta_{\mathrm{obs}} - \delta_{\mathrm{H}}^{P}\left(1 - \left(\frac{R_{\mathrm{H}}}{R_{\mathrm{Me}}}\right)^{3}\right)}{\left(\frac{R_{\mathrm{H}}}{R_{\mathrm{Me}}}\right)^{3}} \qquad \text{Eq. 1.0}$$

where $\delta_{\mathrm{H}}{}^{C}$ is the contact shift, $\Delta\delta_{\mathrm{obs}}$ is the observed shift difference between a single protons and substitute methyl protons, $\delta_{\mathrm{H}}{}^{P}$ is the paramagnetic shift, and R_{H} and R_{Me} are the distances from the metal center to proton and methyl, respectively. With the assumption that methylation has little effect on the geometric and electronic structure (demonstrated for the series of compounds in Chapter 3), individual proton positions may be probed independent of all other positions on the molecule.

Review of Trigonal Cobalt

The paramagnetic resonance properties of Co(II) have received a significant amount of attention in the past, and specifically, several papers have dealt directly with this set of compounds, performing both EPR and NMR measurements.[6-9] As a means of an introduction to the research presented in this dissertation, prior paramagnetic resonance work will first be reviewed.

Abragam and Pryce provided a comprehensive theoretical description of octahedral Co(II) electronic structure with tetragonal and trigonal distortions using crystal field theory in the 1950s.[10] The theory has as one of its two cases, the D_{3d} symmetry of the *bis*trispyrazolylborates, which is a trigonal elongation about the facial (1,1,1) axis of an octahedron. In the 1960s, Thornley, *et al.*, did an exhaustive ligand field theory

analysis of octahedral Co(II), adding consideration covalency of the ligand wavefunctions.[11] Jesson applied the theory of Abragam and Pryce to *bis*trispyrazolylborate cobalt(II),[6] and his results were refined by McGarvey in 1970.[9] Authors of subsequent monographs that consider high spin Co(II) offer quantitative analyses using Abragam and Pryces' theory; two examples are those of Ballhausen[12, 13] and Griffith.[14] More recent work utilizes the theory of Abragam and Pryce for interpretation of experimental results[15] and found agreement with *ab initio* calculations.[16]

From Abragam and Pryce,[17] the components of the overall Hamiltonian, including the effect of an external field, may be described in the order of their relative magnitude:

$$W = W_F + V + W_{LS} + W_{SS} + \beta \overline{H} \cdot (\overline{L} + g_e \overline{S}) + W_N - \gamma \beta_N \overline{H} \cdot \overline{I} \qquad \text{Eq. 1.1}$$

The total Hamiltonian consists primarily of its energies pertaining to electrons: W_F, the energy of the free-ion configuration, V, the electrostatic energy of interaction of the free ion and surrounding ions, W_{LS}, the spin-orbit interaction, and W_{SS}, the electron-electron repulsion term. Secondarily, energies pertaining to the interaction of the nuclei, indicated by W_N, combine both the hyperfine interaction between surrounding nuclei and electrons and the nuclear quadrupole interaction. And thirdly, the interactions of the external field, $\overline{H}$, may be important, $\beta \overline{H} \cdot (\overline{L} + g_e \overline{S}) - \gamma \beta_N \overline{H} \cdot \overline{I}$.

The terms of the Hamiltonian may be divided into two groups. The first four terms make up the fine structure of an ion, involving only electron-electron interactions and are of decreasing magnitudes, typically from 10^5 to 1 cm^{-1}. The latter terms are components of the hyperfine structure transitions, comprised of the electron-nuclear

interaction and the individual Zeeman interactions of electrons and nuclei, and are typically between 1 and 10^{-3} cm^{-1}. In this dissertation, the hyperfine structure will be of prime importance. However, it is the fine structure of Co(II) that gives rise to many of its unique properties.

Fine Structure

The two lowest states in the free ion configuration of Co(II) are ^4F and ^4P as may be seen in Figure 1.2 These states are split by an octahedral field into states ordered from lowest to highest as $^4T_{1g}$, $^4T_{2g}$, $^4A_{2g}$ and $^4T_{1g}$, with the last arising from the ^4P term. Subsequently, the trigonal distortion of the *bis*trispyrazolylborate compound splits the $^4T_{1g}$ ground state into ^4E_g and $^4A_{2g}$ with the orbitally-degenerate ^4E_g state lowest in energy. The $^4T_{1g}$ state common to the ^4F and ^4P terms results in mixing of ^4P states into the ground state. Spin-orbit coupling is what defines g-values in the complexes of many transition metal ions, including Co(II).[18] Abragam and Pryce treated $^4T_{1g}$ Co(II) with a fictitious orbital angular momentum ***l'*** with the analogy of t_{2g} *d*-orbitals and *p*-orbitals[12] and then used an expression for the fine structure component as $W = \delta\left(1 - l'^2_z\right) - \alpha\lambda l'_z S_z - \alpha'\lambda\left(l'_x S_x + l'_y S_y\right)$. The spin-orbit interaction is given Landé factors α and α' for the parallel and perpendicular directions, respectively. These fictitious states are:

$$|1\rangle = -\frac{1}{\sqrt{2}}\left(E_g^x + iE_g^y\right)$$

$$|0\rangle = (A_{2g})$$

$$|\text{-}1\rangle = \frac{1}{\sqrt{2}}\left(E_g^x - iE_g^y\right)$$

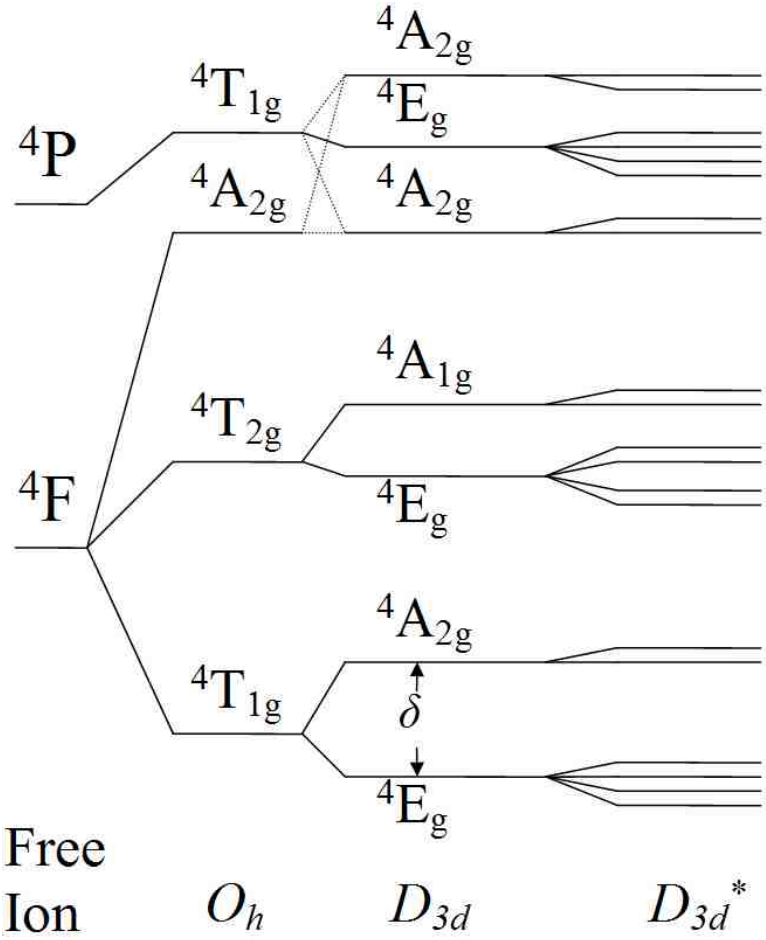

Figure 1.2 A reproduction of the energy level diagram (*not to scale*) provided by Jesson[6]. The energy levels, D_{3d}^*, correspond to the spin orbit states.

The E_g^x, E_g^y and A_{2g} states correspond to the three possible locations of the unpaired electron in the lower three *d*-orbitals:

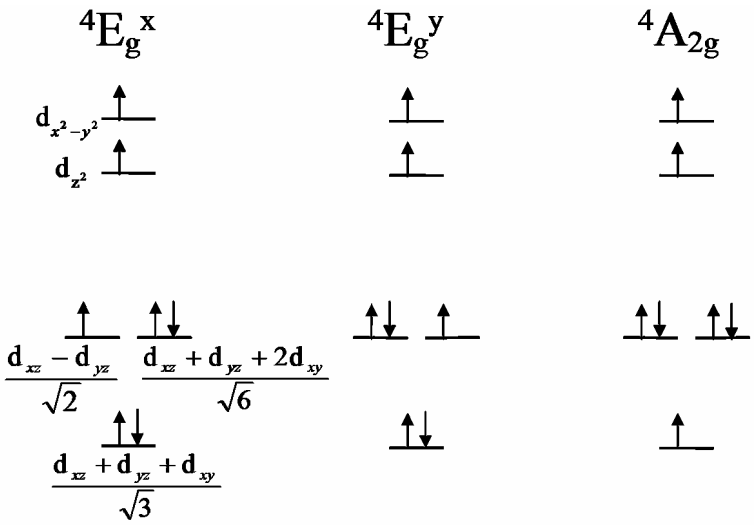

The "*dπ*" orbitals, d_{xy}, d_{yz}, and d_{xz}, are all related by the C_3 symmetry axis along the (1,1,1) direction. They are transformed through linear combinations into the above orbitals. The upper two orbitals remain along the octahedral axes, relatively unaffected by the D_{3d} symmetry. As in the scheme of Jesson, the trigonal distortion is given by the parameter δ. As defined by Ballhausen, Landé factors include consideration of the orbital reduction factor in the ligand field interaction.[13] Jesson used the values of α=1.434, α'=1.379 and δ=1900 cm^{-1} for the following spin-orbit matrix.

$$\begin{array}{c|ccc} M_J=\frac{1}{2} & \left|-1,\frac{3}{2}\right\rangle & \left|0,\frac{1}{2}\right\rangle & \left|1,-\frac{1}{2}\right\rangle \\ \hline \left|-1,\frac{3}{2}\right\rangle & \frac{3}{2}\alpha\lambda & -\sqrt{\frac{3}{2}}\alpha'\lambda & 0 \\ \left|0,\frac{1}{2}\right\rangle & -\sqrt{\frac{3}{2}}\alpha'\lambda & \delta & -\sqrt{2}\alpha'\lambda \\ \left|1,-\frac{1}{2}\right\rangle & 0 & -\sqrt{2}\alpha'\lambda & \frac{1}{2}\alpha\lambda \end{array} = 0 \qquad \text{Eq. 1.2}$$

Evaluating Eq. 1.2 yields the energies of the spin orbit states as well as the wave function coefficients, from the eigenvalues and eigenvectors, respectively. Solving the algebra of Eq. 1.2 yields the following matrix.

$$\begin{bmatrix} -315.6 & 247.8 & 0 \\ 247.8 & 1900 & 286.1 \\ 0 & 286.1 & -105.2 \end{bmatrix} = 0$$

The eigenvalues are -347.7, -139.5, and 1966.4 and the matrix of eigenvectors is

$$\begin{bmatrix} 0.9805 & -0.1651 & -0.1069 \\ -0.1272 & -0.1173 & -0.9849 \\ 0.1500 & 0.9793 & -0.1360 \end{bmatrix}$$

While stating these calculations may appear redundant in the present context, the proper selection of values for the wave function coefficients is not obvious. An erroneous selection of the 1st row of the eigenvector matrix, [0.9805, -0.1651, -0.1069], results in a negative value of $g_{\perp}$. Due to the fact that the calculation of other properties, such as the Co(II) hyperfine interaction, rely on these wave function coefficients, a systematic error will arise. The correct selection of values is the first column, [0.9805, -0.1272, 0.1500]. In order, they are *a*, *b*, and *c* of the wave function given below, which has an overall state of $\psi\left|M_J\right\rangle$ and components of $\left|M_{l'}, M_s\right\rangle$.

$$\psi\left|\pm\frac{1}{2}\right\rangle = a\left|\mp 1, \pm\frac{3}{2}\right\rangle + b\left|0, \pm\frac{1}{2}\right\rangle + c\left|\pm 1, \mp\frac{1}{2}\right\rangle \qquad \text{Eq. 1.3}$$

These coefficients are proportional to the relative contributions of the microstates. Their magnitude will be considered again in Chapter 4. It is a state with M_s=|±3/2〉 that has the greatest contribution to the ground state wavefunction.

Even though there appears to be a large contribution of $M_S=|\pm 3/2\rangle$, the orbitally degenerate, Kramers ground state of Co(II) is described as an *effective S*'=1/2. As will be seen in the following section, the appreciable splitting of the lowest doublet from the next due to spin orbit coupling makes for a ground state description of *S*'=1/2, not *S*=3/2.[18] Some have defined the Hamiltonian in terms of *J* instead of *S* due to the large spin orbit splitting that is characteristic of $^4T_{1g}$ ground states.[19]

The eigenvalues of the matrix correspond to energies of the spin states. Utilizing the 2x2 and 1x1 spin-orbit matrices, Eq. 1.4 and 1.5, respectively, in addition to Eq. 1.2, a plot of the spin orbit states maybe generated with respect to the magnitude of the trigonal distortion parameter, δ, as seen in Figure 1.2. The MATLAB scripts for these calculations are provided in Appendix I.

$$\begin{array}{c|cc} M_J=\frac{3}{2} & \left|0,\frac{3}{2}\right\rangle & \left|1,\frac{1}{2}\right\rangle \\ \hline \left|0,\frac{3}{2}\right\rangle & \delta & -\sqrt{\frac{3}{2}}\alpha'\lambda \\ \left|1,\frac{1}{2}\right\rangle & -\sqrt{\frac{3}{2}}\alpha'\lambda & -\frac{1}{2}\alpha\lambda \end{array} = 0 \qquad \text{Eq. 1.4}$$

$$\begin{array}{c|c} M_J=\frac{5}{2} & \left|1,\frac{3}{2}\right\rangle \\ \hline \left|1,\frac{3}{2}\right\rangle & -\frac{3}{2}\alpha\lambda \end{array} = 0 \qquad \text{Eq. 1.5}$$

The ground state g-values were calculated with the following expression of Jesson[6] based on the wavefunction coefficients of Eq. 1.3.

$$\begin{aligned} g_{\|} &= g_{S\|} + g_{L\|} = \left(6a^2 + 2b^2 - 2c^2\right) + 2\alpha\left(a^2 - c^2\right) \\ g_{\perp} &= g_{S\perp} + g_{L\perp} = \left(4b^2 + 4\sqrt{3}ac\right) - \alpha' bc\sqrt{8} \end{aligned} \qquad \text{Eq. 1.6}$$

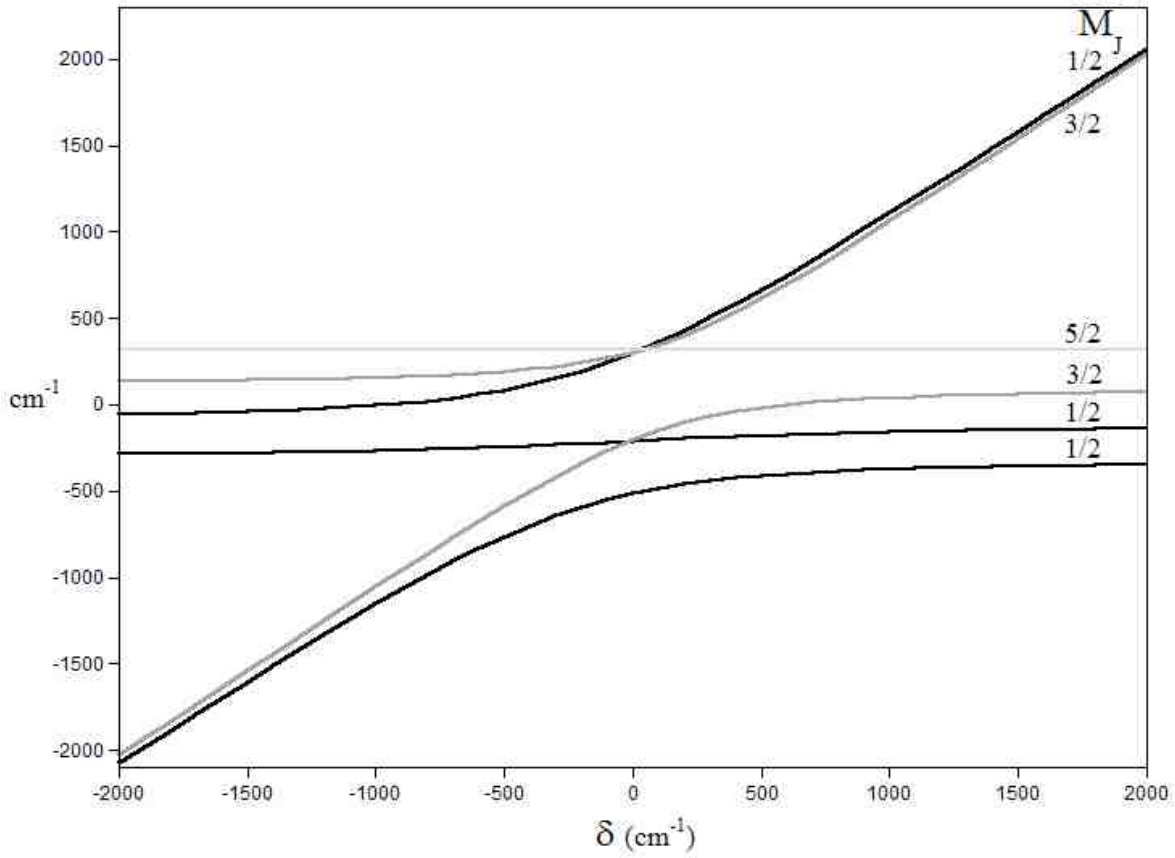

Figure 1.3 The energies of spin-orbit states as a function of the trigonal distortion parameter, δ. There are six Kramer's doublets in total.

A fitting process was used by Jesson to optimize values of the Landé factors and the trigonal distortion parameter, providing $g_{\|}$=8.45 and $g_{\perp}$=1.16. They correspond with the g-values determined by Jesson, 8.46 and 0.98, and are close to those found in a more recent study, 8.48 and 1.02.[5]

Fink, *et al.*, found agreement with the predictions of Abragam and Pryce using a combination of *ab initio* methods, including restricted, open-shell Hartree-Fock (ROHF), complete active space self-consistent field (CASSCF) and valence configuration interaction (VCI) with inclusion of spin-orbit coupling.[16] Due to the computation time cost of these methods, they created a model complex of three fictitious ligands, L, and three Cl ligands for an overall trigonal elongation of the octahedron with a C_{3v} point group. Their calculations generated similar energies of states (0, 283, 478, 942, 1137, and 1268 cm^{-1}, compared with 0, 206, 417, 659, 2278, and 2310 cm^{-1} for $Co(Tp)_2$), the same M_J ordering of states from the spin orbit coupling (SOC) interaction (1/2, 1/2, 3/2, 5/2, 3/2, and 1/2, low to high), and ground state *g*-values that differ significantly from g_e, $g_{\|}$=6.60 and $g_{\perp}$=3.24. The bond angles were similar as well, with ∠ClCoCl = 85.66 for their compound and $\angle NCoN_{avg}$ = 85.74 for $Co(Tp)_2$.

The variation of the trigonal distortion parameter yields a series of *g*-values that may be seen in Figure 1.4. Under trigonal compression, or a negative sign of δ, the g-values approach $g_{\|}$=2 and $g_{\perp}$=4. The trisbipyridine complex of Co(II) displays a trigonal compression with g-values of $g_{\|}$=2.06 and $g_{\perp}$=4.116. With the trigonal elongation of the bistrispyrazolyl compounds, the *g*-values tend toward 8.87 and 0. Using the same values provided, with the variation in the trigonal distortion parameter, a 'parametric'

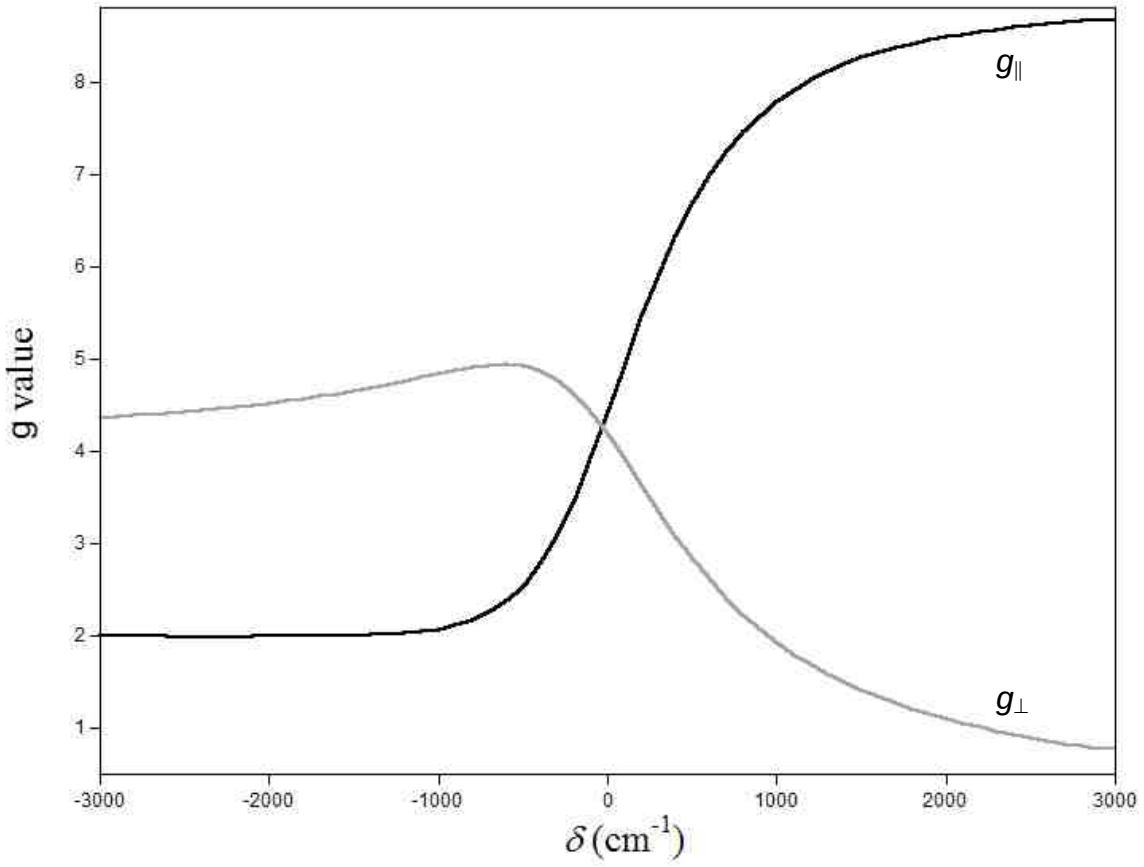

Figure 1.4 The $g_{\|}$, black, and $g_{\perp}$, grey, of a D_{3d} Co(II) complex utilizing the trigonal distortion parameter, δ. Increasing trigonal elongation is represented as $\delta>0$ and compression is in direction of $\delta<0$. Figure was calculated with equations 1.2 to 1.6.

representation may be prepared by plotting $g_{\|}$ on the abscissa and $g_{\perp}$ on the ordinate, as in Figure 1.5. Abragam and Pryce used this presentation to assess calculations of g-values and, for the trigonal case, compared the values with those of cobalt fluorosilicate. They found good agreement.[10] Griffith used the same parametric presentation to assess the ligand field strength for a number of unstated experimental compounds, with the weak-field abscissa intercept at (9,0) and the strong-field at (8,0).[14] Ligands with coordinated, sp^2-hybridized nitrogen, such as phenanthroline and pyrazole are characteristic strong-field ligands,[20] however a weak field interaction is expected to produce a high spin compound. The abscissa intercept of Jesson's *g*-value equations is consistent with the Griffith's application of the Abragam and Pryce theory.

Hyperfine structure

The theory established by Abragam and Pryce is manifest not simply in the calculation of *g*-values, but also in the explanation of the Co(II) hyperfine structure. The nucleus ^{59}Co is 100% abundant, with I=7/2 nucleus, and according to the 2I+1 rule, will have eight hyperfine lines as observed in EPR. The axial symmetry of a trigonal distortion is mirrored in an axial metal hyperfine interaction, with the parallel direction given by $A=A_L+A_{Sd}+A_{Ss}$ and the perpendicular, $B=B_L+B_{Sd}+B_{Ss}$. Their components are the orbital moment of the electrons, A_L, B_L; the spin moment of the 3d electrons, A_{Sd}, B_{Sd}; and admixture of configurations containing unpaired *s*-electrons, A_{Ss}, B_{Ss}.[10] Abragam and Pryce found the contribution of the 3d electron spin moment to be only a few percent of the magnitude of the other two. For both A and B, the admixture term had

A.

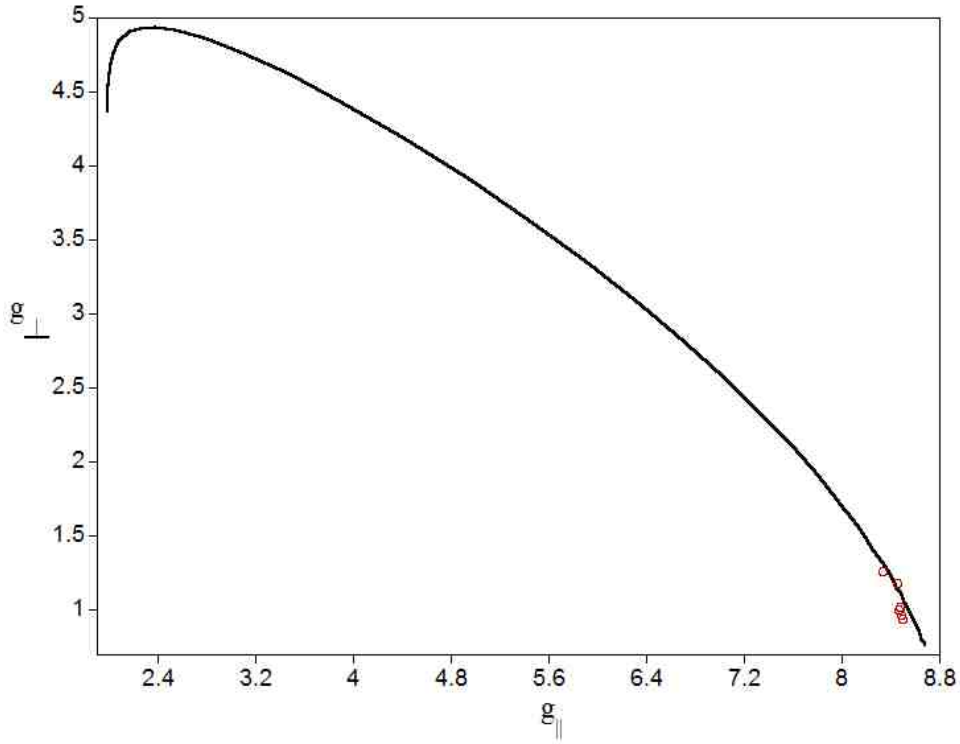

B.

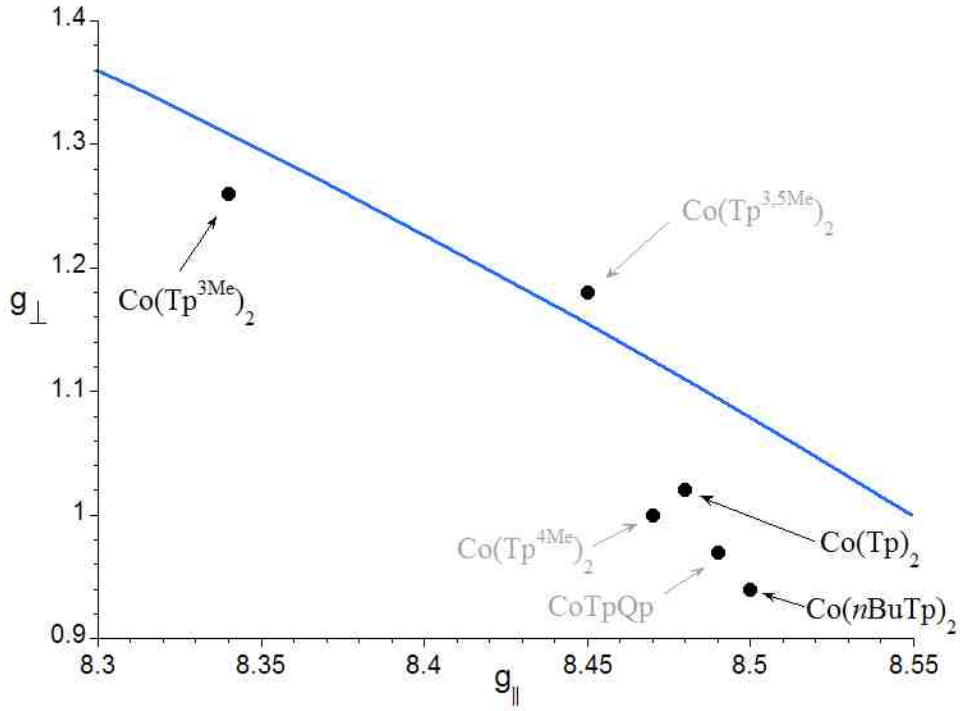

Figure 1.5 A. 'parametric' representation of the relation of the g values predicted by Jesson's treatment of Abragam and Pryce's theory. A. *g*-values for all values of $|\delta| \leq 3000$.

the largest contribution, and it is a function of the covalency of the *d*-orbitals by a parameter κ: $A_{Ss}=-\kappa\gamma\beta\beta_n r^{-3} g_{S\|}$, $B_{Ss}=-\kappa\gamma\beta\beta_n r^{-3} g_{S\perp}$, a function of delocalization of the *d*-electrons in the molecular orbitals containing the ligating atoms. Jesson used the covalency parameter to fit the $Co(Tp)_2$ ^{59}Co hyperfine by reducing κ by 25% from that of Abragam and Pryce, using a value of 0.325.

As with anisotropy in the Co(II) hyperfine, McGarvey and Jesson treat the Fermi contact of the ligand hyperfine interactions as anisotropic.[7, 9] The Fermi interaction arises from the spin component of the *g*-factors, g_S in Eq. 1.6, with $A=1/2g_{S\|}= 3a^2+b^2-c$ and $B=1/2g_{S\perp}=2b^2+2ac\sqrt{3}$. Again, *a*, *b*, and *c* are the wavefunction coefficients of Eq. 1.3. The anisotropic Fermi interaction is also called a pseudo-dipolar interaction and is likely due to a large contribution from the unquenched orbital angular momentum.

Taken as a whole, the theory of Abragam and Pryce was successfully applied by Jesson and McGarvey to optical, EPR and NMR experimental data of $Co(Tp)_2$ and its derivatives. The features of the theory here reviewed will be applied to the EPR and ENDOR data of this dissertation.

Chapter 2

EPR Simulations

EPR simulations allow one to ascertain a precise set of parameter values to describe EPR spectra. Extensive simulations were performed for $Co(Tp)_2$ EPR spectra without an *a priori* analytical determination of the ground state g-values. Four suppositions were used: **S1**, the ground state is perfectly axial $M_s=|\pm 3/2\rangle$, the axial zero-field splitting, D is << 0 cm^{-1}, the rhombic zero-field splitting, E, is 0; **S2**, the ground state is $M_s=|\pm 3/2\rangle$, D =-10.5 cm^{-1}, $E\neq 0$; **S3**, the ground state is $M_s=|\pm 1/2\rangle$, $D<<0$, $E\neq 0$; and **S4**, using an effective $S'=1/2$, the ground state is M_s(*or* M_J)$=|\pm 1/2\rangle$, $D>>0$, $E\neq 0$ and g-values are dominated by spin orbit coupling. In each case, a g-strain model was used to match the line widths. The value of -10.5 cm^{-1} for D used in **S2** comes from application of Makinen's method for determining the zero field splitting ($2D$) from the microwave power at half-saturation to the $CoTp_2$ EPR signal.[21] Given the uniform success of these varying approaches, **S2** was selected for simulation of a series of five-coordinated Co(II) model complexes, as it most closely resembled recent literature. While this treatment may not be strictly correct, use of a consistent approach allows assessment of trends within a given set of molecules.

The Tierney lab has utilized XSophe for simulations of CW EPR spectra of *hs* Co(II) compounds. XSophe is distributed by Bruker-Biospin and it was developed by Graham Hanson at the University of Australia.[22] The purpose of these simulations was to test the sensitivity of the simulations to the various parameters and to demonstrate that there is no unique solution in EPR simulations of this type. Recent approaches to simulations of Co(II) have employed the relation of g_{eff}, the observed g-value, and g_{real},

the "true" *g*-values,[23] as devised by W.R. Hagen's Rhombogram scheme.[24] The g_{real} is related to the effective by the following:[23, 25]

$$g_{eff\,(x)} = g_{real\,(x)}\left[1 \pm \left[1 + 3(E/D)\right] / \sqrt{1 + 3(E/D)^2}\right]$$

$$g_{eff\,(y)} = g_{real\,(y)}\left[1 \pm \left[1 - 3(E/D)\right] / \sqrt{1 + 3(E/D)^2}\right] \qquad \text{Eq. 2.0}$$

$$g_{eff.(z)} = g_{real\,(z)}\left[1 \pm -2 / \sqrt{1 + 3(E/D)^2}\right]$$

Due to the fact that recent simulations have used this approach for Co(II) in biological systems, it was therefore used as a starting point.

Simulation Parameters

XSophe simulations described below follow a basic spin Hamiltonian[22]:

$$H = \hat{S} \cdot \mathbf{D} \cdot \hat{S} + \beta \vec{B} \cdot \mathbf{g} \cdot \hat{S} + \hat{S} \cdot \mathbf{A} \cdot \hat{I} \qquad \text{Eq. 2.1}$$

Here, $\hat{S}$ is the electron spin operator, **D** is the zero field splitting tensor, β is the Bohr magneton, $\vec{B}$ is the applied magnetic field, **g** is the electron Zeeman coupling matrix, **A** is the hyperfine coupling matrix and $\hat{I}$ is the nuclear spin operator. The terms are ordered in magnitude of energy. Typical values for the zero-field splitting, $|\Delta|$, of *hs* Co(II) in low symmetry Zn(II) sites are reported to be 2.3 to 98 cm^{-1}.[26] The quadrupole and nuclear Zeeman interactions are not explicitly considered due to the large Co(II) EPR line widths.

Simulations with XSophe are amenable to a systematic approach based on exact simulations of careful measurements of experimental spectra. A high degree of simulation accuracy is achieved by matching the standard set of spectra data: relative peak heights, full-width at half maximum (FWHM), and peak locations in Gauss. Experimental parameters, such as temperature, microwave frequency, microwave field,

a)

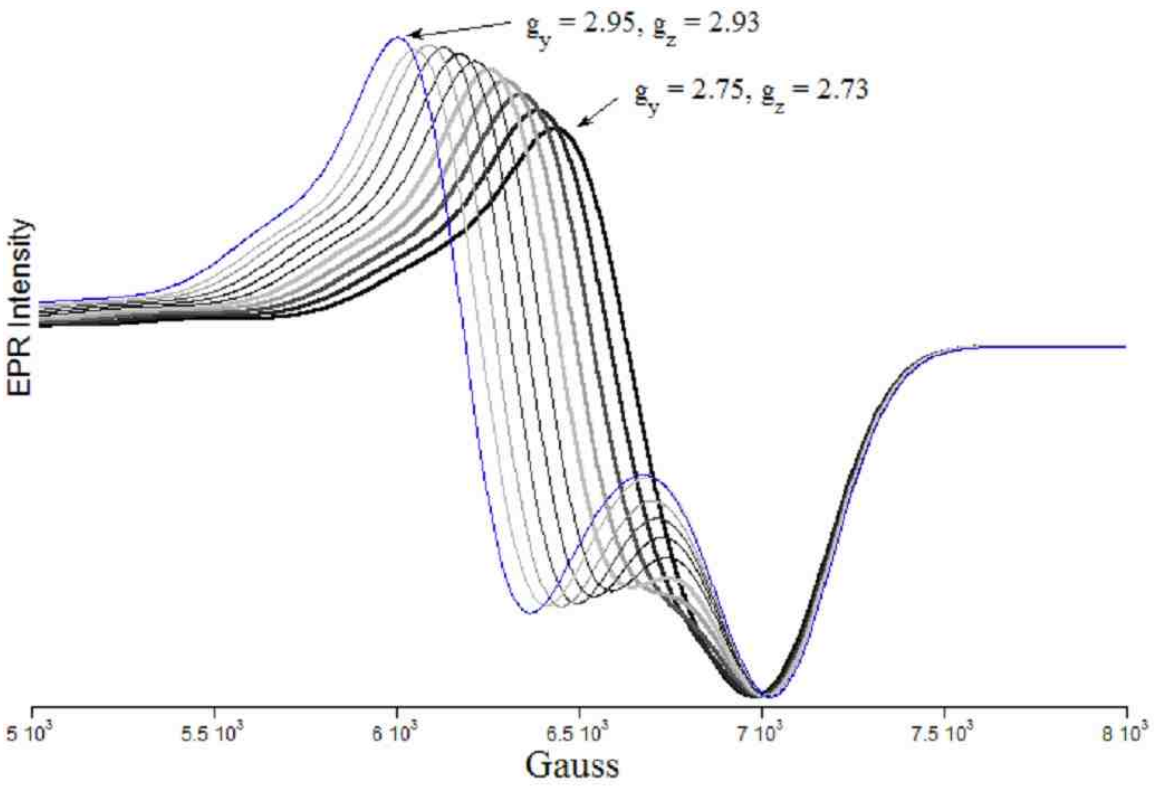

b)

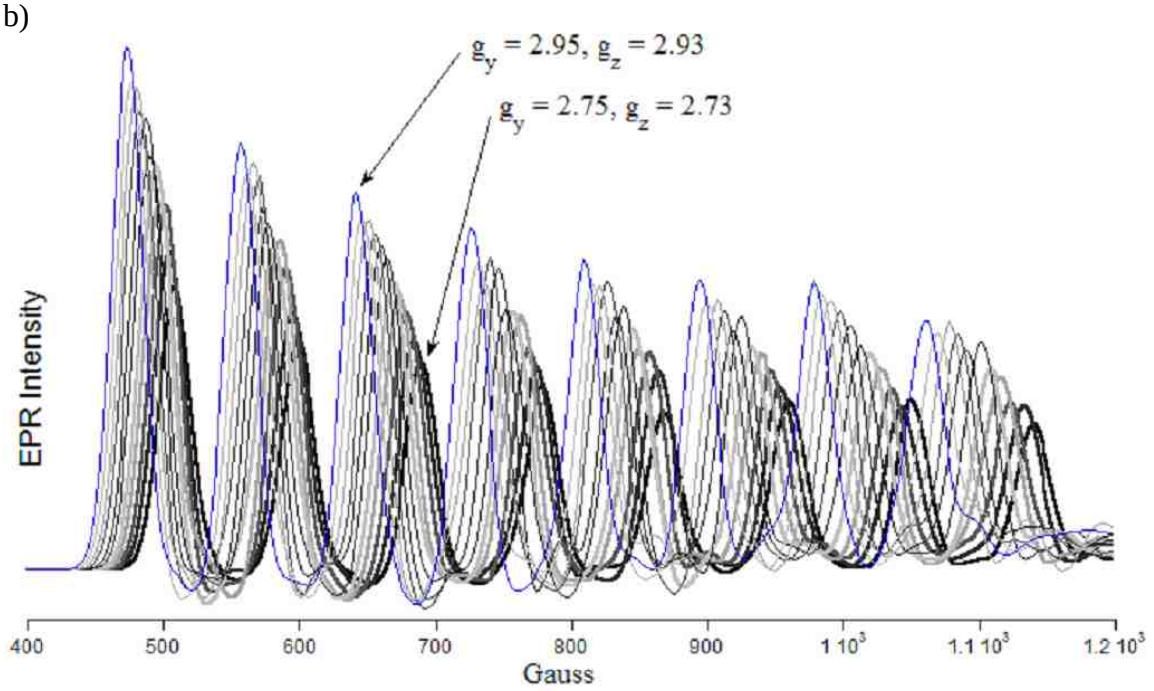

Figure 2.1 Effect of 0.02 iteratively added to g_y and g_z on a) $g_\perp$ and b) $g_\parallel$. g_x is constant

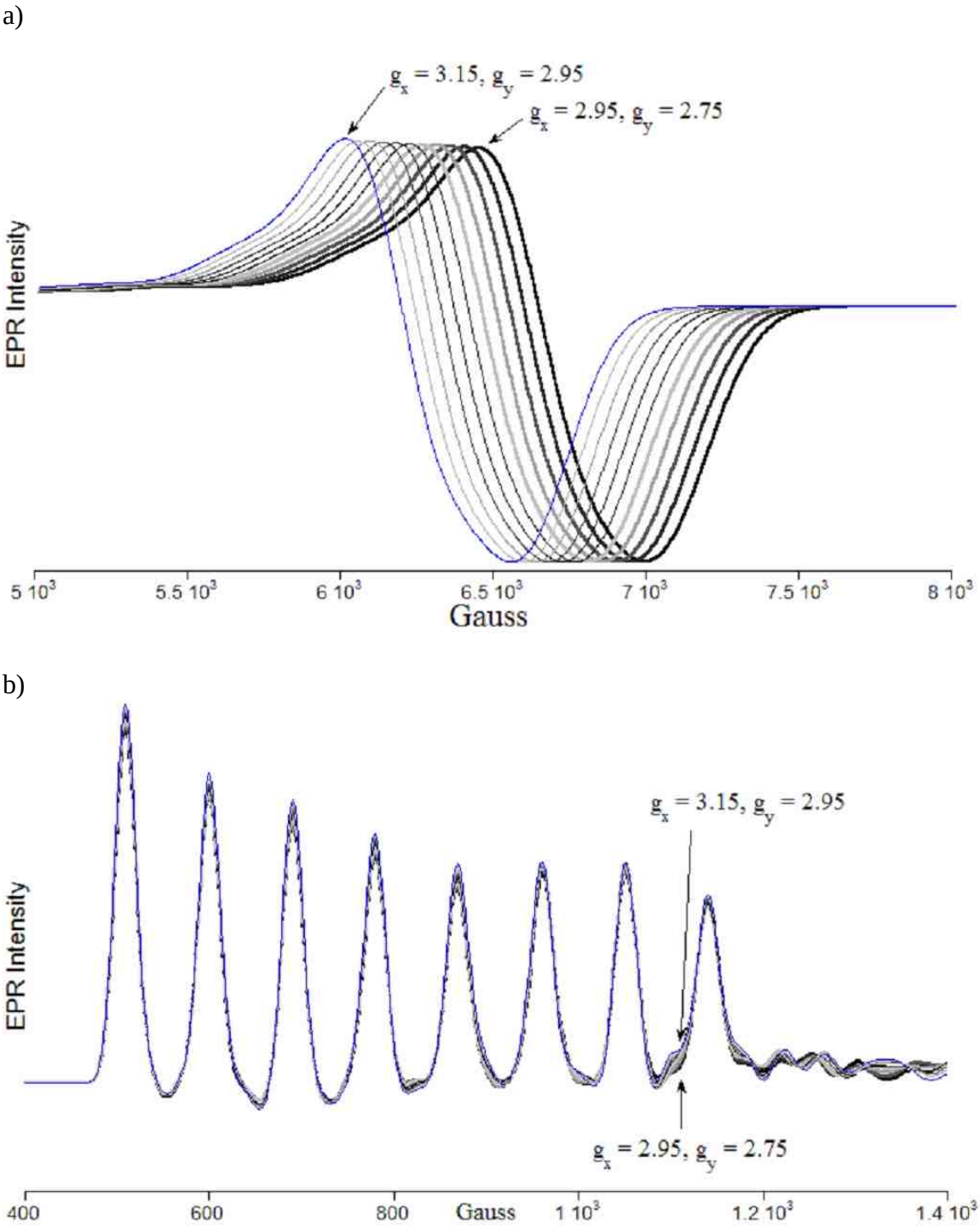

Figure 2.2 Effect of 0.02 iteratively added to g_x and g_y on a) $g_\perp$ and b) $g_\parallel$. The small oscillations at the high field end of b) are calculation artifacts. g_z is constant.

and sweep width were successfully implemented in XSophe for facile simulations. Automated parameter optimization routines of XSophe were apparently not implemented, and all iterative parameter optimization was done manually.

Determination of meaningful EPR simulation parameter values is predicated by the acquisition of experimental EPR spectra that are representative of non-saturating conditions. In the simplest case, assume that only the ground state Kramer's doublet is excited, *i.e.* no thermal population of higher doublets. Under non-saturating conditions the EPR signal intensity is proportional the inverse square of the microwave power. Likewise for non-saturating conditions, signal intensity will also follow the inverse of temperature. For a given microwave power, the signal intensity will typically increase to a maximum at a particular temperature and then decrease with a 1/T dependence. This "maximum signal temperature" has been used to differentiate types of iron-sulfur clusters.[27] For a given temperature there will be a power setting where maximum signal intensity occurs. At microwave powers lower than this maximum, the signal intensity follows $P^{-1/2}$ dependence. Therefore, every sample will have a two-dimensional relation of power and temperature for the maximum signal intensity. Spectra designated for EPR simulations are best acquired in the (power, temperature) parameter space beyond this maximum signal, *i.e.* lower power and/or higher temperature. In an upcoming book chapter, Bennett prescribes the return of the high field end of the integral of a first-derivative EPR spectrum to the initial point at low field as an indication of good spectrometer conditions.[28]

Initial parameter value searching within **S2** started from values provided by a developer of XSophe, who chose values consistent with a Rhombogram devised for high

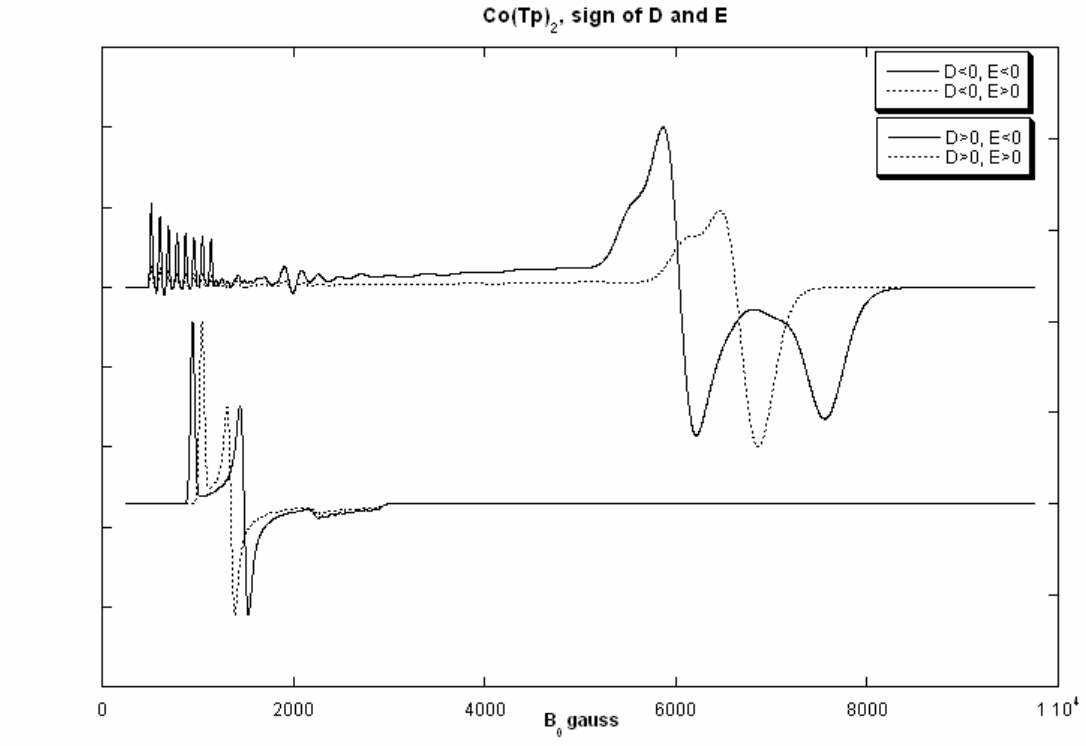

Figure 2.3 The $g_{||}$ region at X-band, with iterative additions of 0.2 to g_x and g_y. Again, the ripples between the Co(II) hyperfine lines and $g_{\perp}$ and the "notch" in the upper part of the derivative of $g_{\perp}$ are artifacts of the calculation. Inclusion of a greater number of orientations in the calculation will remove these artifacts, afford a smoother spectrum and greatly increase the calculation time. However, the apparent g-values will remain constant.

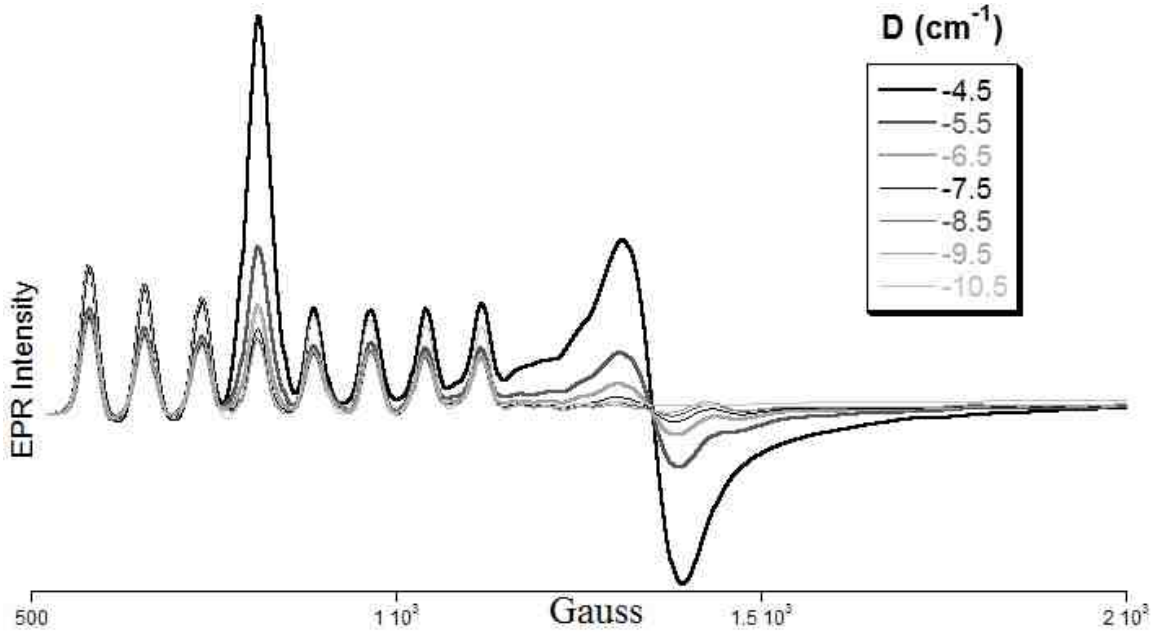

Figure 2.4. The affect of magnitude and sign of D for $D<0$ hyperfine lines.

spin Co(II).[23, 29] The first task was to determine what parameter values control which features of the simulated spectrum. The experimental spectrum is axial, consisting of an eight line pattern at the unique *g*-value of 8.48 and a derivative feature at *g*=1.02. XSophe uses g_x, g_y and g_z and these must be matched to the experimental *g*-values of g_1, g_2 and g_3. In an attempt to assign g_z, the values of g_y and g_z were varied by increments of 0.02 at $g_\perp$ as send in Figure 2.1a. As both of these values increase, only the derivative-shaped spectral feature shifts as a unit to lower field, higher in g-value. There is a component of $g_\perp$ that is not dependent on g_y and g_z, which evidently arises from g_x. The same approach was used to examine the $g_\parallel$ region. The entire feature shifts to lower field (higher *g*-value) with increasing g_y and g_z. Only one g-value may be assigned to $g_\parallel$, thus it appears to be g_z. Additions of 0.02 to g_x and g_y yields a shift of the entire $g_\perp$ feature and the feature depends on both g_x and g_y equally, as may be seen in Figure 2.2a. From Figure 2.2b, it may be seen that incremental change of g_x and g_y has no effect on $g_\parallel$. In conclusion, the assignment of g_1, g_2, and g_3 (numbered in the direction of low to high field) appears as g_z, g_y, and g_x, respectively.

In most cases, the zero field splitting tensor, **D**, is traceless (meaning $D_x+D_y+D_z=0$), and its components may be divided into the three cases for EPR: isotropic ($D_x=D_y=D_z$), axial ($D_x=D_y\neq D_z$), and rhombic ($D_x\neq D_y\neq D_z$). The axial zero field splitting, *D*, and the rhombic zero field splitting, *E*, are given by the following.[30]

$$D = D_z - \frac{D_x + D_y}{2} \quad \text{(A)} \qquad E = \frac{D_x - D_y}{2} \quad \text{(B)} \qquad \text{Eq. 2.2}$$

The effect of the sign of *D* and *E* on the calculated spectrum is seen in Figure 2.3. In the top set of the two traces, *D* is held negative, such that the ground state is $M_s=|\pm 3/2\rangle$. There is a marked change in the character of the EPR spectrum upon switching the sign

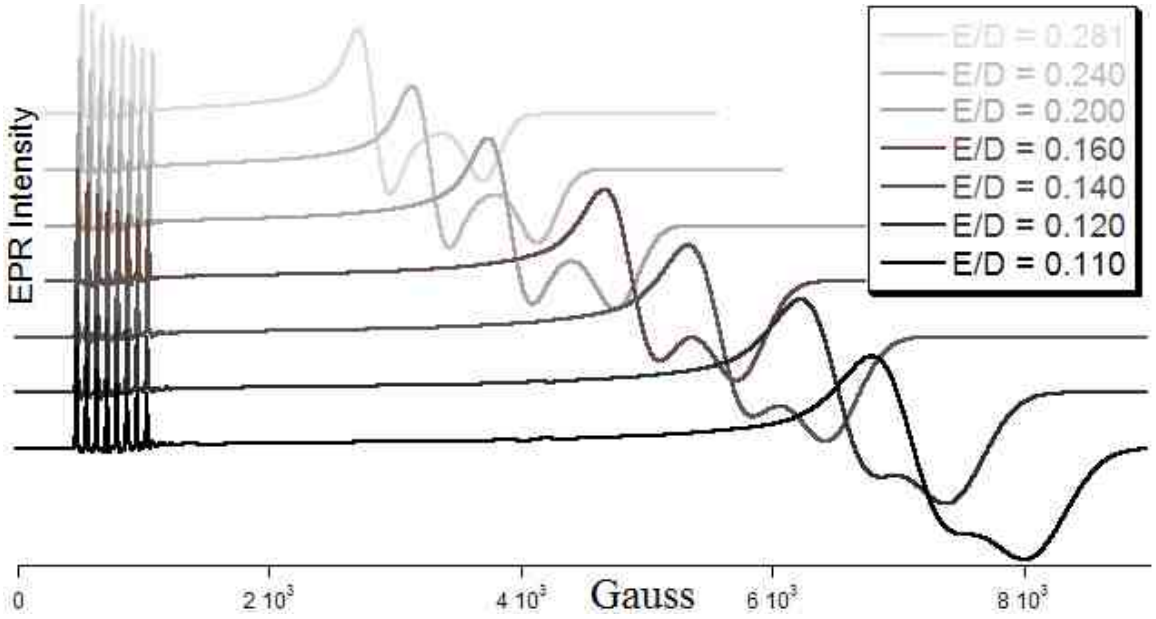

Figure 2.5. The effect of E/D on $g_{\perp}$.

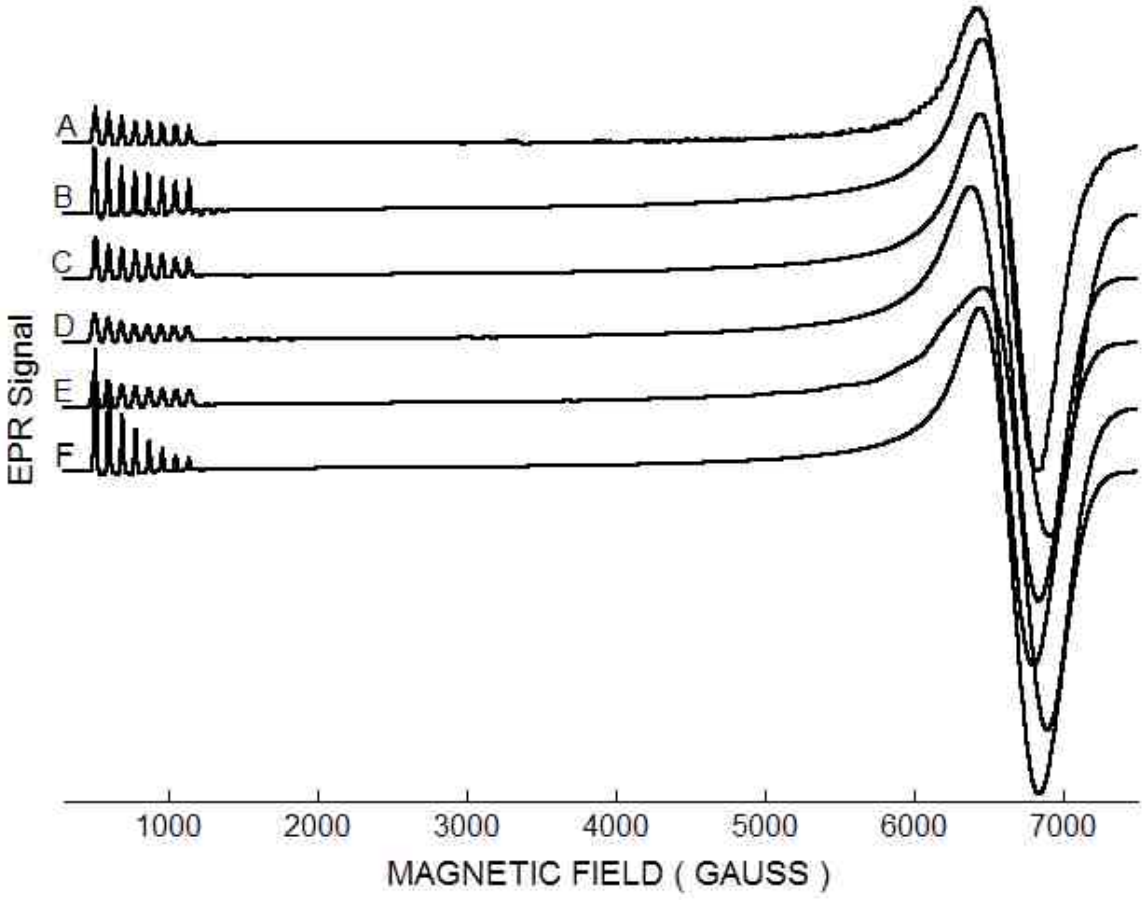

Figure 2.6 (A) $Co(Tp)_2$ (black) observed values $g_{\|}$=8.48, $g_{\perp}$=1.02, and $A_{\|}$=92.7 gauss; (B) **S3** values g(x,y,z)=(3.02, 2.74, 2.72), A_z=113x10^{-4} cm^{-1}, D=-50 cm^{-1}, E/D=0.113, line width(x,y)=(20,20); (C) **S2** g(x,y,z)=(3.02, 2.74, 2.72), A_z=113x10^{-4} cm^{-1}, D=-10.5 cm^{-1}, E/D=0.113, line width(x,y)=(20,20); (D) **S1** D=-10.5 cm^{-1}, E/D=0, A_z=335x10^{-4} cm^{-1}, $g_{\|}$=8.48, $g_{\perp}$=0.5 (E) **S4** D=10.5 cm^{-1}, E/D=0, positive value of D (F) M_s=$|\pm 5/2\rangle$ g(x,y,z)=(2.93,3.9,1.65), A_z=69x10^{-4} cm^{-1}, D=-10.5 cm^{-1}, E/D=0.3. The apparent differences in $g_{\perp}$ could be rectified with a more exhaustive search of parameter values.

of D to positive. Most obvious is the range of g-values switching from approximately g=7 to g=2. In addition, the assignment of g-values changes to $g_1 = g_y$, $g_2 = g_x$, and $g_3 = g_z$. Changing the sign of E exchanges the assignments of g_x and g_y.

The magnitude of D controls the separation of the $M_s = |\pm 3/2\rangle$ and $M_s = |\pm 1/2\rangle$ levels. A low magnitude of D will result in population of the upper state even at the lowest temperatures. When the temperature is set to 4K in the calculation and the microwave frequency to 9.5 GHz, the spectral component of the second, upper state is seen, as in Figure 2.4. Here, D is approaching zero and is negative. Below $|D| = 10.5$ cm^{-1}, the features of the upper state, $M_s = |\pm 1/2\rangle$ in this case, become apparent within and about the $g_{\|}$ region of the spectrum. Not shown is the ^{59}Co hyperfine of the level that appears at the high-field g-value of an $M_s = |\pm 1/2\rangle$ level, near g=2. Thus, a selection of any value of $|D| \geq 10.5$ cm^{-1} will essentially only populate the ground state spin level at helium temperatures within the limits of the calculation. For the effective S'=1/2 normally employed in the simulation of Co(II) EPR spectra, an "arbitrarily large" D of 50 cm^{-1} is often used.[28]

In these simulations, the magnitude of E is expressed as the ratio E/D, and the amount of rhombicity is proportional to the separation of g_x and g_y in the simulated spectrum. The magnitude of E/D also has a significant impact on the effective value of $g_{\perp}$. As seen in Figure 2.5, an increasing magnitude of E/D from 0.110 to 0.281 moves the effective average of g_x and g_y from near 7750 gauss to 3400 gauss, g~2. The value of $g_{\perp}$ may of course be adjusted by directly changing the input g-values themselves.

When the value of E/D is set to zero and the magnitude of D is set to a relatively large number, e.g. 50 cm^{-1} is a typical literature value,[31-33] the real g-values will more

Table 2.1 Experimental X-band EPR parameters.[(a)]

Compound	$g_{\|}$ ($A_{\|}$, $\Delta\nu_{½}$)	$g_{\perp}$ ($\Delta\nu_{½}$)	$R_{N\cdot\cdot N}$[(c)]
Co(*n*BuTp)$_2$	8.50 (94, 22)	0.94 (1300)	2.87
Co(TpQp)	8.49 (93, 22)	0.97 (1300)	2.87
Co(Tp^{4Me})$_2$	8.47 (93, 20)	1.00 (1600)	2.88
Co(Tp)$_2$	8.48 (93, 21)	1.02 (1400)	2.89
Co(Tp^{3,5Me})$_2$	8.45 (92, 21)	1.18 (1100)	2.93
Co(Tp^{3Me})$_2$	8.34 (89, 20)	1.26 (1600)	2.96

[(a)] All spectra were collected at T = 3.6 K with 5 G field modulation (100 kHz), time constant = 82 ms, 0.2 mW (X-band, 9.38 GHz) receiver gain = $5x10^3$. Data was acquired by Tierney and reported in Myers et al.[5]

[(b)] Values of $A_{\|}$ reported in gauss; FWHM ($g_{\|}$) or baseline-to-baseline line width ($g_{\perp}$) in gauss.

[(c)] Average distance between the coordinated nitrogens on a single trispyrazolyl borate, in Å.

closely resemble those from the experimental spectrum. With a negative value of D, $g_{\perp}$ real will be one half the observed, experimental $g_{\perp}$. When D is positive, $g_{\perp}$ real is the same as the observed value. For both positive and negative D, $g_{\|}$ real is the same as the experimental value. The success important point is that of the simulation is independent of the input sign of D. Figure 2.6 shows this insensitivity. In fact, this figure shows all of the varying approaches to be essentially equivalent: sign of D, $E/D>0$ vs. $E/D=0$, and even $M_s=|\pm 5/2\rangle$. This was further confirmed with a series of methyl-substituted derivatives of $Co(Tp)_2$, in Table 2.1. Differences arise, however, in the relative intensities of the low field and high field ends of the eight line hyperfine pattern of the ^{59}Co nucleus. A $M_s=|\pm 5/2\rangle$ ground state predicts a much larger difference within the hyperfine intensities than a $M_s=|\pm 1/2\rangle$ state.

Simulations of $Co(Tp)_2$

With the little apparent difference in the simulation approaches, the **S2** case was expanded further and applied to a series of *bis*trispyrazolylborate compounds of Co(II), whose EPR *g*-values are the ones depicted in Figure 1.4b and tabulated in Table 2.1. There are three trends apparent in these compounds: a large apparent shift in the value of $g_{\perp}$, a small decrease in the value of $g_{\|}$, and a continuous change in the magnitude of the ^{59}Co hyperfine, $A_{\|}$. Based on the change of values from $Co(n\text{BuTp})_2$ to $Co(Tp^{3Me})_2$, $g_{\perp}$ increases by 0.32, or 34%, and $g_{\|}$ decreases by 0.16, or 2%. An exception to this is the small increase of 0.01 in $g_{\|}$ observed for $Co(Tp^{4Me})_2$. Thus the total change per *g*-value is 0.16. The increase in $g_{\perp}$ and decrease $g_{\|}$ do not cancel each other. The average *g*-value

Table 2.2 XSophe Simulation Parameter Values $Co(Tp)_2$ series[†]

	g_x	g_y	g_z	A_z[(a)]	D[(b)]	E/D[(c)]	Line width (x,y)[(d)]
$Co(n\text{BuTp})_2$	3.02	2.74	2.77	118.5	-11.5	-0.1095	20,20
$Co(TpQp)_2$	3.02	2.74	2.77	117.5	-11	-0.1127	20,20
$Co(Tp^{4Me})_2$	3.02	2.74	2.75	115	-10.5	-0.115	100,30
$Co(Tp)_2$	3.02	2.74	2.72	113	-10.5	-0.118	20,20
$Co(Tp^{3,5Me})_2$	3.02	2.74	2.74	98	-10.5	-0.137	20,80
$Co(Tp^{3Me})_2$	3.02	2.74	2.66	97	-10.5	-0.1445	20,50

[†]Adapted from the supplemental information of Myers et al.[5]

(a) All spectra were simulated with T = 4K, partitions = 160, segments g = 16, g-strain(x,y,z) = 0.025, 0.025, 0, transition threshold = 0.01, and all other parameters set to default. Peak assignments with increasing Zeeman field: $g_1=g_z$, $g_2=g_y$, and $g_3=g_x$. Reversing the sign of E/D, permutes the assignment of g_2 and g_3.

(b) Values are in $1x10^{-4}$ cm^{-1}, with A_x and A_y arbitrarily given a value of 1.

(c) Values are in cm^{-1}.

(d) Line widths reflect the input parameter value, not the resulting width, which may be simulated interchangeably with line width or g-strain. The line width z equals 40 for all compounds.

changes from 3.42 to 3.62, where $g_{avg}=g_{\|}+2*\ g_{\perp}$. Consistent with the trend of $g_{\|}$, the $A_{\|}$ decreases by 5 Gauss across the series. The ^{59}Co hyperfine interaction is derived from the spin density of electrons about the Co(II) ion, and a decrease in spin density will result in a decrease in the magnitude of $A_{\|}$. In an attempt to correlate this observed trend in $A_{\|}$ to a geometrically change in the compounds, a column of structural information was added to the X-EPR data Table 2.1 to show the change in the tightness of binding to the cobalt. The decrease in N··N distance of nitrogen atoms coordinated to Co(II) from a single trispyrazolylborate ligand follows the trend of decreasing $A_{\|}$. The bond angle from the B··Co axis is fairly constant across the series of compounds, thus the bite angle of the ligand is constant. The Co··N bond length also increase from Co(*n*BuTp)$_2$ to Co(Tp^{3Me})$_2$.At the extremes, for Co(*n*BuTp)$_2$ this distance is 2.116Å and it lengthens to 2.162Å for Co(Tp^{3Me})$_2$. Thus a shorter bond length will lead a stronger Co(II) hyperfine. This is somewhat counterintuitive as it would be expected that the mechanism of the hyperfine interaction, core polarization of *s* electrons by unpaired electrons in the *d* orbitals, would dictate stronger hyperfine interactions by more *d* localization on the metal, not less, as expected from tighter bonds to the ligating nitrogens. One possibility suggested by van Kooten et al., is that in a d^7 orbitally-degenerate $^4T_1$ ground state, Fe^+ in this case, the *s* and *p* electrons in the ligand orbitals contribute to the anisotropic Fermi contact term by way of a non-traceless contribution to the overall ligand hyperfine interaction.[19] In conjecture, it could be said that the Co(II) hyperfine magnitude is dependent on distance of these *s* and *p* electron orbitals from the Co(II) nucleus because of their Fermi contact contribution. However, determinations as such are beyond the scope this work.

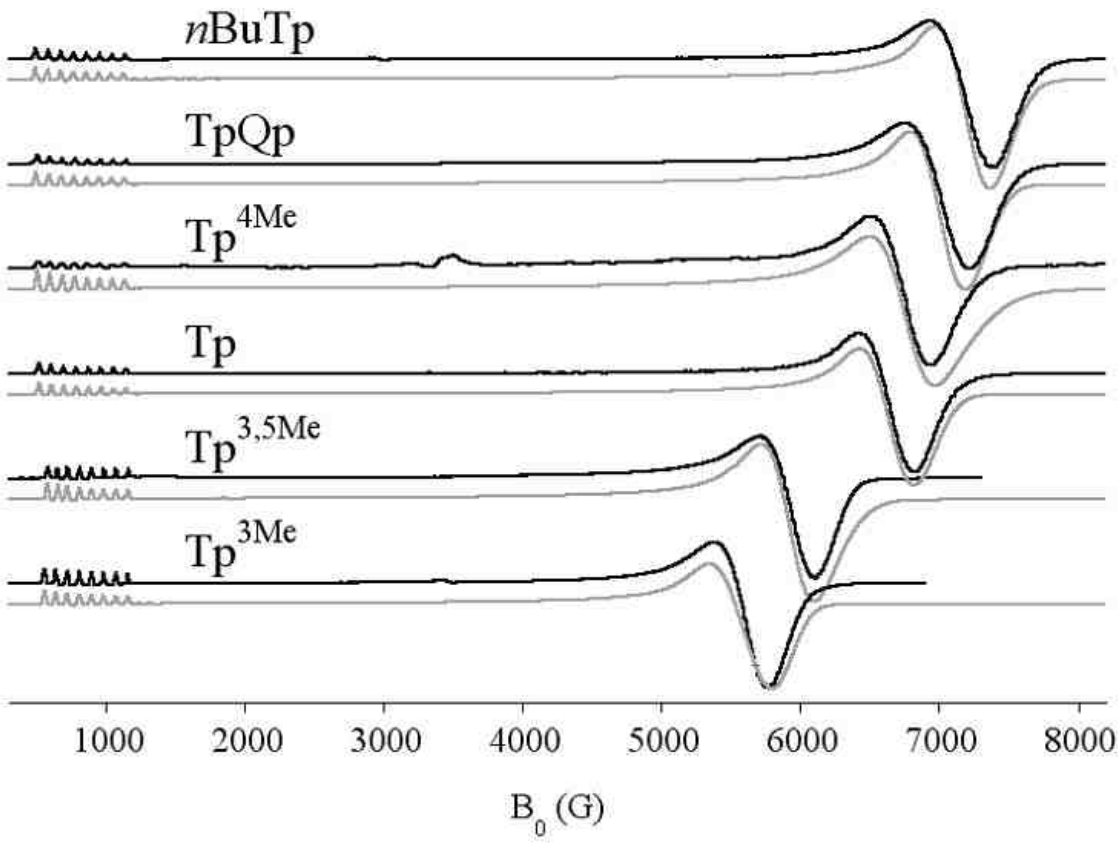

Figure 2.7 Experimental X-Band EPR spectra (black) and XSophe simulations (grey), for a series of bistrispyrazolylborate Co(II) compounds. Adapted from Myers et al.[5] The signal at g=2 is postulated to arise from an expected parallel mode transition. An alternative explanation is a signal arising from a trace amount of another metal ion, such as Cu(II).

The three trends in the experimental X-band EPR data were simulated and the results are tabulated in Table 2.2. Simulated spectra and experimental spectra may be compared in Figure 2.7. Under the simulation regimen of **S2**, the decrease in the value of $g_{\|}$ is well represented in the change of g_z. The magnitude of this change is 0.11, and it is different from the experimental change of 0.16. This difference may be explained by a careful examination of Figure 2.6, where varying E/D makes a slight change in $g_{\|}$ in addition to the more noticeable change in $g_{\perp}$. Increasing E/D decreases the apparent $g_{\|}$ and thus the required adjustment of g_{real} in Table 2.2 is less than the change observed in the experimental $g_{\|}$.

For the perpendicular direction, g_x and g_y were kept at constant values and changes to E/D were used to adjust the apparent $g_{\perp}$ in the simulated spectra. In Figure 2.7 one may see that this approach works very well. Only one compound, $Co(Tp^{4Me})_2$, had a significant difference in the line width of $g_{\perp}$, with the high field end of the derivative shape containing breadth that was difficult to simulate. Further increase of the line width would affect the low field end of the derivative. For $Co(Tp^{3Me})_2$ and $Co(Tp^{3,5Me})_2$ the line widths of the low field end of the derivative required additional line width. It is not apparent as to the reason for the difference in EPR line width. In general, the EPR line width is related to the relaxation behavior of both the electron spin-spin relaxation, or T_2, and the spin-lattice relaxation time, T_1. The overall line width is stated as the following.[34]

$$\frac{1}{T_2} = \frac{1}{T_2} + \frac{1}{2T_1} \qquad \text{Eq. 2.3}$$

As with NMR, a wider line width is indicative of faster relaxation. For transition metals, line broadening effects are often due to the short relaxation times inherent to orbital

degeneracy of the ground state that is coupled to the low-lying excited states via spin-orbit coupling.[34] This is the case for octahedral Co(II) with a trigonal elongation. Full analysis of the relaxation behavior of this series of compounds could be achieved with a separate study utilizing a pulsed EPR spectrometer.

The hyperfine interaction simulations for the series generates a decrease in the magnitude of $A_{\|}$ similar to what is observed; however, for all simulations utilizing a non-zero E/D, the simulation value differs markedly from the observed value. The frequency units of the observed hyperfine value may be calculated with the following equation.

$$h\nu = g_{eff}\beta_e H \qquad \text{Eq. 2.4}$$

Here, h is Planck's constant, ν is the frequency, g_{eff} is the observed g-value central to the hyperfine feature, β_e is the electron Bohr magneton and H is the magnitude of the hyperfine interaction in magnetic field units. The observed ^{59}Co hyperfine value of 92.7±0.03 Gauss converts to a value of 1100 MHz or $366.9\text{x}10^{-4}$ cm^{-1}. This is close to the value of $335\text{x}10^{-4}$ cm^{-1} used in the simulations D and E in Figure 2.6. Using E/D as the fitting parameter (to fix the positions of spectral features), the simulation value of $A_{\|}$ is approximately one third of the observed value.

Simulations of Matrix Metalloproteinase Model Complexes

With the apparent success of the **S2** simulation approach for the bistrispyrazolylborate Co(II) compounds, the same approach was applied to a series of five coordinate Co(II) compounds. These compounds also utilized a trispyrazolylborate ligand; however, the pyrazole rings were substituted as *tris*-3-phenyl, 5-methylpyrazolylborate, or $Tp^{Ph,Me}$ in the Trofimenko notation.[3] The steric hindrance of

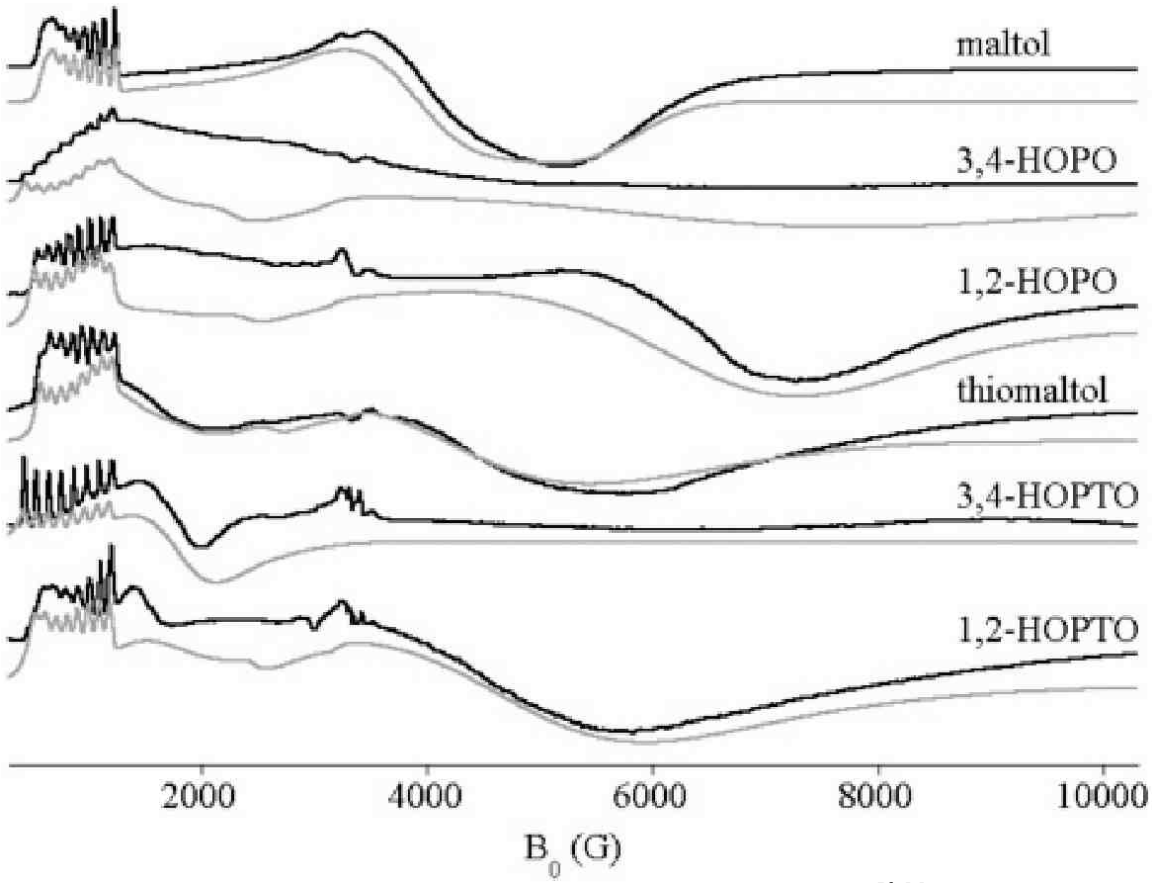

Figure 2.8 X-band EPR spectra (black lines) of [(Tp^{Ph,Me})Co(**L$_{O,O}$**)] and [(Tp^{Ph,Me})Co(**L$_{O,S}$**)] complexes and corresponding simulations (gray lines). Experimental spectra were acquired by R. Breece. Adapted from Jacobsen et al.[35]

Table 2.3 XSophe Simulation Parameter Values: [(Tp^{Ph,Me})Co(**L**)]

Compound	*g*(x)	*g*(y)	*g*(z)	D	*E*/*D*	*Az*[a]	T(K)	Cutoff[b]	L.W.	σ(x,y,z)	T.T.
Maltol	2.60	2.32	2.56	-60	0.21	110	4	20	300,100,100	1,0.1,0.005	0.565
ThioMaltol	2.60	2.26	2.52	-3.2	0.19	106	4	20	600,600,80	0.025,0.025,0.01	0.001
3,4 Hopo	2.30	2.26	2.74	-2.2	0.17	120	4	20	800,800,150	0.125,0.025,0	0.304
3,4 Hopto	2.60	2.20	2.80	-3	0.17	142	4	40	400,200,30	0.025,0.025,0.0	0.100
1,2 Hopo	2.40	2.20	2.58	-12	0.152	112	10	20	20,100,20	0.11,0.095,0.25	0.262
1,2 Hopto	2.40	2.20	2.60	-11	0.180	125	10	40	500,800,50	0.15,0.2,0	0.362

[a]in units of $1x10^{-4}cm^{-1}$

[b]Lineshape Cutoff (Gauss)

the phenyl groups prevents formation of the six coordinate bis- complex. From a four coordinate salt, various chelating groups were added.

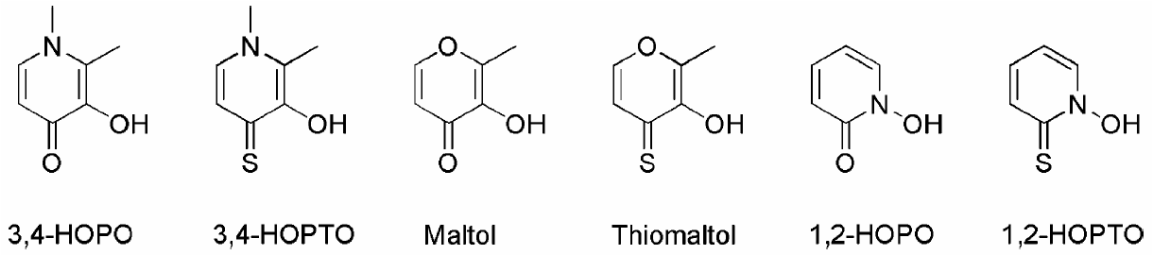

Figure 2.9 Scheme of chelators for five coordinate Co(II) compounds. Adapted from Jacobsen et al.[35]

These coordinating groups were selected as candidates for use in inhibitors of matrix metalloproteinases (MMP). They all showed a significantly higher binding constant to the trispyrazolylborate mimic of MMP than acetohydroxamic acid, which is commonly used as a metal binding group in drugs targeting MMPs, but is in fact more suited for iron ligation.[36]

As may be seen in Figure 2.8, the compounds yielded EPR spectra that contain more features than the bistrispyrazolyl borate series. They are similar, in the appearance of a ^{59}Co hyperfine feature at the low field end of the spectrum. The $g_{\perp}$ feature appears for maltol, 1,2-HOPO, thiomaltol and 1,2-HOPTO as a broad derivative feature at the high field end. In the remaining two compounds it is too broad for accurate simulations. Differences from the bistrispyrazolylborate Co(II) compounds (apart from the unexplained signal at g=2) are the derivative (thiomaltol, 3,4-HOPTO, and 1,2-HOPTO) or broad absorption (3,4-HOPO and 1,2-HOPO) feature appearing at approximately 1500

Gauss. Also, the appearance of the ^{59}Co hyperfine varies significantly for the ligands. The low field end of the hyperfine features appears to have a greater line width than the high field end of the hyperfine lines. This is most evident for maltol and 1,2-HOPTO. For 1,2-HOPO and thiomaltol the line width is narrowest in the middle of the hyperfine lines. All of these features make accurate simulations challenging.

As may be seen in Table 2.3, an exclusive use of one parameter to simulate the spectra was not possible for this series due to the number of different features. Variation in both the *g*-values and *E*/*D* was used to fit the spectra. Given that both parameters have the same effect of changing the apparent *g*-values, no unique solution may be determined from these simulations. An attempt was made to minimize the variation in g_{real} and again use *E*/*D* as the primary fitting parameter. Further complications arose in matching line widths. It was determined that line width and *g*-strain may be used interchangeably to vary the apparent line width of a feature and both were used in these simulations. Evidence of the 1500 Gauss signal was understood to arise from the $M_s=|\pm 1/2\rangle$ level, and the magnitude of *D* was decreased to allow for those transitions to occur. The fact that this upper doublet could be simulated without change to the *g*-values themselves was taken as evidence that they arose from the same chemical species. However, extensive variation of power and temperature show that these $g\sim(8.6, 1)$ and $g\sim(4,2)$ components behave differently, with the $g\sim(4,2)$ component exhibiting rapid passage or saturation behavior at low temperature and high power.[35] This saturation is most obvious in the 3,4-HOPO and 1,2-HOPO spectra. Such different saturation behavior of spectrum components is usually indicative of separate chemical origins. However, as they likely arise from two doublets of the same ion, they are required to show the same relaxation

properties. The difference in the line width requirements (aforementioned "complications") of these two components is also indicative of their different relaxation rates. In a subsequent study of a second series of compounds of the type [($Tp^{Ph,Me}$)Co(**L**)], Breece has performed separate simulations of the *g*~(4,2) and *g*~(8.6,1) components and achieved a higher degree of simulation accuracy.[37]

The ligands contain two ligating atoms, oxygen, oxygen (O,O) or oxygen, sulfur, (O,S), and either or both could coordinate to the metal. The coordination number has implications on the electronic structure. Both four coordinate tetrahedral and five coordinate trigonal bipyramidal geometries have $^4A_2$ as their ground state. A ground state of $^{2S+1}A_2$, with $S \geq 1$ is orbitally non-degenerate and correctly defined by a zero-field splitting interpretation of *D* and *E*, whose values may be determined by far-infrared spectroscopy, heat-capacity estimates, magnetic-anisotropy measurements, and high-field/high-frequency EPR.[13, 38] However, a five coordinate geometry of *hs* Co(II) that is more closely aligned with square pyramidal will have an orbitally degenerate ^4E ground state with a low-lying $^4A_2$ state.[30] The crystal structures all favor a five coordinate, square pyramidal geometry, though the small number of peaks observed by room temperature NMR implies that a Berry pseudorotation of the ligand allows for equivalence of ^1H signals from the three 3-phenyl,5-methylpyrazoles.[35]

Chapter 3

ENDOR Computer Interface

The Tierney laboratory has implemented its own ENDOR unit, which employs the program, Labview 7.1, for controlling the 0.1 to 160 MHz Programmed Test Sources (PTS) 160 RF synthesizer and for accumulating the ENDOR data. Labview is a symbolic programming language that allows the programmer to "wire" program components, represented as graphical icons, for the purpose of creating logic arguments and program structures similar to those of standard text-based languages like C++. The following section is devoted to explaining the current version of the Labview ENDOR interface.

The implementation of an ENDOR experimental apparatus in the Tierney laboratory has been an ongoing process beginning prior to the start of the author's participation in the UNM chemistry program in August 2003. The construction of a Labview interface was one of the primary goals as it predicates the ability to test the function of hardware components. An initial version of the control program became operable by the summer of 2004 and it subsequently went through over 34 revisions in the process of testing different approaches to the ENDOR experiment. The current version incorporates many of these approaches.

The front panel that allows the user to control the program may be seen in Figure 3.1. A closer inspection of the input controls may be seen in Figure 3.2. Here, the user selects values for the RF sweep parameters (start frequency, end frequency) total number of scans, resolution (number of points per MHz) number of times that the ESR output is averaged for a given MHz data point, and a delay time to wait after the change to a new RF frequency prior to the measurement of the EPR output signal.

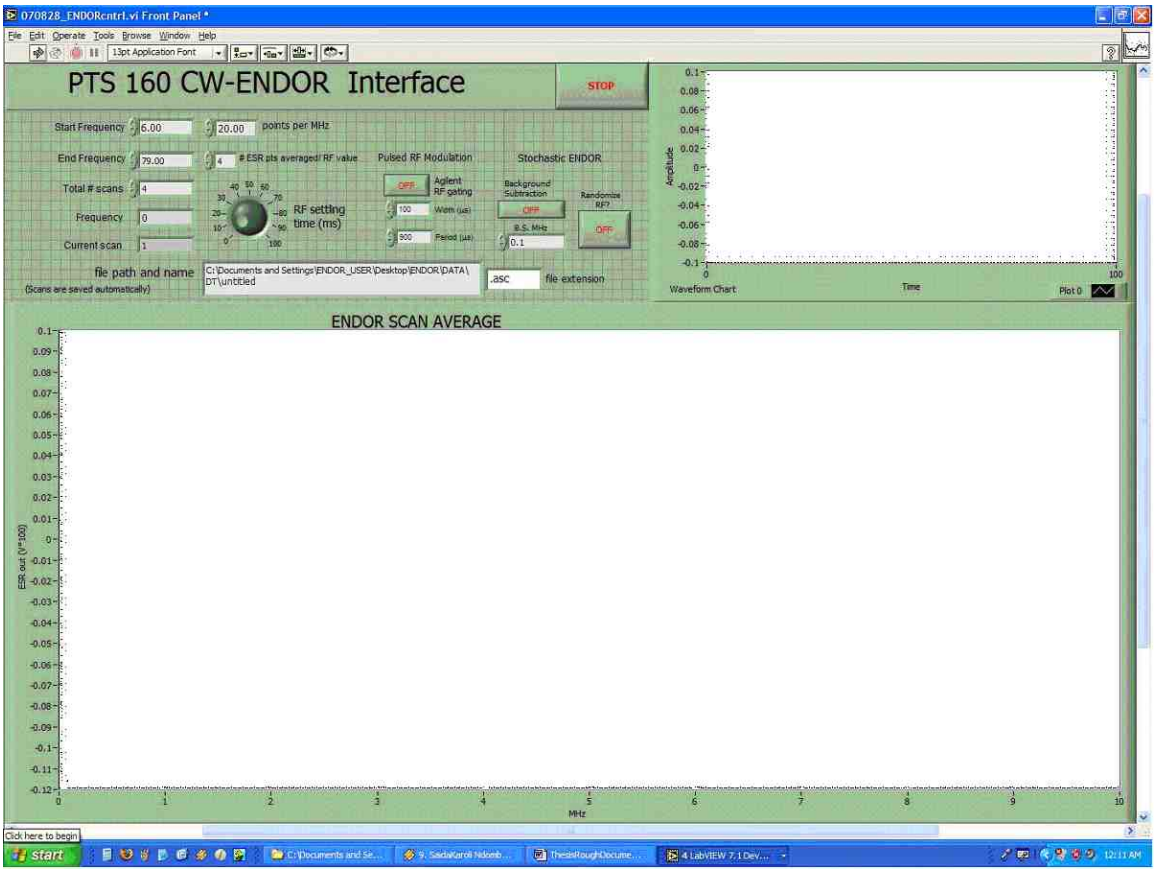

Figure 3.1. The Front Panel of the ENDOR interface. ENDOR SCAN AVERAGE and Waveform Chart windows were colored white for the dissertation.

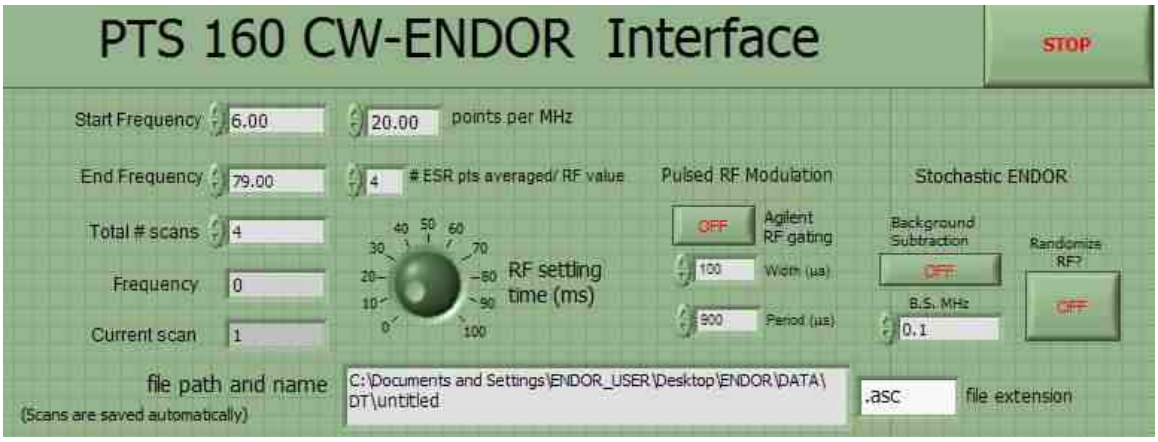

Figure 3.2 An expansion of the control parameters of the interface

They also include the file name and file extension for the output files generated.

There are three Boolean controls options. The first is to send a gating signal, assuming the user is employing a pulsed RF amplifier. The second provides the option to alternate measurement of baseline drift and signal, called "background subtraction". And finally, the third Boolean control allows a randomization of the RF array points so that they are covered in a non-linear fashion. The latter two subroutines are the basic components of the stochastic ENDOR approach detailed by Brüggemann[39]. With these controls having been set, an experiment may commence with the right-hand arrow in the upper left corner of Figure 3.1. As the experiment proceeds, information on the current frequency and scan number are displayed below the start and end frequency inputs. The current ESR output is displayed in the upper right chart recorder window (the user must pre-select the chart history length). Upon completion of a given scan, the average of all scans is displayed in the large lower window, and a file is saved with each scan number. When the overall experiment is complete, a file that is the average of all scans is generated.

The block diagram that controls the execution of the ENDOR interface may be seen in Figure 3.3. The command sequence flows along the wires in a general left to right manner. This Labview program is designed with subroutines that are symbolically represented. The subroutines will be described individually. Initial input values are on the leftmost side and are primarily directed to the main While Loop, the largest gray rectangle.

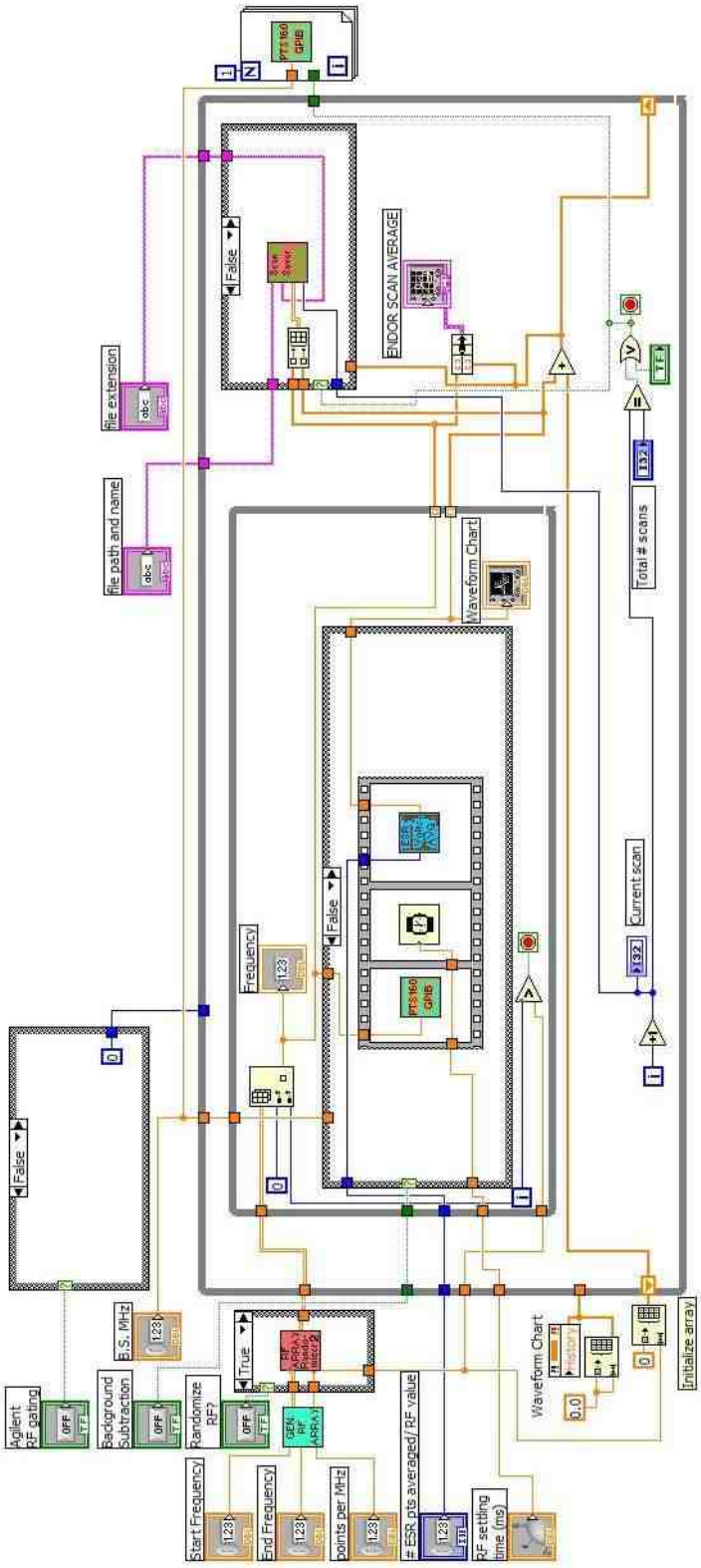

Figure 3.3 Overall interface block diagram.

The “start frequency”, “end frequency”, and “points per MHz” describe the values required for creating the RF array, which precedes the main While Loop. They are sent to the subroutine, MakeFreqArray.vi, Figure 3.4. In this subroutine, end frequency minus start frequency equals sweep range (MHz). Then the sweep range multiplied by the points per MHz gives the total number of points. The sweep range divided by the total number of points gives the array step size (MHz). There are four inputs to the While Loop. These are the start frequency, end frequency, the array step size, and initialization condition of the array. Values for the current frequency and the array index are generated in the While Loop with each iteration, via the use of Shift Registers, seen as the small downward triangle on the left and upward triangles on the right. A shift register value starts on the left, undergoes some arithmetic as it is passed through the loop routines, reaches the right register where it is saved, and is passed back to the left for the start of a subsequent iteration. Here the current frequency begins as the start frequency, it is sent to the current frequency display on the front panel and then is placed into the array index of iteration #. Then the array step size is added to the current frequency and it is passed to the shift register to store for the subsequent iteration. The stop condition of this While Loop is the current frequency as being greater than or equal to the end frequency. Thus an array[iteration #, RF value (MHz)] is created.

Two of the front panel Boolean toggles must also be set prior to the main While Loop. The Boolean values for a gating signal are sent to the top left and the randomization of the RF array on the upper left determine whether or not the subroutines are to run. The subroutine RandomizeArray2.vi, Figure 3.5., randomizes the RF array and formulates a new array. In this subroutine, the upper While Loop generates a

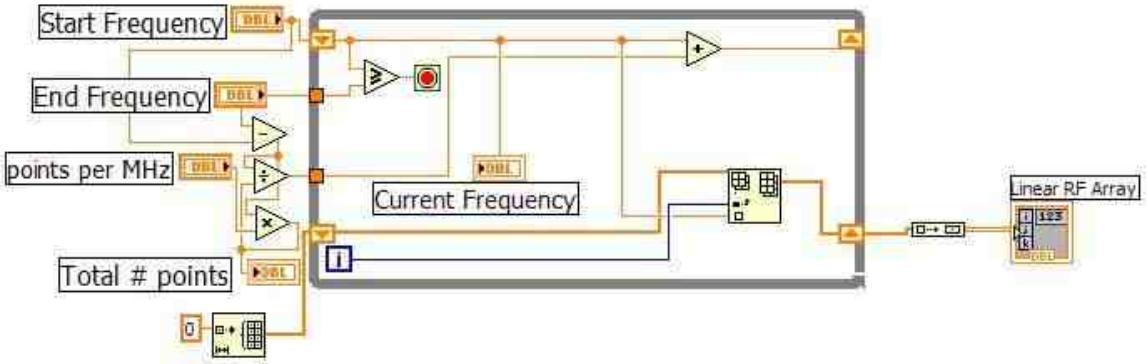

Figure 3.4 MakeFreqArray.vi generates an array of RF values.

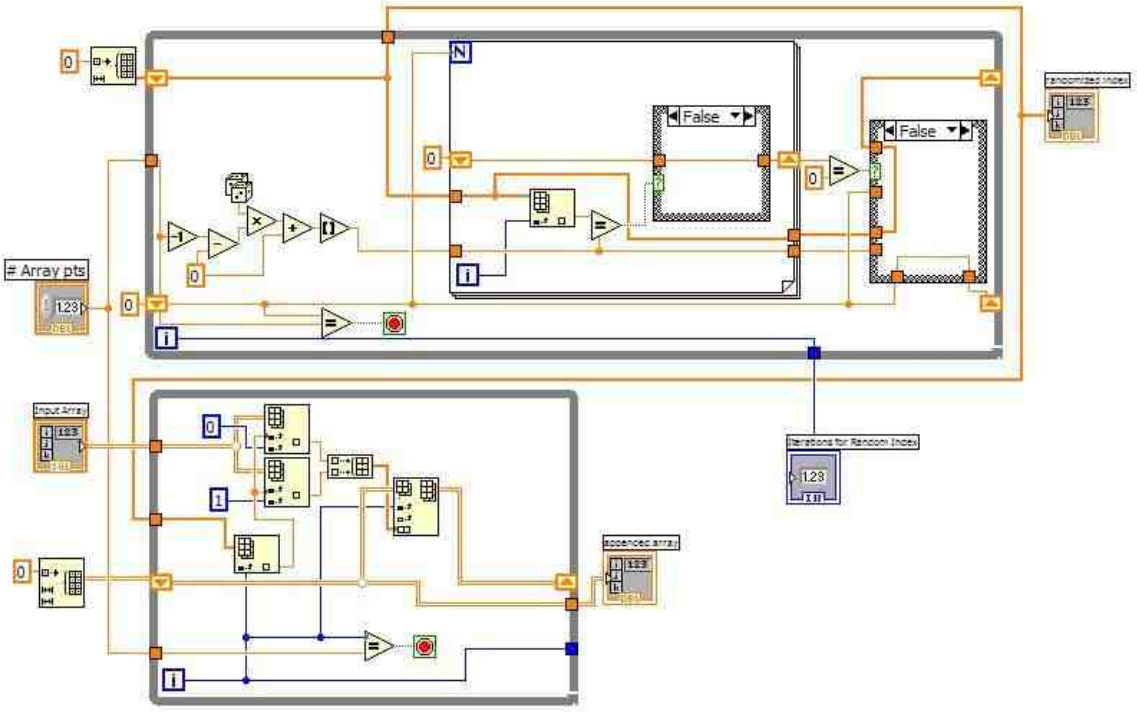

Figure 3.5 RandomizeRFArray2.vi

randomized index of the same length as total number of points in the RF array. In the second While Loop, the randomized index is used to call array elements from the original array and a new array is generated with these randomized RF values. The creation of a randomized index may require some explanation: the total number of RF array points is multiplied by a random number between zero and one. This value is rounded to the nearest integer. Then the integer is compared to all previously randomly generated integers: if it is unique, it is saved in the next available index point of the new array, and if not, the integer is discarded and a new random integer is generated in the subsequent iteration. When the new array contains all values between one and the length of the original array, the new array is passed to the second While Loop. Here, an index of the While Loop iteration is used to call a random number from the new array. The new array number then is used as an index call for the RF value of the original array. Then the While Loop iteration number and the referred RF array value are used to create the so-called randomized RF array that is used for all scans, with no subsequent modification.

Figures 3.6 and 3.7 both send General Purpose Interface Bus (GPIB) commands to RF frequency synthesizers. In Figure 3.6 the gating signal for a pulsed amplifier is declared, specifying the pulse length, pulse period and voltage level. These commands are sent once, prior to the commencement of the main While Loop, and the gating signal runs continuously, regardless of other events. The GPIB command sequence for the main RF synthesizer, the PTS 160, is seen in Figure 3.7. The “Background Subtraction” Boolean signal indicates whether or not the PTS GPIB subroutine is used once per RF point, as in Figure 3.3, or twice as in Figure 3.8, where the pre-selected background frequency point is used as a reference for baseline drift.

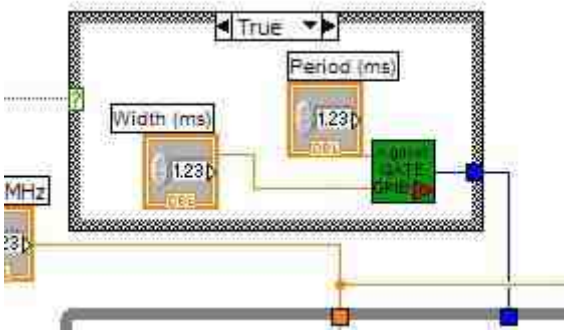

Figure 3.6 Agilent Gating with a TRUE value.

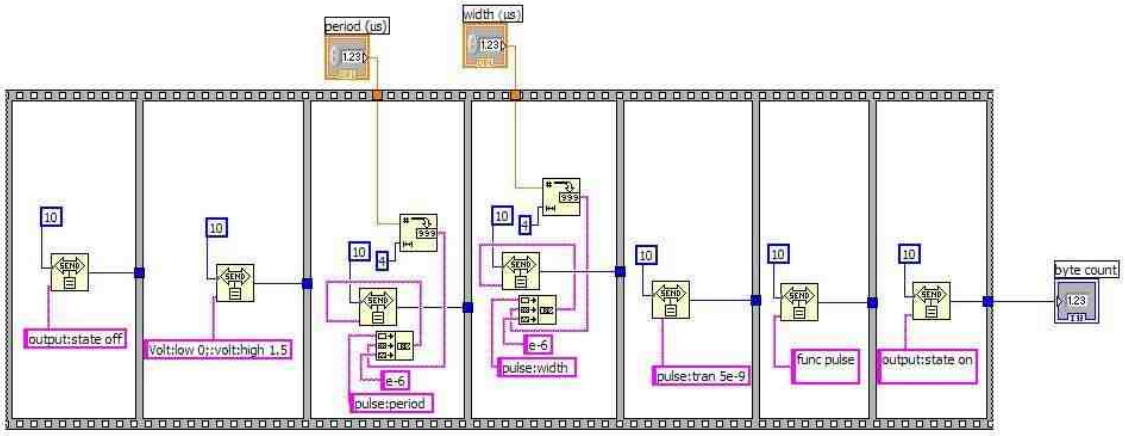

Figure 3.7 Agilent command compilation and signalling

In a similar manner, the ESR Volts AVG subroutine of Figure 3.9 may be used in Figure 3.3 once, under no Background Subtraction, and twice in Figure 3.8, with Background Subtraction. This subroutine involves an initialization of the digital acquisition card (DAC) and signal averaging routine that may repeat a selected number of times. In its current form, the user has the burden of timing this averaging process (and, in fact, the overall scan rate).

On the Front Panel, seen in Figure 3.1 and 3.2, the user pre-selects the filename and location of the output file as well as the file extension. The subroutine responsible for this, Scan Saver, Figure 3.11, has each scan saved with "_XXX" appended to the file name, where "XXX" is the scan number starting with 000 and going up to 999. The final file is the sum of all scans and it is appended with "_sum", as seen in Figure 3.12. These files are in a tab-delimited ascii format, easily accessible with a variety of spreadsheet programs.

Comparison

The laboratory of Charles Scholes employs a vintage MS-DOS program[40] for the acquisition of ENDOR data and a comparison with the above Labview program is merited. The sweep in ENDOR data acquisition has the same basic components of center frequency, sweep width, number of points and scan rate. However, where the Labview data acquisition is focused on the number of points necessary to define an ENDOR peak, *i.e.* it uses the points per MHz to the define the array size, the DOS programs is focused on maintaining the same number of array points and the scan rate. The DOS program's scheme facilitates setting the time constant on the EPR control interface with respect to the scan rate of MHz/second. With the Labview console, the experimenter must use

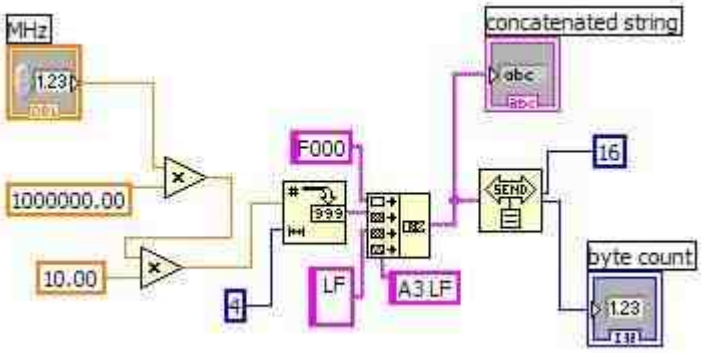

Figure 3.8 PTS 160 RF synthesizer command signaling

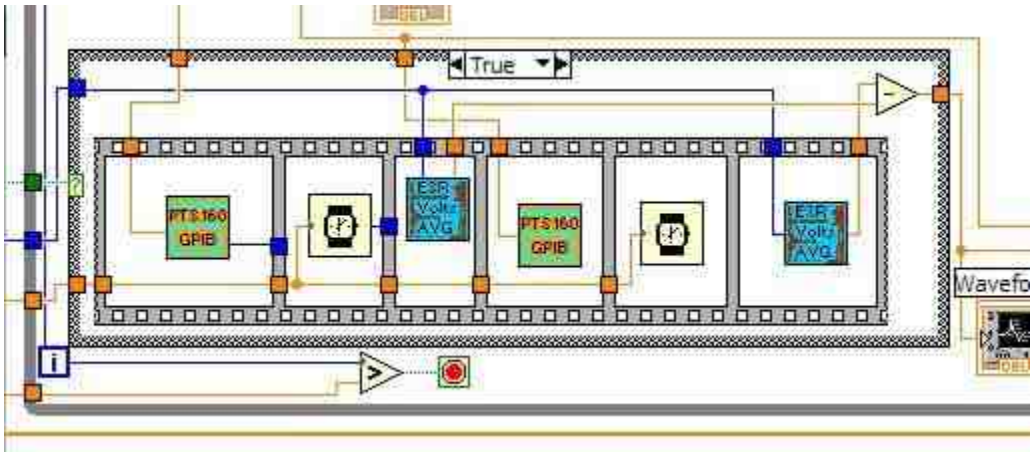

Figure 3.9 Background measurement scheme

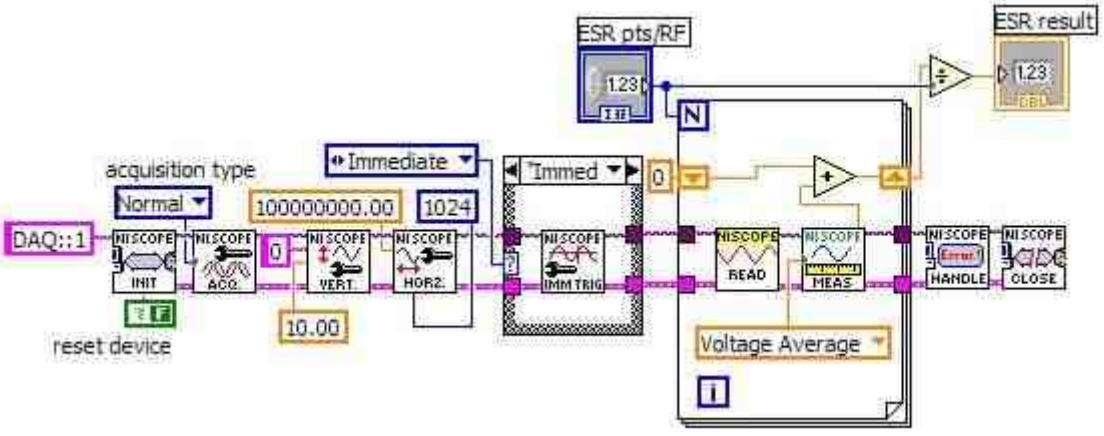

Figure 3.10 ESR signal voltage acquisition

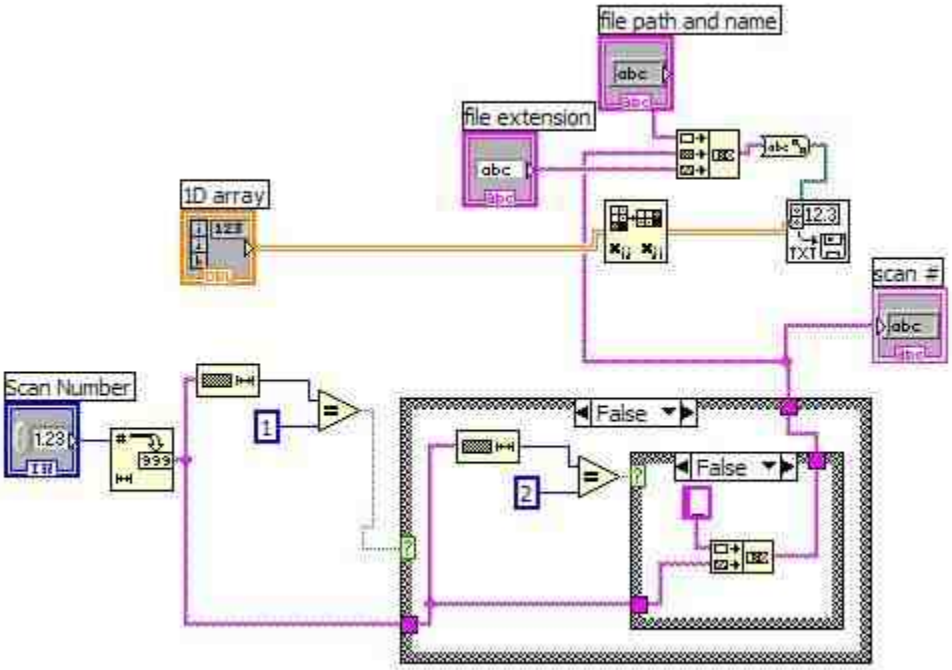

Figure 3.11 The output filename is tagged with scan number and each scan is saved.

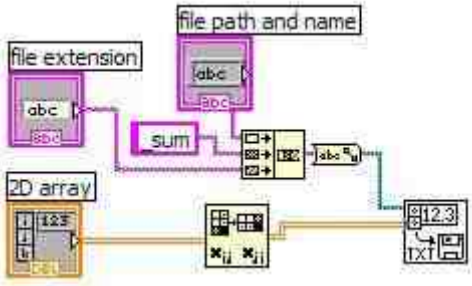

Figure 3.12 The final sweep is saved with the tag "_sum".

an external means, *e.g.* a stopwatch, to determine the scan rate. With DOS programs the internal scan rate is set. The Bruker EPR scan has two components describing its sweep rate. One is the conversion time, which is not applicable during an ENDOR experiment. The other is the time constant (tc), and it may be defined two ways. Approximately, it is a moving average of signal over given length of time. Specifically, it is the analog use of a capacitor that retains charge over a given amount of time. The time of a given scan is calculated from the scan rate. Consequently, the number of RF array points that are averaged into a single point may be determined. For example: with $Co(Tp)_2$, a typical sweep rate is 10 MHz/sec over 10 MHz (+/- 5 MHz of $\nu(^1H)$) with a time constant of 10.24 msec. For 1000 array points this amounts to approximately 10 points being used as the moving average, or 102.4 kHz averaged, one percent of the total sweep. Standard practice is to set the time constant to no more than $1/10^{th}$ the time it takes to sweep through the narrowest feature in the signal.

Chapter 4

ENDOR of $Co(Tp)_2$

Introduction

ENDOR of $Co(Tp)_2$ allows for direct measurement of the hyperfine interactions of the unpaired electrons of the Co(II) ion and the surrounding NMR-active nuclei. As a double resonance technique, ENDOR uses a single field value in an EPR signal to detect NMR transitions that occur as the RF field is swept through a nuclear larmor frequencies. An ideal ENDOR signal will have two peaks that are centered at the larmor frequency, ν_n and split by the hyperfine coupling, *A*, if the Zeeman interaction of the nucleus is greater than *A*. Alternatively, if *A* is greater than the nuclear Zeeman interaction, the ENDOR signal will be centered at *A*/2 and split by $2\nu_n$. Experiments were performed at Q-Band, 34 GHz, and X-band, 9.38 GHz, providing ^{1}H, ^{14}N and ^{11}B ENDOR patterns at both $g_{\|}$ and $g_{\perp}$, respectively. Selective substitutions with methyl groups in proton positions allowed peak assignments of several of the protons.

Despite the vital role that Zn(II) metalloenzymes play in biological systems, Co(II)-substituted enzymes have received surprisingly little attention by ENDOR spectroscopy, given the great utility of ENDOR for discerning structural information on metal-binding sites in proteins. Prior to our recent X-Band ENDOR study of the bistrispyrazolylborates,[5] only one example existed in the literature concerning high spin Co(II) in a biologically relevant environment. Walsby *et al.* substituted Co(II) for Zn(II) in a four-coordinate zinc finger, consisting of two cysteine and two histidine ligands.[41] The four coordinate Co(II) will have a different electronic ground state than six

coordinate $Co(Tp)_2$: $^4A_2$ vs. ^4E. A full angle-selected ENDOR measurement showed an intrinsic hyperfine coupling to histidine nitrogen of 21.6 MHz and this will be seen in good agreement with what was measured for $Co(Tp)_2$.

Theory

Proton ENDOR

The frequencies of proton features, $\nu_{H,ENDOR}$, center to first order at the free proton nuclear Zeeman frequency, ν_H. At Q-band when ν_e=34.1GHz, $g_{\|}$=8.5 occurs at H=2860G, and ν_H=12.2 MHz. At X-band when ν_e=9.4GHz, $g_{\perp}$=1.02 occurs at H=6585G, then ν_H=28 MHz. Taking *A* as the hyperfine coupling, one finds the ENDOR features are split away from ν_H by $\pm A/2$ for protons coupled to the *S'*=1/2 doublet. Proton ENDOR frequencies, occurring as "+" and "-" Zeeman branches are:[42]

$$\nu_H{}^{\pm}{}_{ENDOR} = |\nu_H \pm A/2| \qquad \text{Eq. 4.1}$$

Under rapid passage conditions the intensities of the "+" and "-" branches need not be the same.[42-45] When $\nu_H > A/2$, the proton ENDOR frequencies increase with ν_H as the magnetic field H increases, although the features of the "+" and "-" Zeeman branches need not occur with equal intensity.

Nitrogen ENDOR

The first order expressions for I=1 ^{14}N ENDOR are:

$$\nu^{+}(^{14}\mathrm{N})_{ENDOR} = \left|A(^{14}\mathrm{N})/2 \pm 3/2\mathrm{P} + \nu(^{14}\mathrm{N})\right|$$

$$\nu^{-}(^{14}\mathrm{N})_{ENDOR} = \left|A(^{14}\mathrm{N})/2 \pm 3/2\mathrm{P} - \nu(^{14}\mathrm{N})\right| \qquad \text{Eq. 4.2}$$

Here $A(^{14}\mathrm{N})$ is the hyperfine coupling, P the quadrupolar coupling, and $\nu(^{14}\mathrm{N})$ (=0.88 MHz at 2860G and 2.03 MHz at 6585G) is the ^{14}N nuclear Zeeman frequency. The quadrupole splitting will be 3|P|, if resolved. The $\nu^{+}(^{14}\mathrm{N})_{\mathrm{ENDOR}}$ branch is often the only one observed in rapid passage Q-band ENDOR as previously demonstrated for heme and histidine with couplings less than 30 MHz.[45, 46]

Boron ENDOR

The first order expressions for I=3/2 ^{11}B ENDOR frequencies are:

$$\nu^{+}(^{11}\mathrm{B})_{ENDOR} = \left|A(^{11}\mathrm{B})/2 \pm 2\mathrm{P} + \nu(^{11}\mathrm{B})\right|, \left|A(^{11}\mathrm{B})/2 + \nu(^{11}\mathrm{B})\right|$$
$$\nu^{-}(^{11}\mathrm{B})_{ENDOR} = \left|A(^{11}\mathrm{B})/2 \pm 2\mathrm{P} - \nu(^{11}\mathrm{B})\right|, \left|A(^{11}\mathrm{B})/2 - \nu(^{11}\mathrm{B})\right| \qquad \text{Eq. 4.3}$$

Here $A(^{11}\mathrm{B})$ is the ^{11}B hyperfine coupling, P, the quadrupolar coupling, and $\nu(^{11}\mathrm{B})$ (=3.908 MHz at 2860G and 9 MHz at 6585G) is the ^{11}B nuclear Zeeman frequency. For the particular case at $g_{\|}$ in Q-band, A/2 and ν nearly cancel so that the $\nu^{-}(^{11}\mathrm{B})_{\mathrm{ENDOR}}$ features occur at very low frequency and are not observed. This means that ^{11}B will show three features centered at $\left|A(^{11}\mathrm{B})/2 + \nu(^{11}\mathrm{B})\right|$ and split from each other by 2|P|.

Anisotropic Fermi Contact

In the case of *hs* Co(II), McGarvey and Jesson have suggested that the Fermi contact interaction is anisotropic.[6, 7] The hyperfine described in the previous nuclei-specific first order ENDOR theories is the total observed hyperfine interaction, or A_{obs}. This value has two components, the dipolar interaction and the Fermi contact interaction. At the two extremes of an axial EPR signal the observed hyperfine interactions are given as the following.

$$g_{\|}: \qquad A_{\mathrm{obs}} = A_{\mathrm{dip}} + A_{\mathrm{F}} \qquad \text{Eq. 4.4}$$

$g_\perp$: $A_{obs} = -½A_{dip} + B_F$

The anisotropic Fermi contact has parallel, A_F, and perpendicular, B_F components. Their magnitude is described by the spin component of the ground state wavefunction, multiplied by the purely isotropic hyperfine interaction.

$$A_F = ½g_{S\|} A_{int} \qquad B_F = ½g_{S\perp} A_{int} \qquad \text{Eq. 4.5}$$

Using the values of *a*, *b*, and *c*, from Chapter 1, Eq. 1.3, values for the spin contributions to the *g*-values are A_F=2.88A_{int} and B_F=0.54A_{int}. However, Jesson determined $g_{S\|}$ = 5.95 and $g_{S\perp}$ = 0.87.[7] The observed Fermi contact hyperfine A_{Fermi} as measured has angular dependence of the spin moment S_z' with respect to the $g_\|$ axis as the following:

$$A_{Fermi} = A_{int}\left[\left(\frac{2.88 g_\| \cos\theta}{g_{eff}}\right)^2 + \left(\frac{0.54 g_\perp \sin\theta}{g_{eff}}\right)^2\right]^{1/2} \qquad \text{Eq. 4.6}$$

The g_{eff} is related to the angle that S_z' makes with $g_\|$ by $g_{eff} = \sqrt{(g_\| \cos\theta)^2 + (g_\perp \sin\theta)^2}$. At $g_\|$, A_{Fermi}=A_F and at $g_\perp$, A_{Fermi}=B_F.

Experimental

All chemicals were purchased from commercial sources and used without further purification. The pyrazolylborate compounds used in this study were synthesized by E. T. Niles according to literature procedures.[3] Samples for X-Band EPR were prepared in a 50:50 toluene:dichloromethane glass at 20mM. Samples for ENDOR measurements employed deuterated solvents. The concentrations were 5mM and 14mM for X- and Q-band, respectively.

X-band ENDOR was acquired at the National Biophysical EPR Center at the Medical College of Wisconsin, Milwaukee, WI, as part of a training program supervised

by Associate Professor Brian Bennett. A Bruker ELEXsys EPR instrument equipped with a Bruker SuperQ bridge and a Bruker EN 801 ENDOR resonator were used to acquire data. A Bruker ENDOR does not use field modulation. Instead, the RF undergoes frequency modulation (FM) at a rate of 25 kHz and a width of 100 kHz. Temperature for ENDOR (5K) and EPR was stabilized with an Oxford Instruments ESR-900 liquid He cryostat.

Q-band ENDOR was acquired in the laboratory of Professor Charles Scholes in the Chemistry Department of the University at Albany, State University of New York (SUNY-Albany), Albany, NY. A schematic of the overall SUNY ENDOR instrument is included in Appendix II. On this instrument, the radio frequency (RF)-induced change in the rapid passage, 100 kHz field-modulated dispersion EPR signal is monitored as the frequency of the RF is swept. The modulation phase, for ENDOR, is set to 180 degrees from an EPR acquisition, in order to detect positive features in the ENDOR spectrum. Since rapid passage ENDOR signals may be distorted in the direction of the frequency sweep by internal spin relaxation, average frequencies are obtained ideally by separate sweeps in the low to high and high to low RF directions. The temperature was stabilized at 2K in a Janis bath cryostat of superfluid He. Dr. Andrej Sienkiewicz designed the TE_{011} Q-band ENDOR resonator used in the Q-band experiments.[47]

EPR Results

The low sensitivity of ENDOR requires that the EPR transitions are saturated, (X-band) or in rapid passage (Q-band) such that the relaxation times are long. Spectra of this type are provided in Figure 4.1. The X-band EPR spectrum (Figure 4.1A) is shown over a magnetic field range of almost 10,000 gauss.

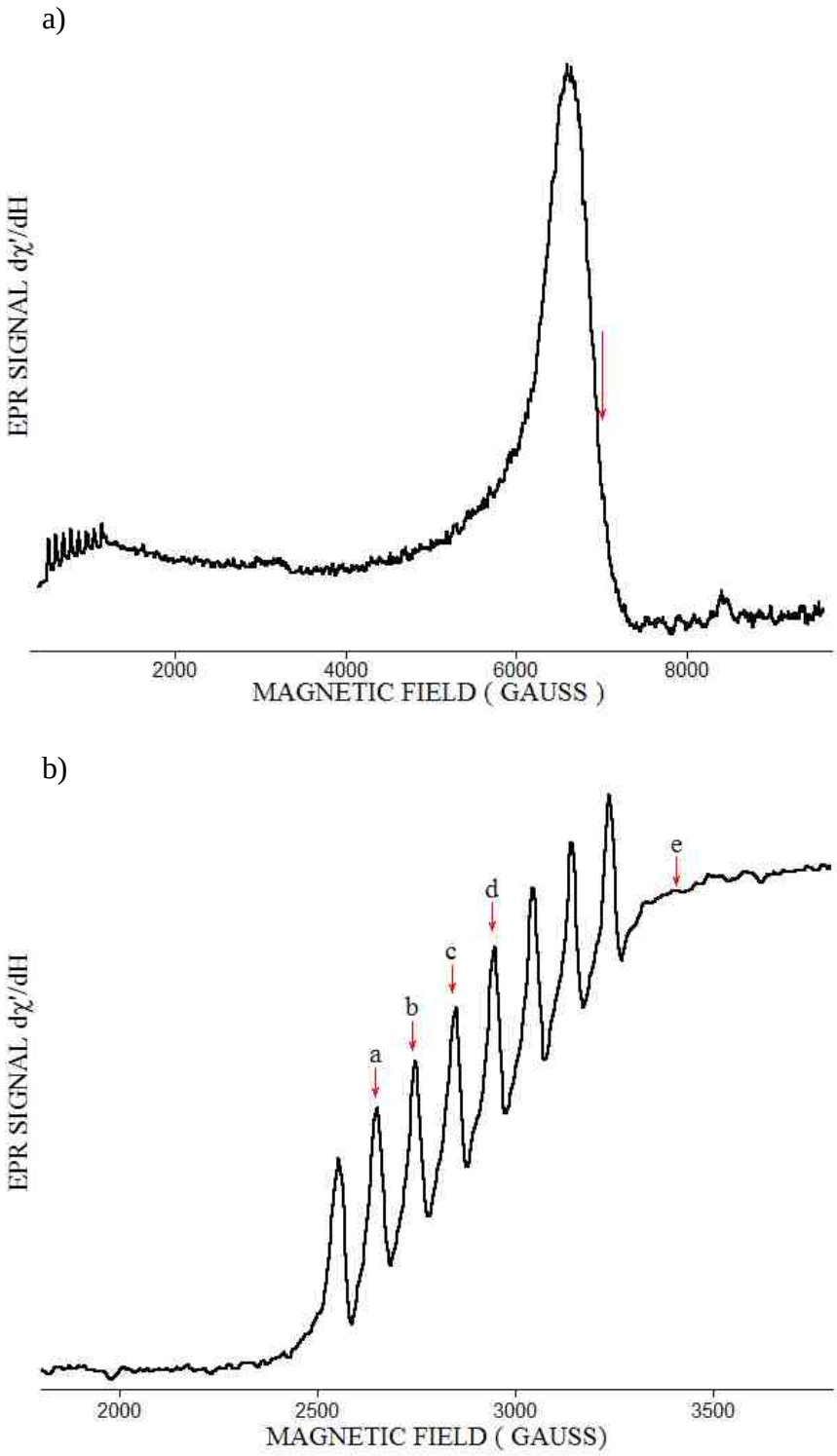

Figure 4.1. EPR spectra of $Co(Tp)_2$ at a) 9.38 GHz, 5.5K and b) 34GHz, 2K (obtained with a pumped-helium bath cryostat). The eight peaks of the Co(II) hyperfine are centered at $g_{\|}$. ENDOR was acquired at the 7000G point indicated for X-Band and the following points for Q-Band: a. 2638G; b. 2740G; c. 2834G; d. 2927G; and e. 3403G. A linear baseline was subtracted from the X-band spectrum, y=-0.0010111x+1.1654.

The high field absorption feature provides an estimate of $g_{\perp}$, 1.02, and the low field feature centers at $g_{\|}$, 8.48, showing well resolved ^{59}Co hyperfine coupling. The Q-band spectrum shows the $g_{\|}$ region in more detail with the large ^{59}Co splitting of 92.7±0.3 gauss (=1100 MHz). The best resolved ENDOR spectra were taken on the $g_{\|}$ feature, which provides well resolved single-crystal-like ENDOR spectra because it is at the unique *g*-value.[48] However, because of the large *g*-value anisotropy, the underlying EPR intensity in the $g_{\|}$ region, on which the ENDOR signal depends, is small, and one needs the greater sensitivity of rapid passage Q-band ENDOR at pumped helium temperature (versus frequency modulated X-band ENDOR at 5 K[5]) to obtain the sensitivity for doing ENDOR at $g_{\|}$.

Peak Assignments: proton and nitrogen

In CW ENDOR, there are two common methods of identifying the origins of signals. First, one may simply acquire spectra at a variety of field positions and peaks will move according to the Larmor frequencies of the nuclei from which they originate. Figure 4.2 shows this approach with shifts of H_0 by about 95 G within the hyperfine region and an additional point above the hyperfine region. The proton features are centered at the proton Larmor frequency and remain so as the field is changed. In general, ENDOR signal intensity is proportional to the intensity of the EPR signal. Consequently, the requisite number of scans greatly increases as the field is located at the lowest field hyperfine values. For the extreme hyperfine line of 2550 gauss, no ENDOR signal could be observed within 25% of the time spent signal-averaging on the next hyperfine value of 2645. However, the available EPR intensity beyond the *g*-value

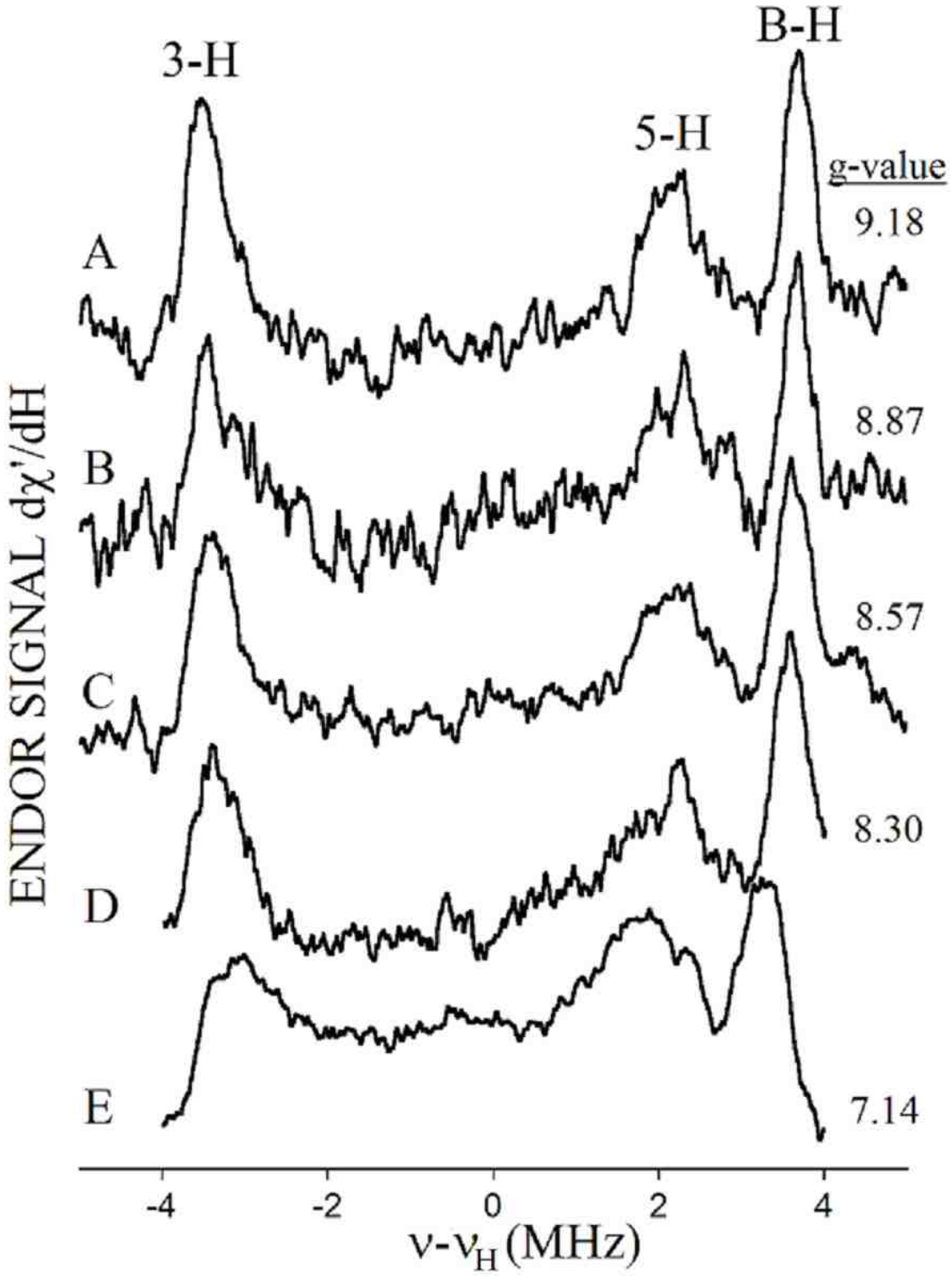

Figure 4.2 Q-Band ENDOR acquired in positions corresponding to Figure 4.1b. Data was acquired in the low to high sweep direction only.

allows the greatest resolution in the ENDOR spectra. When the sweep width and center frequency are changed to focus on the ν_H^+ region, the same change of about 105 G leads to two peaks moving as would be expected of protons, seen in Figure 4.3. The peaks between 16 and 18 MHz remain essentially stationary. This behavior identifies them to originate from ^{14}N, centered at $A/2$ and split by twice $^{14}\nu$. The observed two peaks are expected to be the $\nu^+(^{14}\mathrm{N})_{\mathrm{ENDOR}}$ branch split by the quadrupole coupling of the ^{14}N nucleus. As seen in Figure 4.4, full separation of the nitrogen peaks from the protons is not achieved until g=3.47 due to broadening of the ^{14}N signal. A similar set of measurements and observations was made with $Co(Tp^{3Me})_2$ and may be seen in the Figure A3.1.

To distinguish between nuclei that are of the same type, but are chemically distinct, one may perform isotopic substitution. Standard methods include substituting ^{1}H with ^{2}H or ^{19}F and ^{14}N with ^{15}N for identification purposes. Selective substitution of protons by more distant methyl or alkyl groups was used to attenuate the dipolar couplings to the original α-protons, since the substituent will be more distant by at least an additional C-C bond. In addition, such alkyl substitutions would diminish any Fermi contact contribution, when its source is bonding through the sigma skeleton. The relevant structures were depicted in Figure 1.1: $Co(Tp)_2$, which is the starting *bis*trispyrazolylborate Co(II) complex and the major focus of this work, $Co(n\mathrm{BuTp})_2$, which has the apical B-H protons replaced by *n*-butyl groups, and $Co(Tp^{3Me})_2$, which has the 3-H protons replaced by 3-Me groups. In the case of the *bis*trispyrazolylborates, the overall structure undergoes minimal perturbation, such that only the protons of the

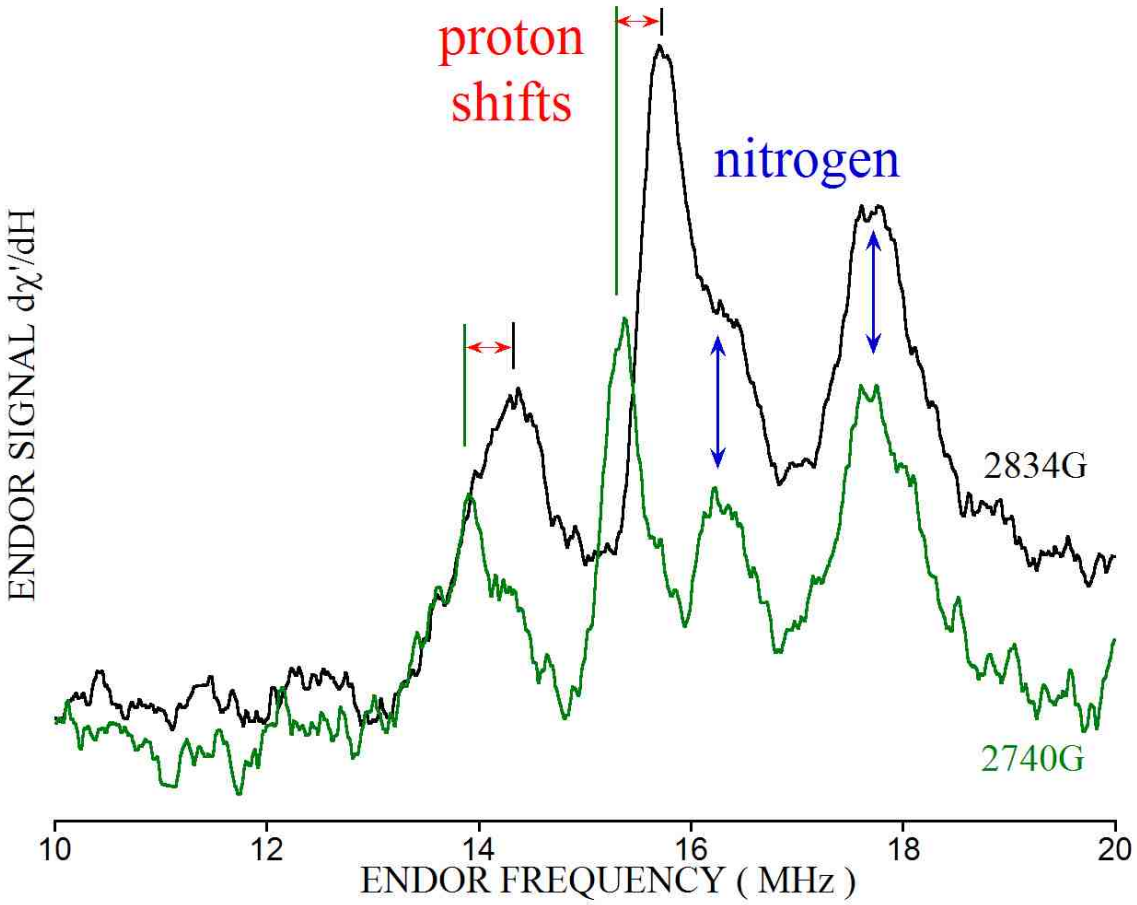

Figure 4.3 The ^{14}N peaks are centered at $A/2+\nu(^{14}N)$ and are less sensitive to changes in H_0 than ^{1}H, which are centered at ν_H.

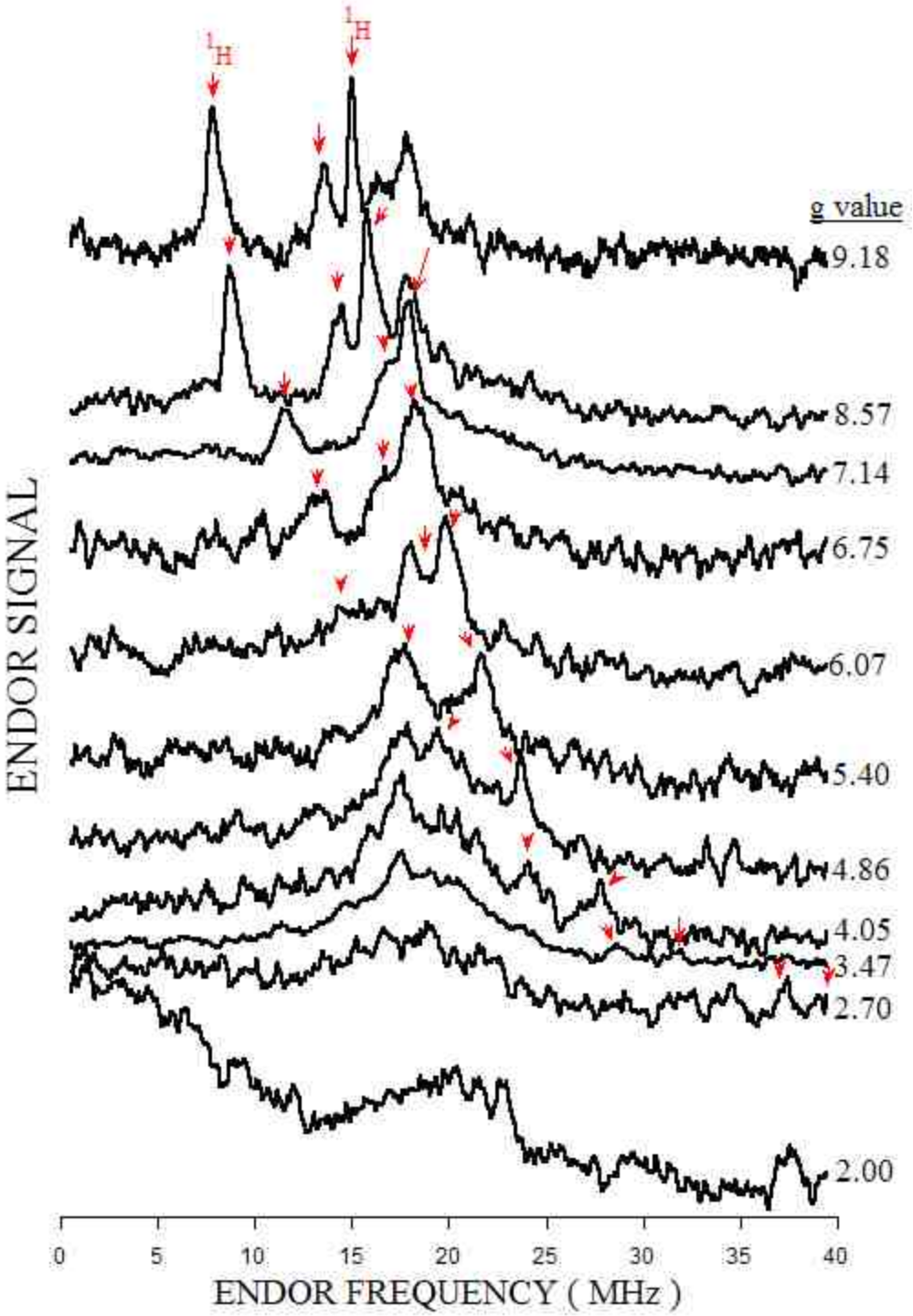

Figure 4.4 The coordinated nitrogen gives rise to broad peaks at 17 MHz that remains constant, while the proton peaks, indicated with red arrows, pass through. This broad peak is similar to what was observed for coordinating nitrogen Cu(imidazole)$_4$, one of the few studies transition metal – imidazole ENDOR.[49]

methyl substitutions are expected to change significantly from the proton hyperfine couplings of the parent complex.

Figure 4.5 provides a comparison of ENDOR spectra from $Co(Tp)_2$, $Co(n\text{BuTp})_2$, and $Co(Tp^{3Me})_2$. Proton ENDOR spectra will be centered at the proton Zeeman frequency, ν_H, as indicated by Eq. 4.1, but both predicted Zeeman partners in Eq. 4.1 need not be observed under rapid passage ENDOR conditions. It is sufficient for assignment and for computation of proton hyperfine couplings, to have only one of the Zeeman partners present.

Since only one type of proton is changed at a time, the proton feature that disappears and is replaced by a feature of smaller coupling will be the proton which we are attempting to assign. The feature labeled 3-H changed when replaced by 3-Me. The magnitude of the coupling reduced from 7.1 MHz to 5.25 MHz that has been substituted. The feature labeled B-H changed when replaced by an *n*-butyl group. The magnitude for the coupling for B-H was 7.15 MHz and was reduced to 3.7 MHz for the nearest α-CH_2 protons of *n*-butyl. The couplings responsible for these features are noted in Table 1. Proton ENDOR spectra taken over a narrower frequency range, providing more detail of the individual proton peaks is seen in Figure 4.2. As outlined in the discussion of dipolar couplings for the B-H and the 3-H protons, the metal-to-proton vector (**R** in Eq. 4.8) will be parallel and nearly perpendicular to the $g_{\|}$ axis. For these two cases the *g*-tensor and the proton hyperfine tensors have collinear principal axes, giving good spectral resolution at $g_{\|}$ of B-H and 3-H.

Table 4.1 Hyperfine values at $g_{||}$

Atom	$\|A_{obs}\|$	$\theta^{\dagger}$	R(Å)	$A_{dip}{}^{\ddagger}$	$A_{dip}{}^{*}$	A_{obs}-$\|A_{dip}\|^{\ddagger}$ *aniso*	A_{obs}-$\|A_{dip}\|^{*}$ *iso*	A_{iso} *from NMR*
3-H	7.1±0.1	84	3.44	-6.04	-5.17	1.06	1.93	-0.27
4-H	--	61	5.21	-0.53	-0.45	--	n/a	1.94
5-H	3.2±0.3	33	5.04	2.20	1.89	1.0	1.31	1.07
B-H	6.9±0.1	0	4.35	6.18	5.28	0.72	1.62	1.27
3-Me	5.25±0.3	92	3.73	-4.88	-4.17	0.37	1.08	--
B-*n*Bu (α-CH_2)	3.8±0.1	7	5.25	3.44	2.94	0.44	0.86	--
^{11}B	5.58±0.05	0	3.2	4.98	4.26	0.6	1.36	--
1-^{14}N	--	28.5	3.02	0.88	0.75	--	n/a	--
2-^{14}N	34.0±0.3	52	2.124	0.26	0.22	33.26	33.78	--

$^{\dagger}\theta$=angle from $g_{||}$ (B··Co··B) axis in degrees.

‡ For ^{1}H, $A_{dip}=(f_{Co}g_{eff}g_n\beta_e\beta_n/(hr^3))(3\cos^2\theta-1) = (39.5f_{Co}8.48/r^3)(3\cos^2\theta-1)$, as in Eq. 4.10. Respective g_n values for ^{11}B & ^{14}N were used. With an anisotropic Fermi contact, $f_{Co}=0.76$.

* Assuming a purely isotropic Fermi contact interation, $f_{Co}=0.65$.

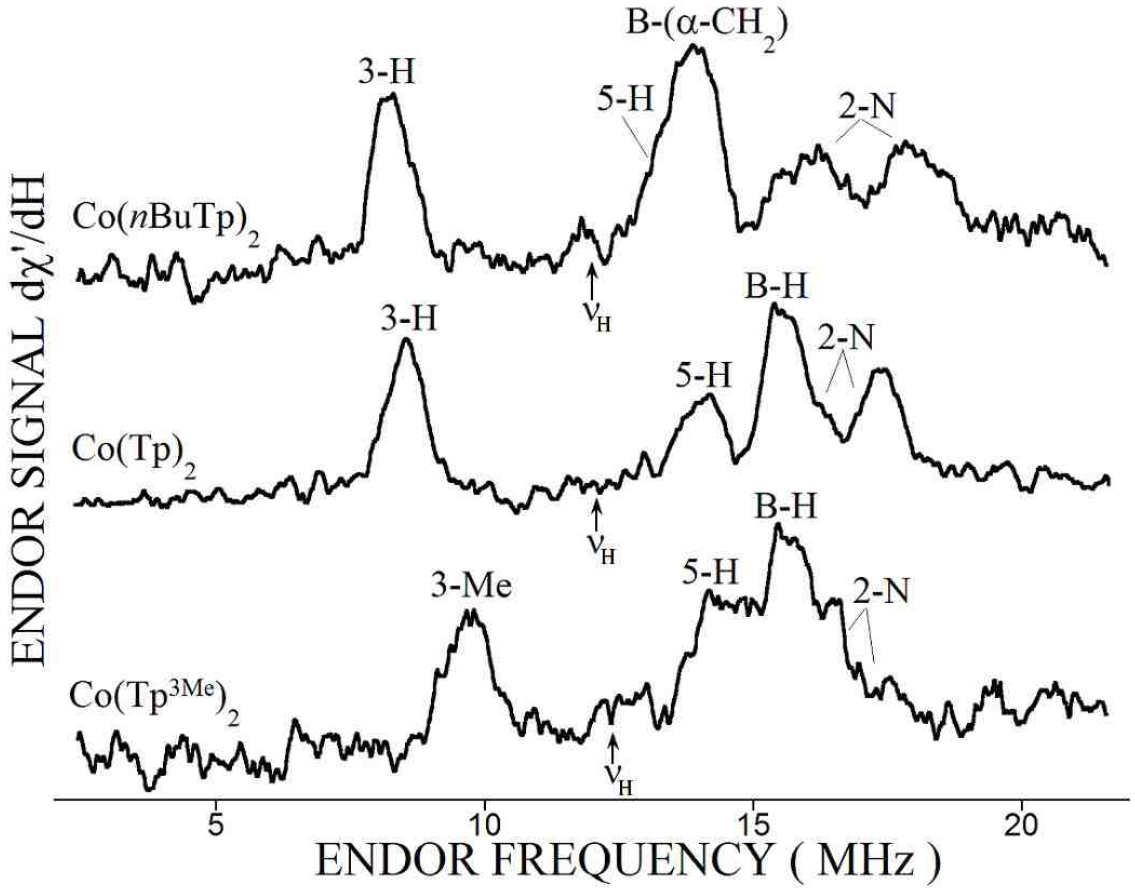

Figure 4.5. Selective substitutions of protons with methyl groups attenuates the Fermi contact hyperfine interaction, allowing identification of peaks. Note that the B-H and 5-H peaks originate from ν^+ and the 3-H is from ν^-. The slight increase of the 3-H hyperfine relative to $Co(Tp)_2$ is mirrored in the small change observed in the paramagnetic NMR shift.[5]

There are two other protons on the pyrazolyl group, 4-H and 5-H, for which the metal proton vectors are neither parallel nor perpendicular to the $g_{\|}$ axis. Non-collinear axes are expected to result in broadened ENDOR spectra.[48] The **R** vector of 4-H makes an angle close to the magic angle with respect to the $g_{\|}$ direction, and would have little dipolar coupling. The 5-H lies with its **R** vector at about 33 degrees to $g_{\|}$ and is expected to have a dipolar coupling consistent with the 3.95 MHz coupling measured for the peak labeled 5-H in Figure 4.5. However, GENDOR v2.3[50] simulations account for the 33 degree angle with an A tensor of (5.2, 0.975, 0.975) seen in Figure A3.2.

Below the frequency where 3-H occurred, three well-resolved peaks were observed by ENDOR at a magnetic field (2927 Gauss) toward the low field end of $g_{\|}$. These features lost resolution and shifted upward in frequency when the field was changed from 2927 to 3403 Gauss. The three line pattern is indicative of a quadrupole-split I=3/2 nucleus, and the only such nucleus available is ^{11}B. The upward shift of the pattern by 0.55 ±0.04 MHz is the shift that one would expect from the nuclear magnetic moment of ^{11}B (500 Gauss causes a 0.54 MHz shift). The shift is less than the 2 MHz shift expected for protons and larger than the 0.2 MHz shift expected for ^{14}N. Thus, these features are assigned to the apical ^{11}B. As seen in Figure 4.6, they are centered at $|A/2+\nu(^{11}B)|$ with A=5.38 ±0.05 MHz and the quadrupolar splitting, 2P, along the direction of the trigonal distortion, is 0.57 MHz. Evidence that these peaks do not originate from the 3rd harmonic of the protons may be seen in Figure A.3, where increase the RF power by three dB does appear to generate 3rd harmonic features.

At X-Band, in Figure 4.7, the ^{11}B ENDOR signal is four lines as opposed the three lines observed at Q-band. Four lines may arise from the expected two sets of three

lines by overlapping the two inner peaks of each three line pattern, resulting in an intensity ratio of 1:2:2:1. The hyperfine coupling, A_{obs}, is then the distance between the two inner peaks, or 0.33 MHz. Dipolar hyperfine coupling at the orthogonal extremes is related by $A_{\|}$=-2$A_{\perp}$. If the full 5.58 MHz of A_{obs} at $g_{\|}$ is taken to be purely dipolar in origin, at $g_{\perp}$ the hyperfine expected is 0.34 MHz. In Table 1, calculation of expected coupling dipolar coupling differs from the observed value by 0.72 MHz. Allowing for an anisotropic Fermi contact coupling, A_{int}=0.135 MHz, the expected hyperfine coupling at $g_{\perp}$ is 0.475 MHz, or only slightly more than the observed value. Simulations with GENDOR at $g_{\|}$ at Q-band and $g_{\perp}$ at X-band, Figure A3.4, provide values of *A*(5.8,0.33,0.33) and P(0.2,-0.1,-0.1).

Spin Densities

It is important to differentiate between two concepts relevant to describing the distribution of the unpaired electron magnetic moment throughout a molecule of interest: spin density and spin polarization. The definition of spin density given by Bertini is the fraction of unpaired electron present multiplied by $\langle S_z \rangle$, the expectation value of S_z ($\langle S_z \rangle \propto$ the induced magnetic moment on a particle), where the presence of an unpaired electron is given by the square of the molecular orbital wavefunction in which it is contained, at a given point in space.[30] Bertini's definition of spin polarization relates the ability of core electrons surrounding a nucleus to be polarized by unpaired electrons in outer orbitals. The core spins opposite to that of the outer orbital electron would be attracted to the outer orbital electron. Core electrons of the same spin as the outer orbital

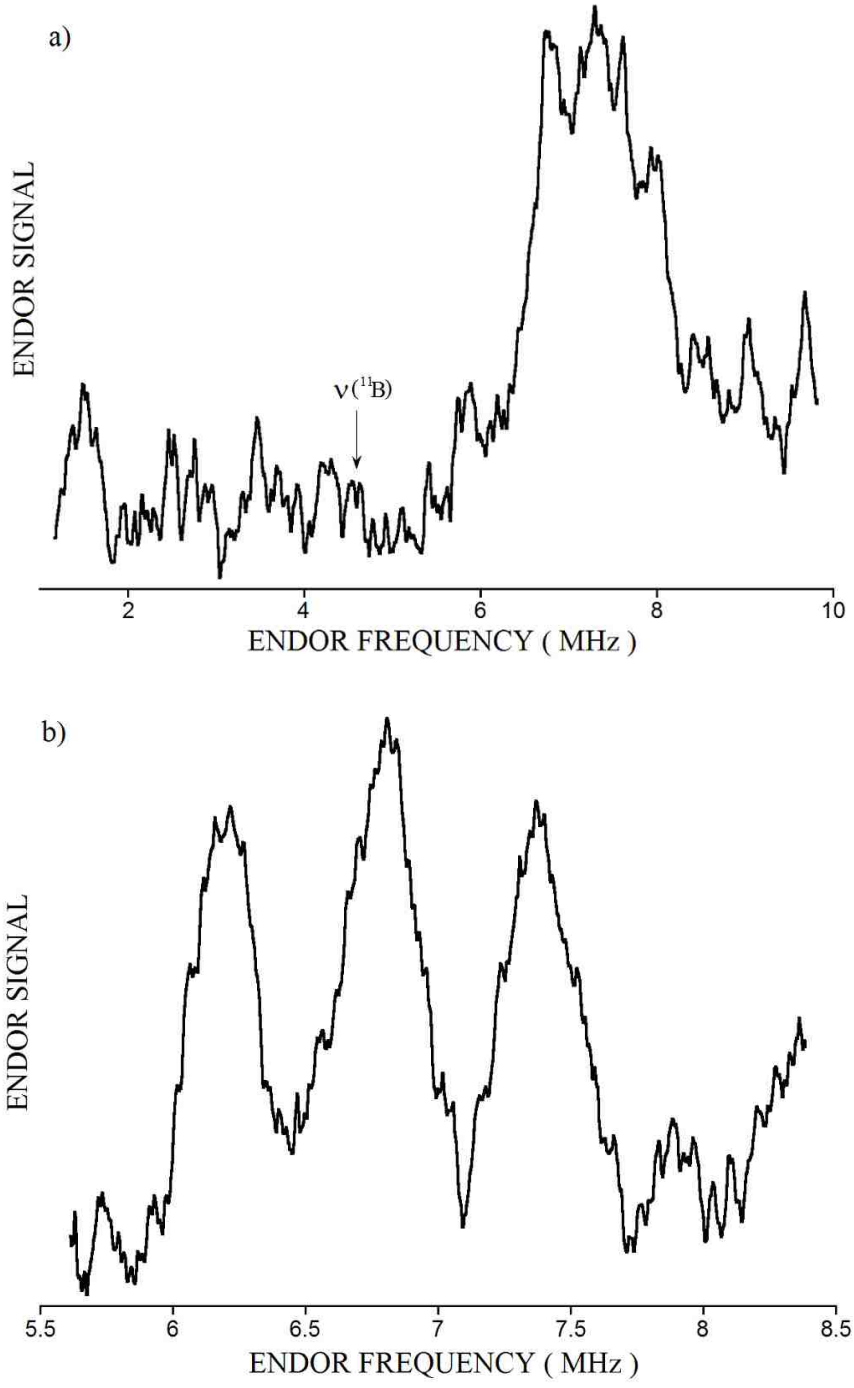

Figure 4.6 Signals from ^{11}B, a) 3403G, g=7.14 and b) 2927G, g=8.57. Acquisition conditions: a) 9 MHz/sec, 2.78hrs, b) 3 MHz/sec, 2.22hrs.

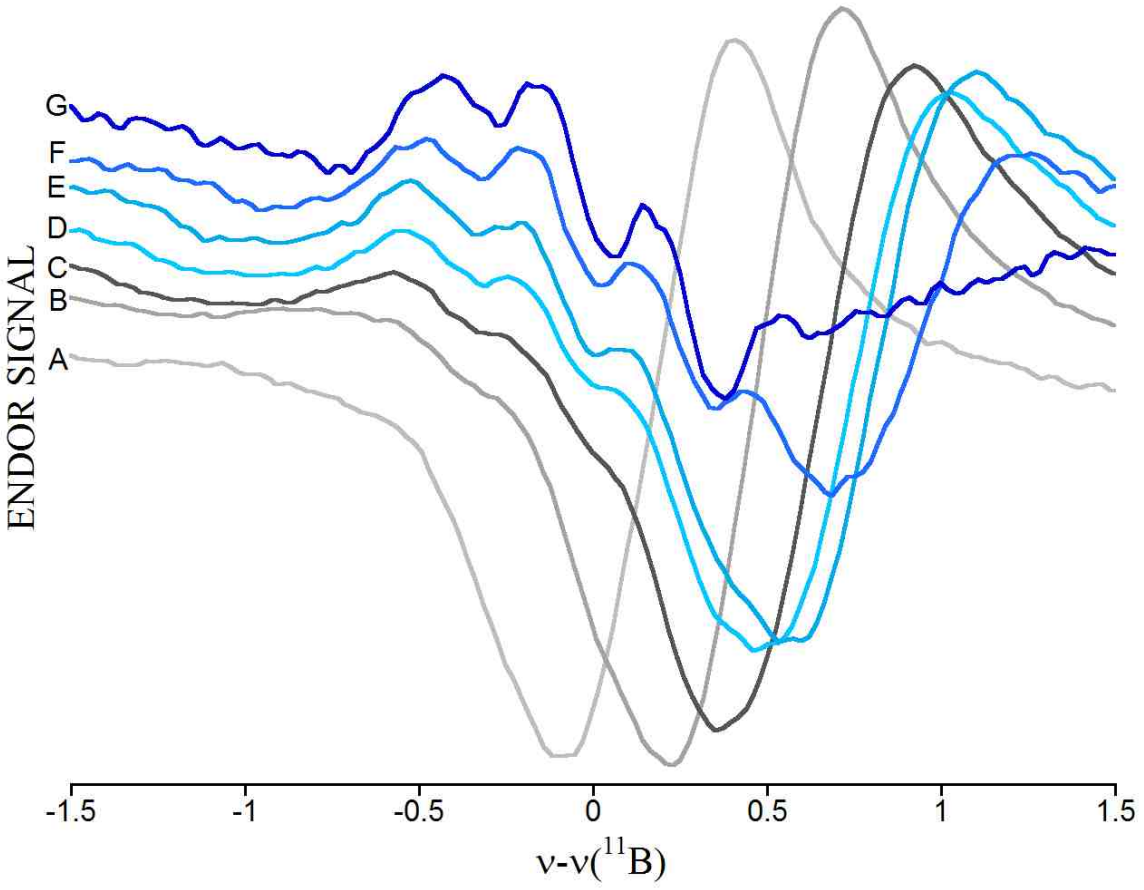

Figure 4.7 The ^{11}B region of X-Band ENDOR spectra acquired at $g_{\perp}$. A) 7044G, g=0.957; B) 6838G, g=0.986; C) 6685G, g=1.0089; D) 6605G, g=1.0212; E) 6552G, g=1.029; F) 6439G, g=1.048; G) 6244G, g=1.080.

electron would remain closer to the nucleus. The nucleus would then see a slightly non-zero electron spin moment from the particular *spin polarized* core orbital.

The common result of changing $\langle S_z \rangle$ for the nucleus makes the distinction between spin density and spin polarization appear quixotic. Indeed, recent work by Professor Dr. F. Neese has emphasized that there is a unique definition for spin density and that what EPR and NMR spectroscopists typically define as spin density is in fact spin polarization.[51] The destinction used by the said spectroscopists is that spin density is a direct exchange mechanism and spin polarization is an indirect mechanism

The coordinated nitrogen provides a signal at 17 MHz at $g_{\|}$. This may be used to calculate the spin density on each nitrogen and conversely, the fraction of spin on the central Co(II) ion. The vast majority of spin transfer with a Fermi contact interaction is expected to proceed via electron spin transfer from the $d(x^2\text{-}y^2)$ and $d(z^2)$ Co(II) orbitals to the coordinating nitrogen *2s* orbitals. It is also possible for spin to transfer from the unpaired electron in $d\pi$ orbitals to the 2-N *2p* orbitals. However, if the fraction of electron spin transfer is equivalent in both the *2s* and *2p* orbitals, the resultant Fermi contact coupling due to the spin in the *2s* orbital will be ~30 fold larger than hyperfine coupling due to the spin in the *2p* orbital.[52] The equation for determining spin density is the following.

$$A_{iso} = \rho_N \frac{A_0}{2S} \qquad \text{Eq. 4.7}$$

Here, A_{iso} is the isotropic Fermi coupling, ρ_N is the spin density, A_0 is the expected hyperfine coupling due to a full electron in the *2s* orbital, and S is the true spin moment

of 3/2. In the simplest case, the isotropic hyperfine is related to the observed hyperfine according to the following:[41]

$$\text{a)} \quad A_{obs}=g_{eff}A_{int}/g_e \qquad \text{b)} \quad A_{iso} = A_{int}(2S) \qquad \text{Eq. 4.8}$$

The Fermi coupling may be interpreted both with and without the inclusion of the predicted anisotropic Fermi contact interaction. From Weil, *et al.*,[53] $A_0(^{14}N)$ = 1809 MHz. The observed hyperfine measured at $g_{\|}$, is 34 MHz, and neglecting the ~0.3 MHz of dipolar coupling, A_{int}=8.03 MHz and A_{iso}=24.09 MHz. The spin density, ρ_N, is then 0.24, when multiplied by the number of coordinating nitrogens. Assuming a very small amount of spin density on the other atoms of the compound, the remaining fraction of spin density on Co(II), f_{Co}, is then 0.76. The anisotropic Fermi interaction predicts that at $g_{\|}$, $A_{obs}=2.88A_{int}$,[6] such that A_{int}=11.8 MHz and A_{iso} is 35.4 MHz. It follows that ρ_N is 0.35 and f_{Co} is 0.65. The predicted peak locations of both cases are shown in Figure A3.5. There are no obvious signal correlations for either case except at Q-band $g_{\|}$.

Alternatively, if the angular position of the ^{14}N nucleus with respect to the axial directions is important, simulations would be as follows. In the case of 2-N, the angle is 52 degrees from the $g_{\|}$ direction. Using simulation software, GENDOR v2.3 and EasySpin,[54] the magnitudes of $A_{\|}$ and $A_{\perp}$, were found to be 55.5±0.3 and 13.4±0.5 MHz, respectively. Both programs gave similar results. If the 55.5 MHz is treated as A_{obs} and Eq. 4.8 is used, the isotropic hyperfine is 39.3 MHz. However, if the 55.5 MHz is treated with Eq. 4.6, then A_{iso} is improbably large, 57.8 MHz. A value of 13.3 MHz at $g_{\perp}$ is three MHz in excess of the value expected from Eq. 4.5, such that the A_{iso} values of Eq. 4.8 and 4.6 are 26 and 74 MHz, respectively. Again, with the angle-dependent simulations, the A_{iso} of Eq. 4.8 produces a reasonable value and the A_{iso} from Eq. 4.6, less so. The range

of 19 to 25 MHz compares well with the A_{iso} of 21.6 MHz determined by Walsby *et al.* for the $A_{iso}(^{14}N)$ of Co(II) histidine.[41]

While not precisely reproducing the experimental spectra, these parameter values are more successful at reproducing the significant angle-selected line width changes of the 2-N signal than a simple A_{int}=34 MHz. Simulations and simulation parameter values are available in Appendix III. With the 19 MHz intrinsic value, the fraction of *2s* 2-N spin density is 0.0316. Assuming negligible spin density on the carbon and boron atoms, this leaves f_{Co}=0.81. The differing amounts of spin density determined with an isotropic or an anisotropic hyperfine may be compared in the calculation of the dipolar hyperfine couplings.

Quantizing Dipolar and Fermi Interactions

A major contribution to proton hyperfine coupling is the metal-proton dipolar coupling.

$$\mathcal{H} = 3(\boldsymbol{\mu}_e \cdot \mathbf{R})(\boldsymbol{\mu}_P \cdot \mathbf{R})/R^5 - (\boldsymbol{\mu}_e \cdot \boldsymbol{\mu}_P)/R^3 \qquad \text{Eq. 4.9}$$

Here, **R** is the metal-proton vector, $\boldsymbol{\mu}_e = \beta_e(g_{\|}S_z + g_{\perp}S_x + g_{\perp}S_y)$ and is the electronic magnetic moment that includes orbital angular momentum, and $\boldsymbol{\mu}_P = {}^{P}g\beta_n(I_z + I_x + I_y)$ is the proton nuclear magnetic moment. For the B-H and the 3-H protons studied, the metal-to-proton vector is, respectively, parallel and nearly perpendicular to the $g_{\|}$ axis. For these two cases, the g-tensor and the proton hyperfine tensors have collinear principal axes, a fact that causes good spectral resolution at $g_{\|}$. Because of the large g-anisotropy, the dipolar coupling is more than eight times larger at $g_{\|}$=8.48 than at $g_{\perp}$=1.02. The large *g*-value-dependent dipolar coupling makes the resolution of different proton features with

different dipolar couplings much better at $g_{\|}$ than at $g_{\perp}$. Calculation of the magnitude of the dipolar hyperfine interaction requires the prior calculation of the fraction of spin density on Co(II):

$$A_{dip} = (f_{Co} g_{eff} g_n \beta_e \beta_n / hR^3)(3\cos^2\theta - 1) = (39.5 f_{Co} g_{eff} / R^3)(3\cos^2\theta - 1) \text{ (MHz)} \quad \text{Eq. 4.10}$$

The symbols are as previously stated. This simple relationship was used for calculation of the dipolar hyperfine values tabulated in Table 4.1. Both cases, using an anisotropic Fermi contact and assuming a purely isotropic Fermi contact, were used in the calculation. Use of the f_{Co} from assuming an isotropic Fermi contact interaction reduced the calculated dipolar interaction to approximately 75%. As is apparent in Eq. 4.4, when the calculated dipolar interaction is subtracted from the observed hyperfine coupling the Fermi coupling remains. For the table, A_{obs} values were measured from scans that were the average position of low to high and high to low sweeps. Typical peak position adjustments were no more than 0.17 MHz.

Tierney and coworkers reported values of A_{iso} from $Co(Tp)_2$ ^1H NMR measurements in Myers *et al*.[5] These values are in the rightmost column of Table 4.1. The magnitude of the NMR-derived A_{iso} shows the better agreement with the anisotropic case for 3-H and 5-H, but the Fermi contact of B-H clearly favors the isotropic case. If the fraction of spin density on the Co(II) is treated as a variable parameter, there is no unique value that will fit the dipolar and observed hyperfine difference to the A_{iso} from NMR. To achieve a 3-H value of -0.27 MHz, f_{Co}=0.927. For the A_{iso} of B-H to be 1.27 MHz, f_{Co}=0.692. One reason given by McGarvey for why the A_{iso} of room temperature NMR data differs from that derived from ENDOR is that the room temperature NMR behavior is the sum of contributions from several different states, each with distinct *g*-

values. Indeed, Jesson calculated the energy of the first excited state as being just 206 cm^{-1} above the ground state, close to the room temperature Boltzmann energy of kT=205 cm^{-1}. The proton ENDOR signals for the 3-H and 3-Me may also be compared with the two positions, $g_{\|}$ at Q-band and $g_{\perp}$ at X-band, using Eq. 4.4 and 4.8, and resulting in two equations and two unknowns, A_{dip} and A_{iso}. For the 3-H, A_{iso} is 0.44 MHz for both an anisotropic and isotropic Fermi interaction cases, which is close the value of 0.45 MHz found by Jesson.[8] However, that value was determined from the peak of the X-band derivative line shape. If the zero point of the X-band derivative line shape is used, a much smaller value of A_{iso} results, 0.0144 MHz. Alternatively, the difference of the 3-H and 3-Me A_{obs} may be used to calculate the residual fraction of spin not on the protons and ΔA_{iso} as the two unknowns. The approach requires use of the crystallographic structural data to quantify the dipolar component, exclusive of the residual ^{59}Co spin fraction. This residual spin may then be used with Eq. 4.10 to calculate A_{iso} values. A value of A_{iso}=0.24 MHz results, which is very close to the -0.27 MHz determined by NMR. For 3-H alone and the comparison method, the spin density on the 3-H and 3-Me is less that 0.006. This small quantity supports the assumption that the vast majority of ligand spin density resides on the ligating 2-N.

The effect of methyl substitution at proton positions allows assessment of the success of Fermi contact attenuation. Regardless of anisotropy in the Fermi interaction, the magnitude of the intrinsic hyperfine interaction for 3-Me is about one half that of 3-H. Clearly, the fact that spin density is not completely attenuated, suggests, as Jesson does, that there is at least some component the Fermi contact with the ring carbons arising from *2p* π polarization of the σ electrons in the C-H bond. Pyrazole does have a conjugated π

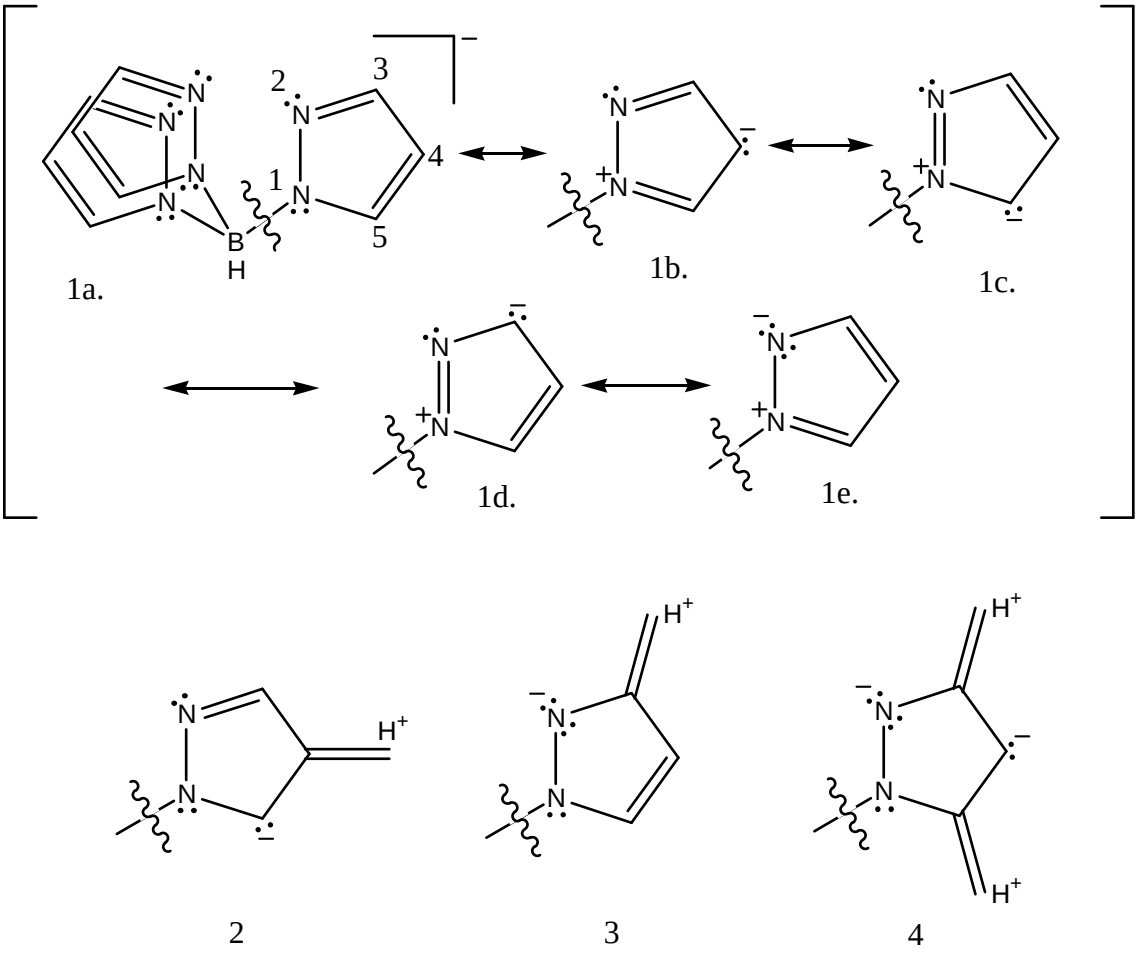

Figure 4.8 The aromaticity via "electron-pushing" in the pyrazole rings of hydrotrispyrazolylborate, 1a-e, and the hyperconjugate forms of 4-Me, 3-Me, and 3,5Me-pyrazolyl ring, 2-4 respectively.

system, and there is one electron in the $d\pi$ orbitals. Other ligands with sp^2-hybridized nitrogens coordinating a metal containing unpaired $d\pi$ electrons, such as Cr(III) pyridine and Co(II) imidazole (which pyrazole is meant to mimic), have shown π spin delocalization/ polarization as a mechanism of paramagnetic shifts by NMR.[30] As illustrated by the resonance structures in Figure 4.8, the lone pair on 1-N may propagate though all other ring positions. The propagation of spin onto the methyl comes from the pyrazole π-system to the σ electrons of the C-C bond, which subsequently polarizes the remaining sp^3 bonds of the methyl group. An alternative mechanism is through hyperconjugation of the pyrazole π system onto the methyl group as shown in Figure 4.8, 2-4. Hyperconjugation occurs through the alignment of the methyl C-H sp^3 bond with the *p*-orbitals of the adjacent sp^2-hybridized pyrazole carbon.

Conclusion

The compound $Co(Tp)_2$ has an unusual ground state with large unquenched orbital angular momentum and contributions from the quartet S=3/2 spin. The result is a highly unusual *g*-tensor: $g_{\|}$=8.48 and $g_{\perp}$=1.02. The large magnitude of $g_{\|}$ enhances dipolar couplings of protons measured near $g_{\|}$ and aids in elucidation of distances in the range of 3.5-5 Å and, indirectly, the contact interaction of these protons. A nitrogen hyperfine interaction from coordinating nitrogens of the pyrazolylborate is observed over much of the range of *g*-values. The unusual magnetic character of the ground state results in a nitrogen hyperfine interaction that appears as anisotropic, even though the underlying cause is the isotropic Fermi interaction with *2s* electron spin on the nitrogens. The underlying Fermi interaction was elucidated and the unpaired electron spin density was determined.

Chapter 5

High Frequency Nuclear Magnetic Resonance of $Co(Tp)_2$

Introduction

The first nuclear magnetic resonance (NMR) experiments operated with iron core electromagnets. We extended this method by using a modern electron paramagnetic resonance (EPR) electromagnet to perform NMR experiments in the range of 12 to 42 MHz $\nu(^1H)$. This range is possible for samples with large paramagnetic shifts, such as $Co(Tp)_2$, which has four peaks spread over a range of 300 ppm. The purpose of these measurements was to test the linearity of the T_1 values in this range.

Experimental

Sample solutions were prepared in 10 mm NMR tubes with the requisite amount of $Co(Tp)_2$ for a final concentration of 30 mM dissolved in 2.5 mL of toluene–*d8* (Sigma-Aldrich). Measurements of T_1 employed the standard inversion-recovery sequence: 180-τ-90-AQ, which is listed on the UNM ASX300 NMR console as the pulse program t1ir1d.h. Pulse length (90°) measurements were made by first assessing the 90 degree pulse length with the automated routine, *paropt*, with the *t1ir1d.h* pulse program. The recycle delay and τ times were set to one second due concerns about field stability (later determined to be unsubstantiated). The 180 degree pulse length was measured similarly, with the exception of τ having been set to the shortest value of one μsec employed in the inversion-recovery experiment. In cases where a 180 degree pulse length was not obvious it was set twice the 90 degree pulse length. At room temperature, the longest 180 degree pulse length was 28 μsec and it was 44 μsec at 237K (12% of the observed T_1

at 237K). Due the low sensitivity, pulse measurements sometimes required up to 500 scans.

The instrument involved a Bruker ASX300 NMR console connected to a Bruker 250 MHz 10mm broadband probe, with a N_2 flow cryostat dewar insert. Experiments at 237K utilized a Bruker temperature controller of Bruker AC 250 instrument. The broadband probe was set in a custom-built wooden mount in a 56mm Bruker ER 073 magnet with a Bruker ER 083 power supply that was controlled with a Bruker EMX EPR console. The orientation of the saddle coil was verified such that its RF field was positioned orthogonal to the DC magnetic field of the electromagnet. The combination of the limitation of the magnet and RF amplifier constraints, this configuration, allows a range of $\nu(^1H)$=1-64 MHz, Typically, the magnet was allowed to stabilize for more than one hour prior to commencement of experiments. Drift in the field position within the time of an experiment was not seen to be significant. A direct measurement of its drift is provided in Figure A4.1. The magnet field position was calibrated with the frequency of a sample containing protonated toluene and a small amount of waste Co(II) compounds used as a paramagnetic relaxant. Initial sweep widths of 80,000 ppm were sometimes required to locate the toluene signal. By readjusting the field from the calculated position, usually by ca. +15 Gauss, the signal was centered and the sweep width was narrowed to 1000 ppm.

Appearance of the Spectra

The ^1H lineshapes for $Co(Tp)_2$ varied significantly within the range of frequencies employed, and the trends were not consistent for all protons, Figure 5.1. For example the B-H proton is well resolved at 41 MHz and all but disappears by 12 MHz. The remaining

protons begin broad at 41.51 MHz, narrows significantly, reaching minimum FWHM at 27.38 MHz, and then broadening again at 12.54 MHz. The peak positions remain constant (toluene set to 3.5 ppm). The amount of noise in the 37.07 MHz spectrum may reflect the change of pre-amp modules, a 12-34 MHz module was changed to a 32-74 MHz module. There was a noticeable loss of sensitivity (increase scan number required) upon this change. The line widths also nearly doubled. Preliminary experiments, seen in Figure A3.2 employed a series of NMR probes that the author constructed and they also exhibited frequency-dependent changes in line width. The origin of the behavior is unknown at the time of this writing.

For NMR, line width information typically reports on the transverse relaxation, or T_2, of the species in question. A long T_2 corresponds with a slow decay in the time domain FID signal and narrow line width. A short T_2 will produce a rapid decay in the FID and a wider line width. The relation of line width to T_2 is FWHM=$1/(\pi T_2^*)$, where T_2^* is given by the following.[55]

$$\frac{1}{T_2^*} = \frac{1}{T_2} + \frac{1}{T_{2(\Delta B_0)}} \qquad \text{Eq. 5.1}$$

Here, T_2 is the true relaxation parameter and the $T_{2(\Delta B0)}$ is the relaxation due to inhomogeneity in the B_0 magnetic field. It is true that iron core magnets are designed for swept-field applications and are undoubtedly less homogeneous and less stable than modern superconducting, fixed-field NMR magnets. Recent experiments by Bruker determined that their EPR magnets have a noise of 1-3 mG and drift +/- 20 mG over one hour.[56] However, the fact that line widths increase in both the low and high field ends of the experimental range suggests that field inhomogeneity is not responsible for the line widths observed. That is, field inhomogeneity is expected to be field-independent.

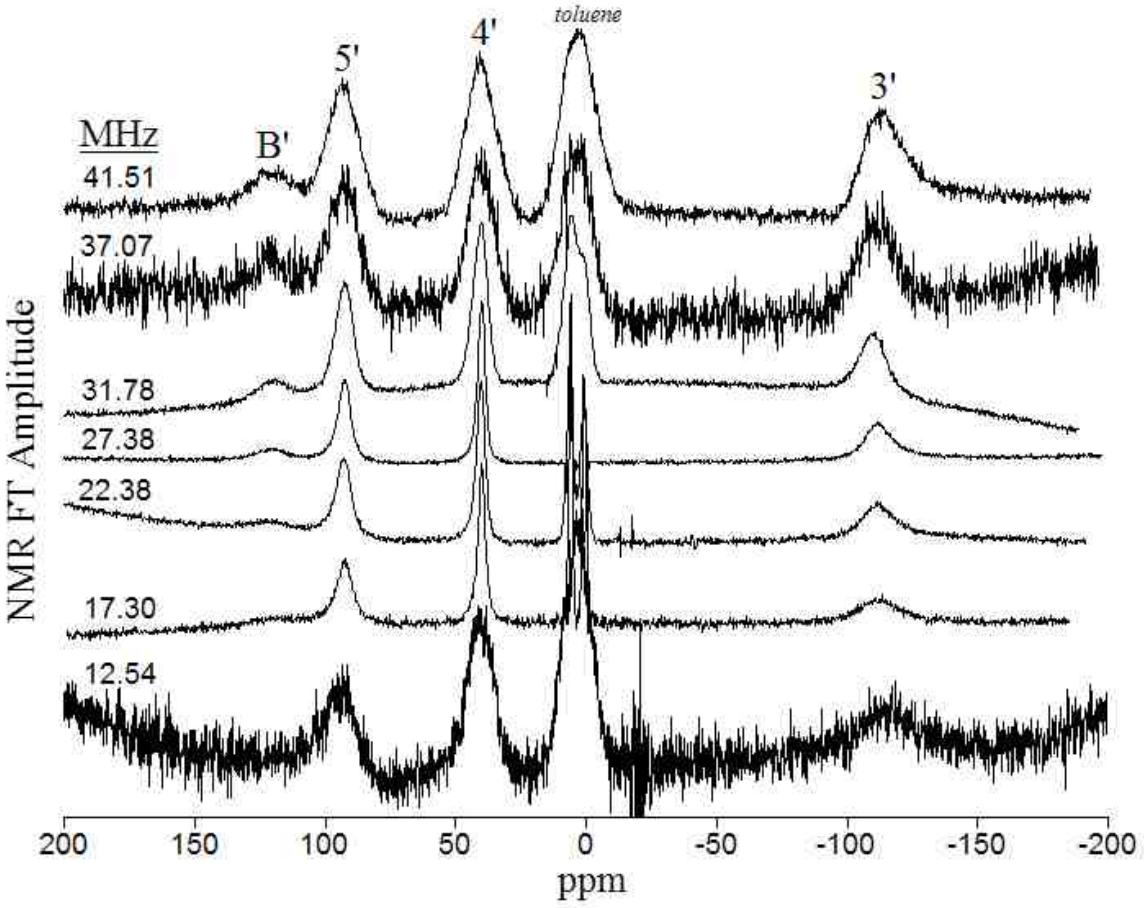

Figure 5.1 $Co(Tp)_2$ $\nu(^1H)$ NMR acquired at several frequencies, on left. The frequency domain spectra were acquired with the 180-τ-90-ACQ sequence with a sufficiently long τ value (one second) such that they essentially represent a single 90 degree pulse experiment.

The aforementioned preliminary experiments, utilizing custom probes, exhibited a different line width behavior. The greatest line widths occurred in the region of 12-18 MHz and narrowed at the extremes of the range, 10 MHz and 40 MHz. This behavior was tied to a specific probe that covered this range and contained tuning capacitors that respond to magnetic fields and thus caused field inhomogeneity. With a commercial Bruker 250 MHz broadband probe, it is not expected that field-responsive electronic components are present.

Correlation Time Calculation

The measurement of T_1 values at a number of fields allows determination of the correlation times for individual protons, which is given by the following:

$$\tau_c^{-1} = \tau_m^{-1} + \tau_r^{-1} + \tau_s^{-1} \qquad \text{Eq. 5.2}$$

The correlation time, τ_c, is a constant that relates three separate correlation times: chemical exchange, τ_m, molecular rotation, τ_r, and electronic relaxation, τ_s. The correlation time that is smallest will determine the overall value of the correlation time. For Co(II), in a small molecule ~500 g/mol, the rotation constant will be on the order of 10^{-11} sec, and in the absence of chemical exchange it is expected that the shortest time will be electronic relaxation with a value of ca. 3 x 10^{-12} sec. Accordingly, $\tau_c \sim \tau_s$. The regular Solomon equation governing relaxation of complexes where S>1/2 is the following:[30]

$$T_1^{-1} = \frac{2}{15}\left(\frac{\mu_0}{4\pi}\right)^2 \frac{\gamma_I^2 g_e^2 \mu_B^2 S(S+1)}{r^6}\left(\frac{\tau_c}{1+(\omega_I-\omega_S)^2\tau_c^2} + \frac{3\tau_c}{1+\omega_I^2\tau_c^2} + \frac{6\tau_c}{1+(\omega_I+\omega_S)^2\tau_c^2}\right) \qquad \text{Eq. 5.3}$$

Here, γ_I is the nuclear magnetogyric ratio, g_e is the free electron g-value, μ_B is the Bohr electron magneton, r is the distance from the metal center to the nucleus, ω_I is the nuclear Larmor frequency, and ω_s is the electron Larmor frequency.

The caveats with the Solomon equation are that it does not account for g-tensor anisotropy, Zero-Field Splitting of the electronic energy levels, and contributions to T_1 from the anisotropy of the Curie spin.[57-60] Among these caveats, the most important for $Co(Tp)_2$ is alteration of the equation to accommodate g-value anisotropy. This was dealt with directly by Sternlicht, with the following equation:[57]

$$T_1^{-1} = T_2^{-1} = \frac{2}{3}\frac{\gamma^2 |\beta|^2 S(S+1)}{r^6}\tau_c\left[\frac{1}{3}\left(g_{\parallel}^2 - g_{\perp}^2\right) + g_{\parallel}^2\cos^2 x + g_{\perp}^2\sin^2 x\right] + \frac{4}{9}\frac{\gamma |\beta| S(S+1)A}{r^3}\left(g_{\parallel} - g_{\perp}\right)\left(3\cos^2 x - 1\right)\tau_c\delta(\tau_c,\tau_e) + \frac{2}{3}S(S+1)A^2\tau_e \qquad \text{Eq. 5.4}$$

Here, γ is the nuclear magnetogyric ratio, $|\beta|$ is the Bohr electron magneton, x is angle of the atom with $g_{\parallel}$ and the metal center, A is the Fermi contact hyperfine, and $\tau_e = \tau_s + \tau_m$, equivalent to τ_c and this makes the value of $\delta(\tau_c,\tau_e)=1$. Sternlicht eliminates ω_I and ω_s with consideration that for many paramagnetic complexes, $\tau_c^{-1} > \omega_I$. In the case of Co(II), τ_c^{-1} is expected to be $\sim 200\omega_I$.

Sternlicht's equation, 5.4, is equally applicable to the case of the rotational correlation energy, $h\tau_r^{-1}$, as being larger and smaller than electron ***g***-anisotropy Zeeman energy, $|g_{\parallel}-g_{\perp}||\beta|H_0$. Using a method for spherically-rigid particles, τ_r may be estimated as 1.2×10^{-10} seconds using the following Stokes-Einstein relation:[30]

$$\tau_r = \frac{4\pi\eta a^3}{3kT} = \frac{\eta \mathrm{MW}}{dN_A kT} \qquad \text{Eq. 5.5}$$

Here, η is the solvent viscosity, a is the radius of the molecule, MW is the molecular weight, d is the density, assumed to 1000 kg/m^3, and N_A is Avogadro's number.

The rotational correlation energy has a value of 5.5×10^{-17} erg. With H_0 set to 9864 G, the largest value for these experiments ($\nu(^1H)$=42 MHz), the electron anisotropy has a value of $(8.48-1.02)(9.2740 \times 10^{-21}$ erg $G^{-1})(9864$ G$)=6.8 \times 10^{-16}$ erg. Therefore, the rotational correlation energy is about one order of magnitude smaller than the electron spin anisotropy energy. When $h\tau_r^{-1} << |g_{\|}-g_{\perp}||\beta|H_0$, $T_1=T_2$.

However, another consideration is the relative magnitude of the overall correlation energy and the electron spin anisotropy energy. When the $h\tau_c^{-1}$ is on the order of the electron-spin Zeeman energy, Sternlicht stated that the relaxations expressions are functions of τ_r. Example literature values of τ_c range from 5 ps for hexaaquocobalt(II) to 13 ps for a small tetrathiolate polypeptide,[61, 62] and they yield correlation energies of 1.3×10^{-15} erg and 5.1×10^{-16} erg, respectively. It is therefore likely that the correlation energy of $Co(Tp)_2$ will be on the same order of magnitude as the electron spin anisotropy energy. Sternlicht defers from attempting to treat the case, citing poor NMR resolution, little variation in T_1, and insensitivity to τ_r.

Bertini stated a restrictive concern pertaining to the splitting of the S manifold due to the hyperfine interaction of metal nucleus and the spin moment, A_M.[30] For this effect to have relevance, two conditions are $A_M > h\tau_c^{-1}$ and $A_M > g\mu_B B_0$, where g is $g=1/3(g_{\|}+2g_{\perp})$ and B_0 is the magnetic field. From Q-band EPR, A_M was measured as 1100 MHz. As in the previous paragraph, the expected range of τ_c values, 5-13 ps, gives energies of 53-12 GHz, much larger than A_M. At the high field end of the NMR

experiments, 9864 G, $g\mu_B B_0$ is only 484 MHz. It follows that only one of the two conditions was met.

Even with the above concerns, the error expected in using the Solomon relation Eq. 5.3, for determining τ_c is not more than 10-20%.[30] Thorough treatments for occasions when Solomon-Bloembergen-Morgan (SBM) theory breakdown are possible with Bertini's PARANMRD program[63] and Sharp's PARELAX program.[63, 64] However, comprehensive theories of NMR paramagnetic relaxation enhancements (NMR-PRE) are still developing.[65] For the purpose of this dissertation, Eq. 5.3 will be used and compared with Eq. 5.4. Jesson measured T_2 values for $Co(Tp)_2$ and then followed Eq. 5.4 of Sternlicht with an isotropic τ_c taken from Swift, *et al.* to calculate T_2 values based on the relative populations of spin-orbit states and their respective *g*-values.[8, 61] His values will be compared under the assumption that T_1=T_2.

Longitudinal Relaxation

The T_1 values obtained are compiled in Figure 5.2. They were calculated with the standard equation:[55]

$$M_t = M_0\left(1 - 2e^{-\tau/T_1}\right) \qquad \text{Eq. 5.6}$$

Here, M_t is the detected magnetization and M_0 is the equilibrium magnetization, and τ is the time between the 180 and 90 degree pulses. For these experiments τ was varied between one μsec and $5x10^6$ μsec. Peak heights were measured with respected to the baseline (to account for baseline drift) and then fit directly with Eq. 5.6. An alternative method is to fit the data with $\ln(M_0-M_t)$ vs. τ and the slope will be $1/T_1$.[55] Furthermore, the delay time when no signal observed is approximately equal to $T_1(\ln 2)$. All of these

give similar results. The longest T_1 values observed were no more than 8 msec, thus a sufficient recycle delay time would be 40 msec. Use of a one second recycle delay was therefore excessive (5^3T_1). The curve fits that led to the values shown in Figure 5.2 are compiled in Figures A4.4 and A4.5.

The average relaxation times at 295 K, in msec, are 3-H (0.89) ≤ B-H (1.12) < 5-H (2.33) << 4-H (7.22). These values correspond well, qualitatively, with the magnitude of the dipolar hyperfine interaction, indicating that it is the likely source of NMR-PRE. By using the $|A_{dip}|$ values determine in Chapter 4, Table 4.1, the ratio of $5.5/|A_{dip}|$ is where 5.5 simply scales the values to a 0.89 minimum, the values are B-H (0.89) ≤ 3-H (0.91) < 5-H (2.49) << 4-H (10.37). The trend is remarkably similar. Values measured for T_2 by Jesson are, in msec, 3-H (0.75) ≤ B-H (0.85) < 5-H (1.9) << 4-H (4.5), and again, similarly, differing mostly in the 4-H proton. Jesson measured T_2 values at $\nu(^1H)$=60 MHz. For the range studied herein, there are no observable trends in the data that would obviate an extrapolation to Jesson's values. However, the relative magnitudes are well reproduced.

When the temperature is lowered to 237K, the open marks in Figure 5.2, there is a significant decrease in the observed T_1 values. The 4-H T_1 decreases from 7.2 to 1.3 msec and the 5-H decreases from 2.3 to 0.36 msec, an extremely short T_1. Two possible mechanisms are 1) changes to the populations of component spin states and 2) a change in the molecular rotation. Jesson found that addition of the higher-lying spin states created a 20-30% correction to his calculation of T_2 values. The decrease is greater than that amount. From Eq. 6.5, it is shown that the rotational correlation time is inversely related to temperature. For a change from 295K to 237K, τ_r will increase by a factor of

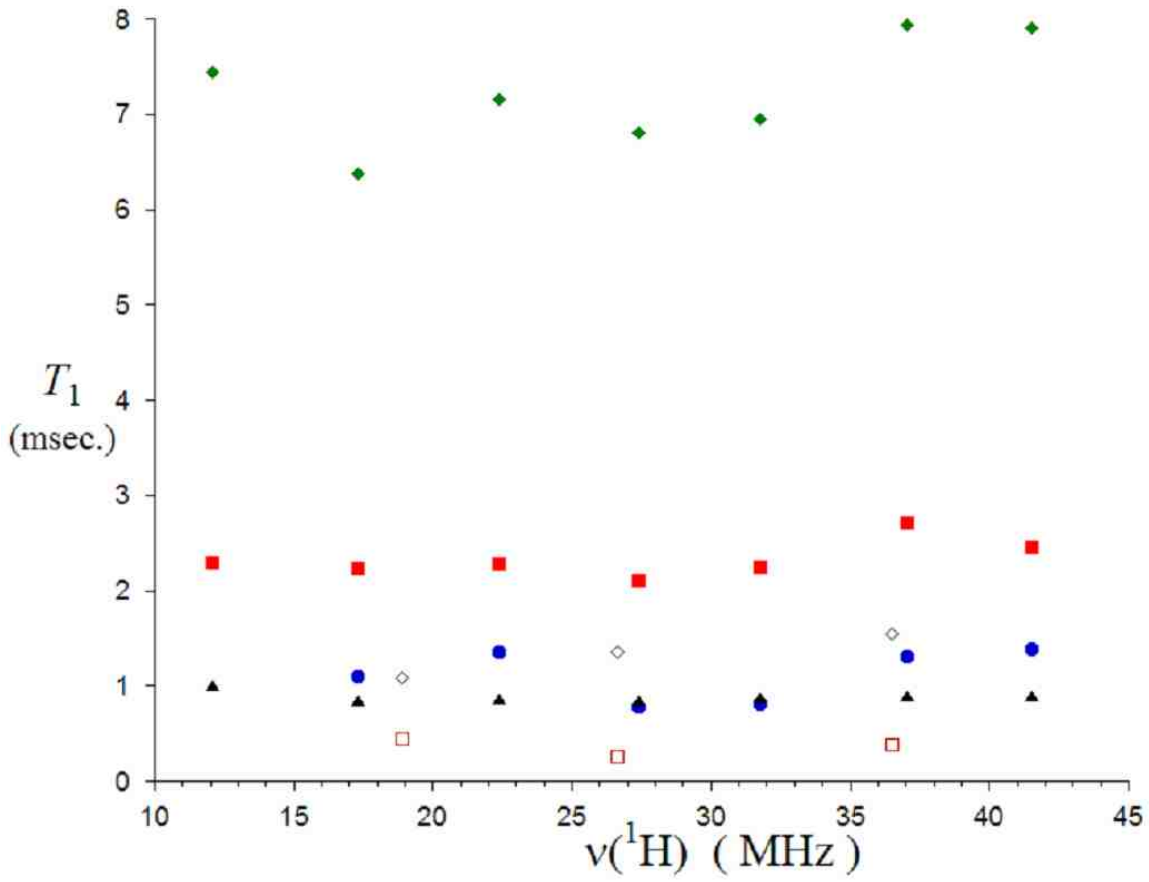

Figure 5.2 Longitudinal (T_1) relaxation times $Co(Tp)_2$ at 295K (solid) and 237K (open). Markings are B-H (blue circle), 5-H (red square), 4-H (green diamond), and 3-H (black triangle).

1.24. Given that T_1 is inversely proportional to τ_r, an increase in τ_r will decrease the value of T_1. This lends evidence to the case laid out by Sternlicht for when τ_c is a function of τ_r.

Correlation time

The correlation times determined from the measured T_1 values, using Eq. 5.3, are shown in Figure 5.3. Values of τ_c were varied until they matched T_1 with an optimal τ_c to three significant figures. Because an isotropic *g*-value is used, with no angle dependence, the different T_1 values all generate distinct values for τ_c. Using average values for τ_c, their order in ps is 3-H (1.5), 4-H (2.4), B-H (8.5), and 5-H (9.3). Due to the isotropic nature of Eq. 5.3, one would expect these to simply follow r^{-6}, but they do not: 3-H (0.16), B-H (0.67), 5-H (1.64), and 4-H (2.0) ($x10^{-56}$ m^6). The dipolar interaction clearly is essential for an accurate calculation of τ_c. Jesson was able to use the first term in Eq. 5.4, with only an estimate of the $Co(Tp)_2$ crystal structure, and obtain a fair match of his data with a single τ_c value of 3.6 ps. With the crystal structure reported in Myers, *et al.*, a more accurate calculation with Eq. 5.4 is possible. Using Jesson's values for the contact hyperfine coupling, a_N, the dipolar term is on the order of $10^{14}\tau_c$, the second term is $10^5\tau_c$ and the third, purely contact term is $10^{12}\tau_c$. Therefore, the first term alone is adequate. When all three terms are used, a value for an isotropic τ_c was found to be 2.34 ps, fit to $1/T_1$ of 3-H. The values for T_1 determined in this way are, in msec, 3-H (0.90), B-H (0.97), 5-H (2.95), and 4-H (5.92), which is a fairly good match of the observed trend. It is important to use an effective spin of $S'=1/2$, as Jesson did. The true S=3/2 results in sub-picosecond values for the isotropic correlation time, which is out of line with literature values. The measurements of 4-H and 5-H at 237K have much larger

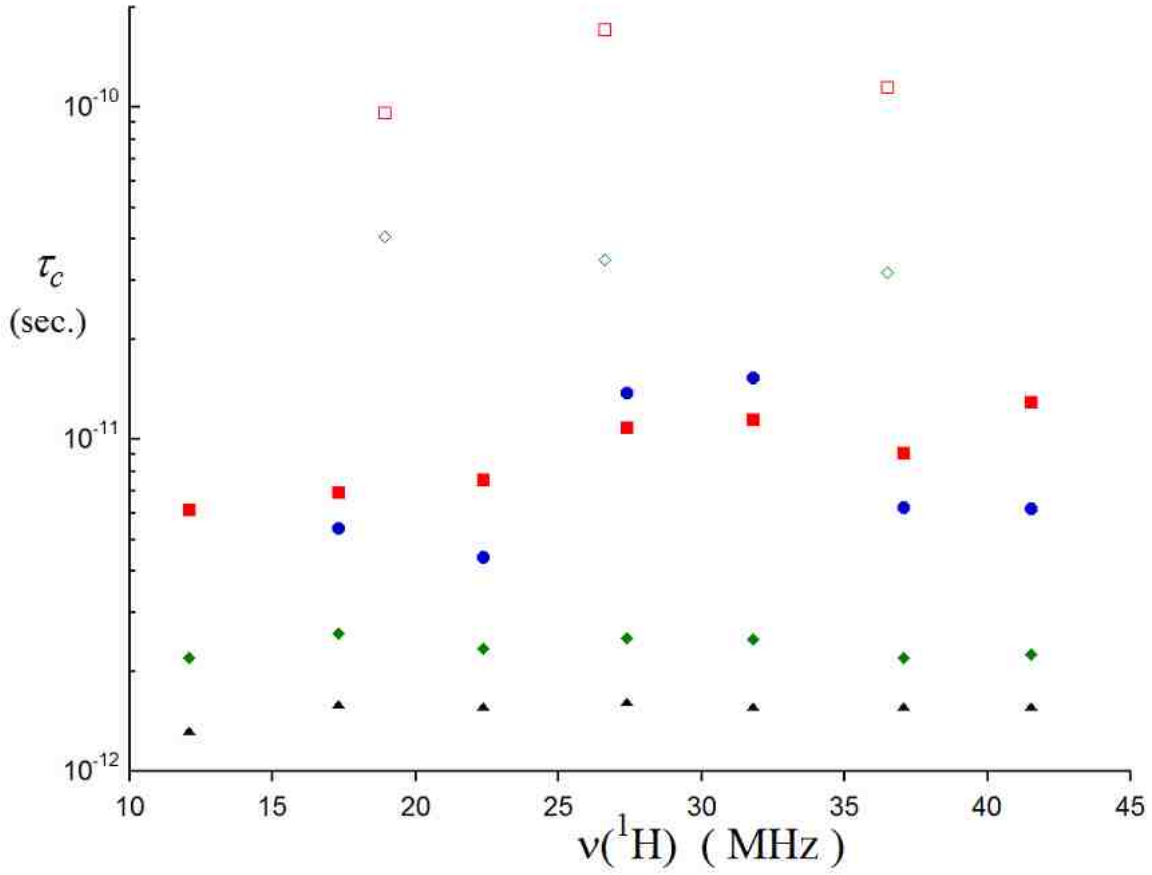

Figure 5.3 Correlation times of $Co(Tp)_2$ at 295K (solid) and 237K (open), determined by using isotropic SBM theory. Markings are B-H (blue circle), 5-H (red square), 4-H (green diamond), and 3-H (black triangle).

correlation times, which are again, inversely proportional to T_1. The change in τ_c, from 295K to 237K, is not the result of a simple linear dependence in temperature.

Conclusion

In conclusion, NMR measurements of the longitudinal relaxation, T_1, of individual protons of $Co(Tp)_2$ were successfully performed in the range of 12 to 42 MHz with an EPR magnet. The values were very similar to those measured at 60 MHz by Jesson for the transverse relaxation, T_2, of the same complex.[8] Calculations of the correlation time showed that the dipolar interactions arising from the highly anisotropic *g*-tensor were the primary factor in the different values of T_1 for each proton. The sizable increase in the correlation time upon decreasing the temperature to 237K from 295K indicates that the solvent viscosity and therefore rotational correlation time may be a factor in the overall relaxation rate. A more accurate τ_r could be determined by measuring T_1 of a diamagnetic complex, *e.g.* $ZnTp_2$, which would be purely a function of τ_r. In the 1D NMR spectra, line widths change by a factor of approximately two between 31 and 37 MHz, indicating that there may be a problem with a preamp module. Without measurements at more frequencies there is no clear shift in T_1. Future data analysis could explore the possibility of using Bertini's and Sharp's computer programs,[63, 64] which will likely provide a more complete treatment of the parameter space involved in the analysis of these experiments.

Chapter 5

Summary and Future Work

Zinc is an important metal, present at approximately three grams in the human body and involved in structural roles as well as catalytic roles in several hundred enzymes across classes of oxidoreductases, transferases, hydrolases, lyases, isomerases and ligases.[4] Cobalt(II) is used as a substitute of Zn(II) in metalloenzymes due to the retention of catalytic activity and similar binding affinities. Previous literature of Co(II)-substituted Zn(II) metalloenzymes has emphasized the methods of optical spectroscopy with a limited number of EPR and NMR studies that are largely qualitative in nature.[2] Paramagnetic resonance studies of model compounds are a means of developing an understanding of the ground state of high spin Co(II), which may be complicated by low-lying excited states, orbital degeneracy, unquenched orbital angular momentum, and large *g*-value anisotropy. The *bis*trispyrazolylborate cobalt(II) and related derivatives offer an opportunity to study these properties with six imidazole-like pyrazole rings that are equivalent by symmetry. Imidazole is a common ligand in Zn(II) metalloenzymes.[4] Proton positions on the pyrazole rings can be substituted to allow identification of signals and study the propagation of spin density throughout the ring structure. For all these reasons, in addition to the ease of synthesis, *bis*trispyrazolylborate compounds of Co(II) are well suited as model complexes with which to assess the properties of high spin Co(II).

In Chapter 1, it was shown that the earliest theoretical treatment was largely successful in describing the observed EPR spectra for the series of compounds studied. Other approaches than that of Chapter 1 is seen in the simulations discussed in Chapter 2.

Specifically, the use of a set of greal values and in some cases the rhombicity parameter *E* may be successfully applied in a simulation of the experimental spectra. It was confirmed that EPR simulations at a single frequency will not provide a unique set of parameter values to describe an EPR spectrum. Chapter 3 documents the development of an instrumental interface for an ENDOR instrument. Although it is of low sensitivity, ENDOR is one of the most direct methods of determining hyperfine couplings. ENDOR was used in Chapter 4 to probe the hyperfine structure of $Co(Tp)_2$ at both 34 GHz and 9.4 GHz, covering the full range of *g*-values of $Co(Tp)_2$. Signals of from three nuclei, ^{1}H, ^{14}N and ^{11}B were observed. The ^{14}N ENDOR provided narrow line widths at $g_{||}$, however due to the significant broadening of the feature it was not possible to distinguish between application of either the simple theory of an isotropic Fermi interaction[41] or the case of an anisotropic Fermi contact interaction.[10] The ^{1}H ENDOR data could not be reconciled with the values of A_{iso} determined previously from NMR,[5] by way of a single value for the fraction of spin density located on the Co(II) nucleus. In Chapter 5, the novel idea of using EPR magnets for performing modern FT NMR measurements of paramagnetic solutions was tested. It was found that the line widths were large at the low and high ends of the frequency range tested, however the paramagnetic shifts were preserved. For simple paramagnetic substances of few unique nuclei and large paramagnetic shifts the technique will be applicable. For $Co(Tp)_2$, it was found that the T_1 values were mostly constant (within the noise of the data) across the range studied, as expected.[30] The significant variation in the magnitude of T_1 for the different protons was ascribed to the effect of *g*-value anisotropy.

There are more experiments that could be performed with the *bis*trispyrazolylborate compounds. An experimental determination of the separation of spin orbit energy levels with temperature-dependent Far-IR spectroscopy would be useful. A comprehensive set of ^{13}C NMR measurements for the series of compounds will help any attempt to determine contributions of π spin density on the pyrazole to the observed NMR shifts. Furthermore, application of the multi-state approach of McGarvey[9] remains as the most appropriate for quantifying the observed NMR shifts in the *bis*trispyrazolylborate Co(II) compounds. Pulse ENDOR measurements could be applied as additional evidence of the assignment of the ^{14}N ENDOR as originating simply from the $A/2+\nu^+$ peak or if it is in fact both the ν^+ and ν^- signals as well as observe both the ν^+ and ν^- proton signals. More advanced techniques, such as hyperfine-selective ENDOR could be applied to help differentiate nitrogen and proton signals. In terms of instrumentation at UNM, development of a reliably ENDOR instrument remains as an objective. Some of the features of the ENDOR instrument outlined in Appendix II could prove beneficial to subsequent researchers. The low sensitivity and hardware-inducing line broadening of NMR acquired on EPR magnets may be limiting, but much work remains in characterizing the use of EPR magnets for NMR. In an era of scarce world-wide helium sources, iron core magnets will likely receive greater attention. Iron core magnets also have the advantage of the capability of tuning to a variety of field strength, a feature unavailable with superconducting magnets.

Appendix I

MATLAB Scripts

MATLAB Scripts, Figure 1.3, p.11

```
disp('calculation of S.O. energies from JESSON equations')
disp('=============================================')
a=1.434;
aprime=1.379;
lambda=-146.7;
format short eng;
%%
for x = -5000:100:5000;
A=[(3/2)*a*lambda -sqrt(3/2)*aprime*lambda 0; -sqrt(3/2)*aprime*lambda
x -sqrt(2)*aprime*lambda; 0 -sqrt(2)*aprime*lambda (1/2)*a*lambda];
[V,D]=eig(A);
m=D(1,1);
n=D(2,2);
o=D(3,3);
B=[x -sqrt(1.5)*aprime*lambda; -sqrt(3/2)*aprime*lambda -
(1/2)*a*lambda];
[V,D]=eig(B);
d=D(1,1);
e=D(2,2);
c=-1.5*a*lambda;
disp([x m n o d e c]);
end
%%
disp('======================JESSON=========================')
```

MATLAB Scripts, Figure 1.4, p.13

```
disp('calculation of g-values from JESSON equations')
disp('=============================================')
a=1.434;
aprime=1.379;
lambda=-146;
p=0;
format short eng;
%%
for x = -8000:100:5000;
A=[(3/2)*a*lambda -sqrt(3/2)*aprime*lambda 0; -sqrt(3/2)*aprime*lambda
x -sqrt(2)*aprime*lambda; 0 -sqrt(2)*aprime*lambda (1/2)*a*lambda];
[V,D]=eig(A);
m=V(1,1);
n=V(2,1);
o=V(3,1);
gpara=(6*m^2+2*n^2-2*o^2)+2*a*(m^2-o^2);
gperp=(4*n^2+4*sqrt(3)*m*o)-sqrt(8)*aprime*n*o;
p=p+1;
disp([p x gpara gperp]);
end
%%
disp('======================JESSON=========================')
```

Appendix II

ENDOR Instrumentation

Abragam and Bleaney describe ENDOR as "stirring" of nuclear transitions in the presence of the specific EPR transitions.[66] Notable in this description is the ambiguity of the process. There have been several different approaches to achieving ENDOR. However, given the small number of instruments that are regularly used to acquire ENDOR of metalloproteins, it is opportune to describe the salient features of one such instrument.

The ENDOR experiment measures an exceedingly small change in the EPR signal intensity, and indeed, it is commonly derided as being of "low sensitivity". Through several decades of development, the Scholes instrument, seen in Figure A2.1 is remarkable in its reliability. Central to CW ENDOR is the reduction of spurious signals. A robust method of doing this is assiduous grounding of all components to a central point. Another consideration of ENDOR design is that signal optimization depends on a complex balance of relaxation times. Nuclear relaxation times are long with respect to the experiment. The Scholes instrument thus pulses the RF with high power (only 11dB attenuation from a 1V amplifier input) but a 0.1 msec on per one msec cycle, yielding a low overall output power of the RF –typically less than 15W. This decreases coil heating and the boiling rate of the cryogen. The low overall power allows the simple grounding of the RF coil to the ESR resonator, as opposed to terminating in an external RF load.

Of special note is the Sienkiewicz ENDOR resonator. It provides a quality factor typically in the range of 1200 to 3000, tolerating a wider variety of solvent dielectric values and larger sample volumes, relative to the Bruker ER 5106 QT cavity. A hole

passing through the length of the cavity allows for the optimal vertical positioning of a sample in the cavity space. This vital design feature accommodates samples in low melting point solvents that may crack and form gas pockets in the sample insertion process.

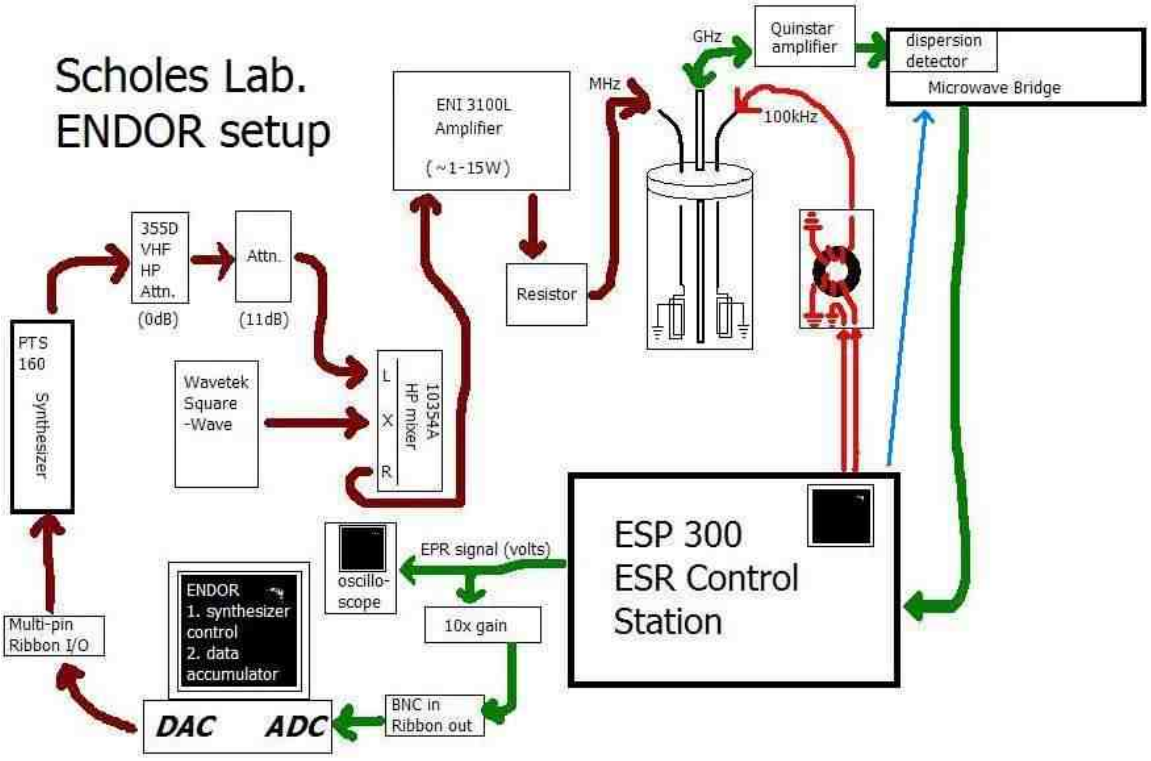

Figure A2.1 Schematic of Charles Scholes's ENDOR instrument. The square-wave that is used to pulse the RF is typically set to a 10% duty cycle, 100 μs on / 900 μs off. Both the modulation and RF coils terminate to ground on the ENDOR cavity.

APPENDIX III

Supplemental ENDOR Figures

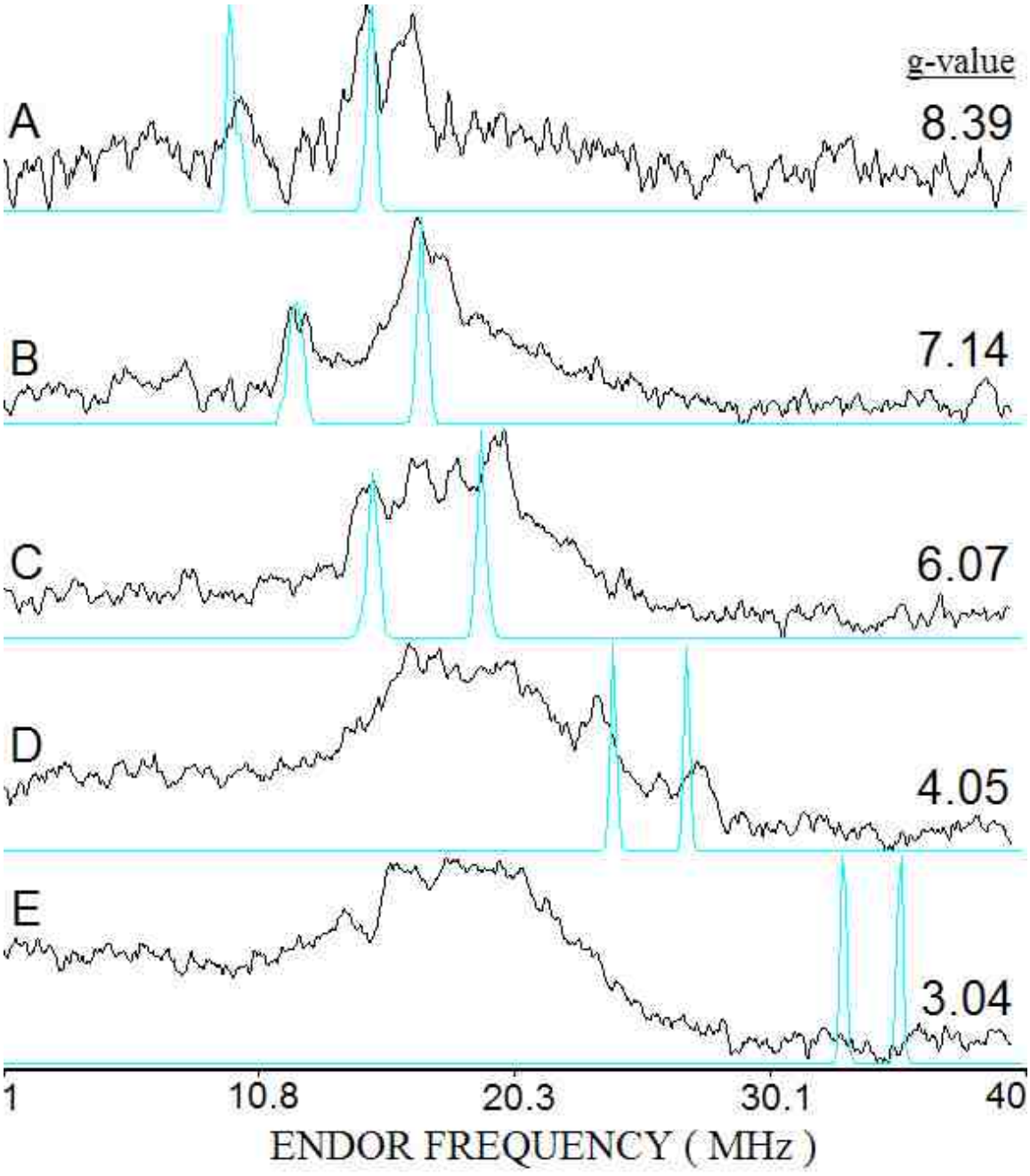

Figure A3.1 The ^{1}H ENDOR signals through the ^{14}N region of Co(Tp^{3Me})$_2$. The ν(^{1}H) is demonstrated with an arbitrary GENDOR v2.3 simulation A=[5.75,1,1]; all other values are default (g-values=g_{eff}).

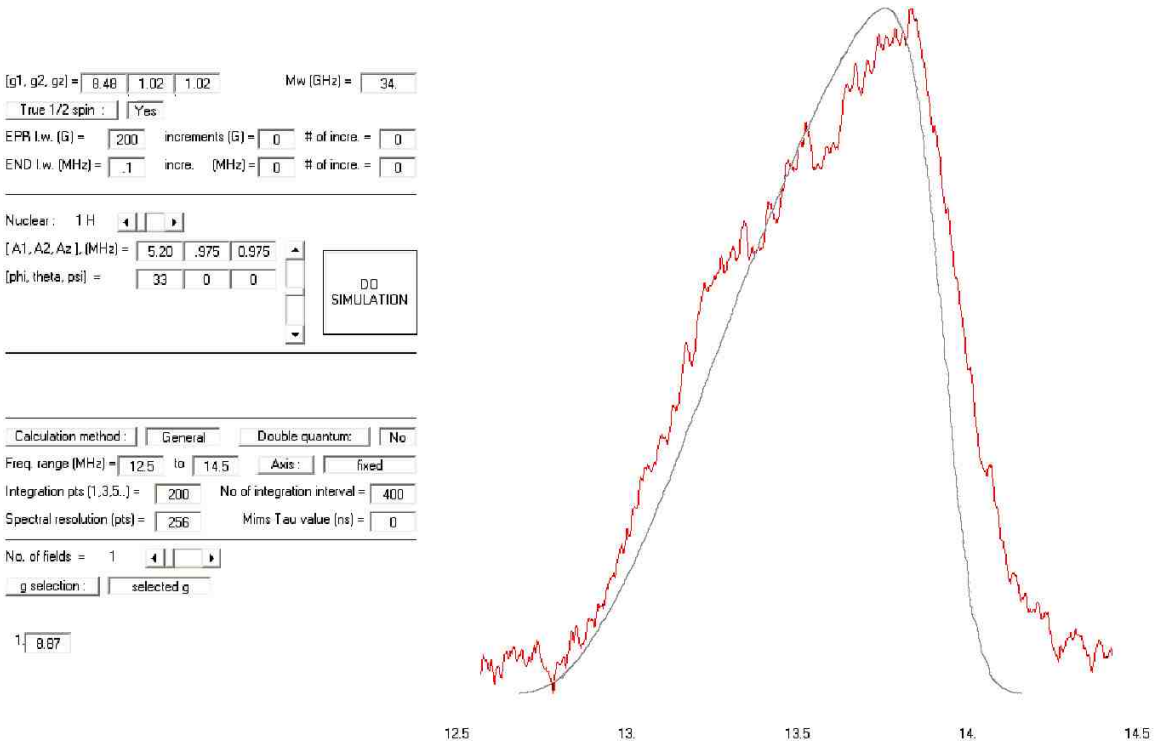

Figure A3.2 GENDOR v2.3 simulation of 5-H of $Co(Tp)_2$. Data is in red and simulations are in gray. Data was collected at 2740G, 4000 scans, sum of low to high and high to low sweep directions, sweep rate: 2 MHz/sec.

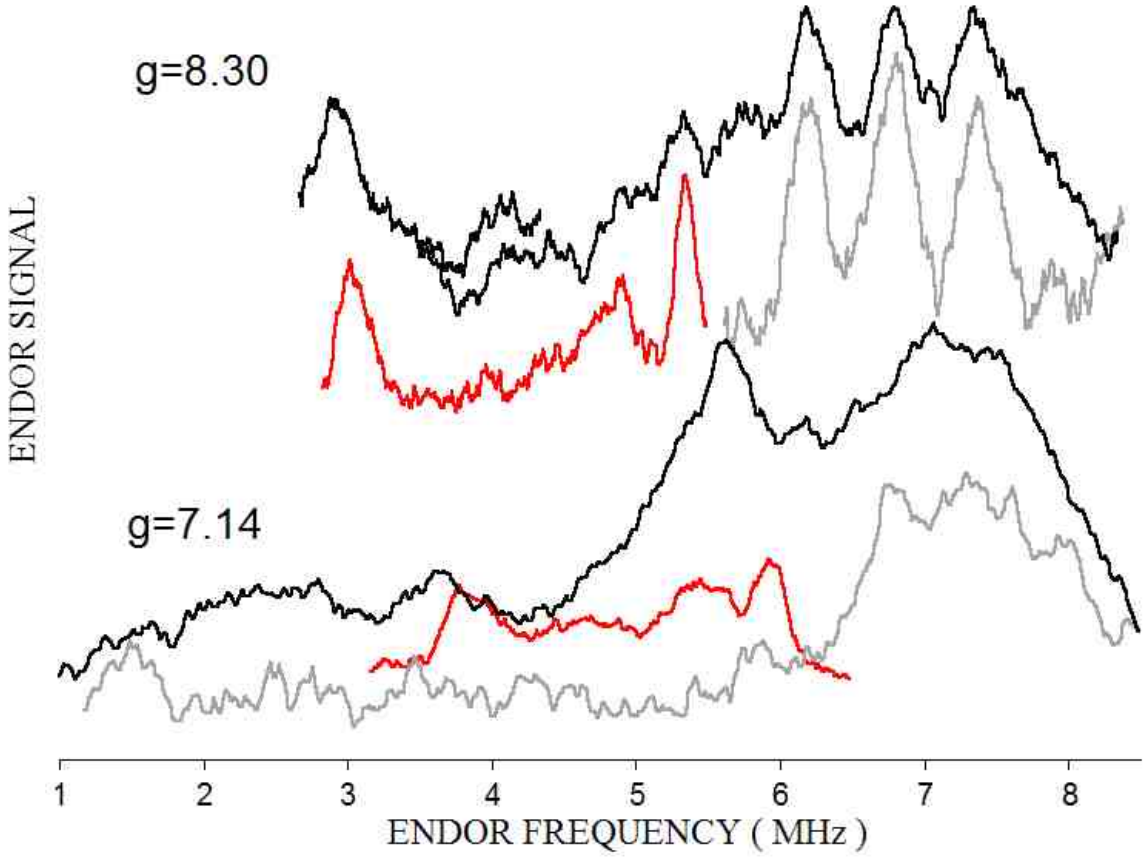

Figure A3.3 The 3rd harmonic of protons is shown in red, calculated from actual proton spectra acquired about $\nu(^1H)$. The grey signals represent a 3dB decrease in the RF power from the black traces. Close alignment of the ca. 2.5-6 MHz features in the black, and their absence in the grey suggests that the three-line spectrum is not due to a 3rd harmonic feature.

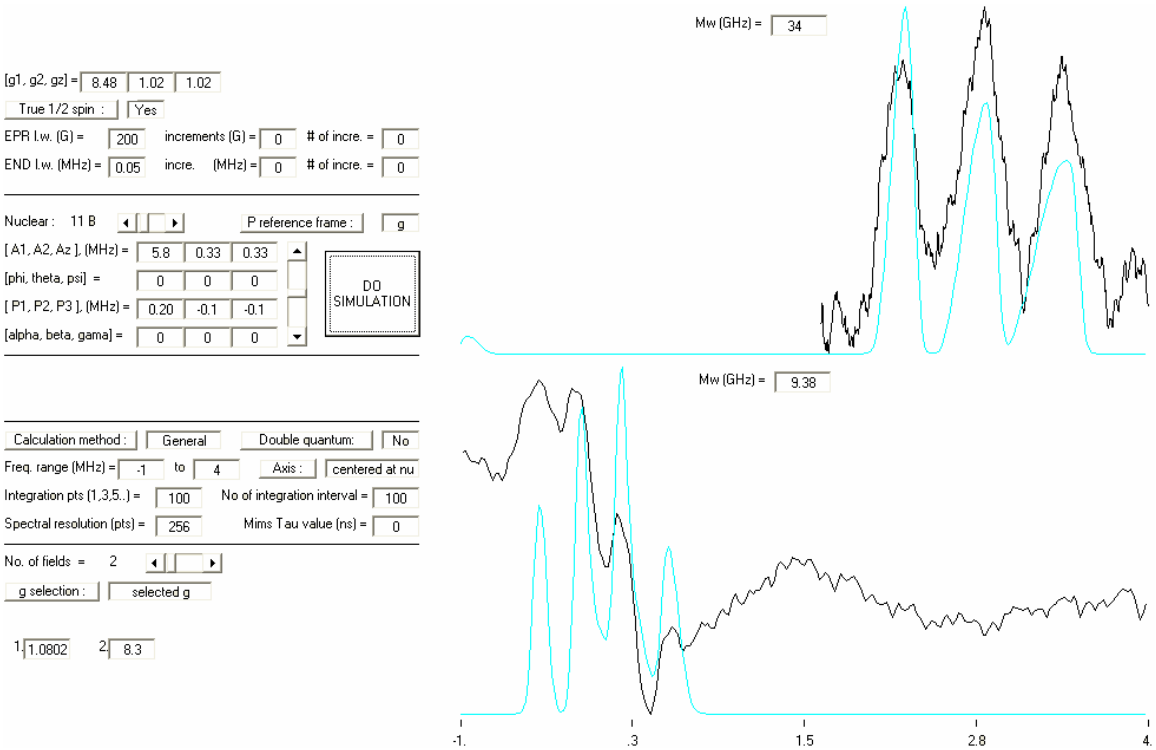

Figure A3.4 Q-band and X-band ^{11}B ENDOR signals (black), with GENDOR v2.3 simulations (blue), g=[8.48,1.02,1.02], A=[5.8,0.33,0.33], and P=[0.2,-0.1,-0.1]. All other values set to default. The X-band data was acquired as the first derivative.

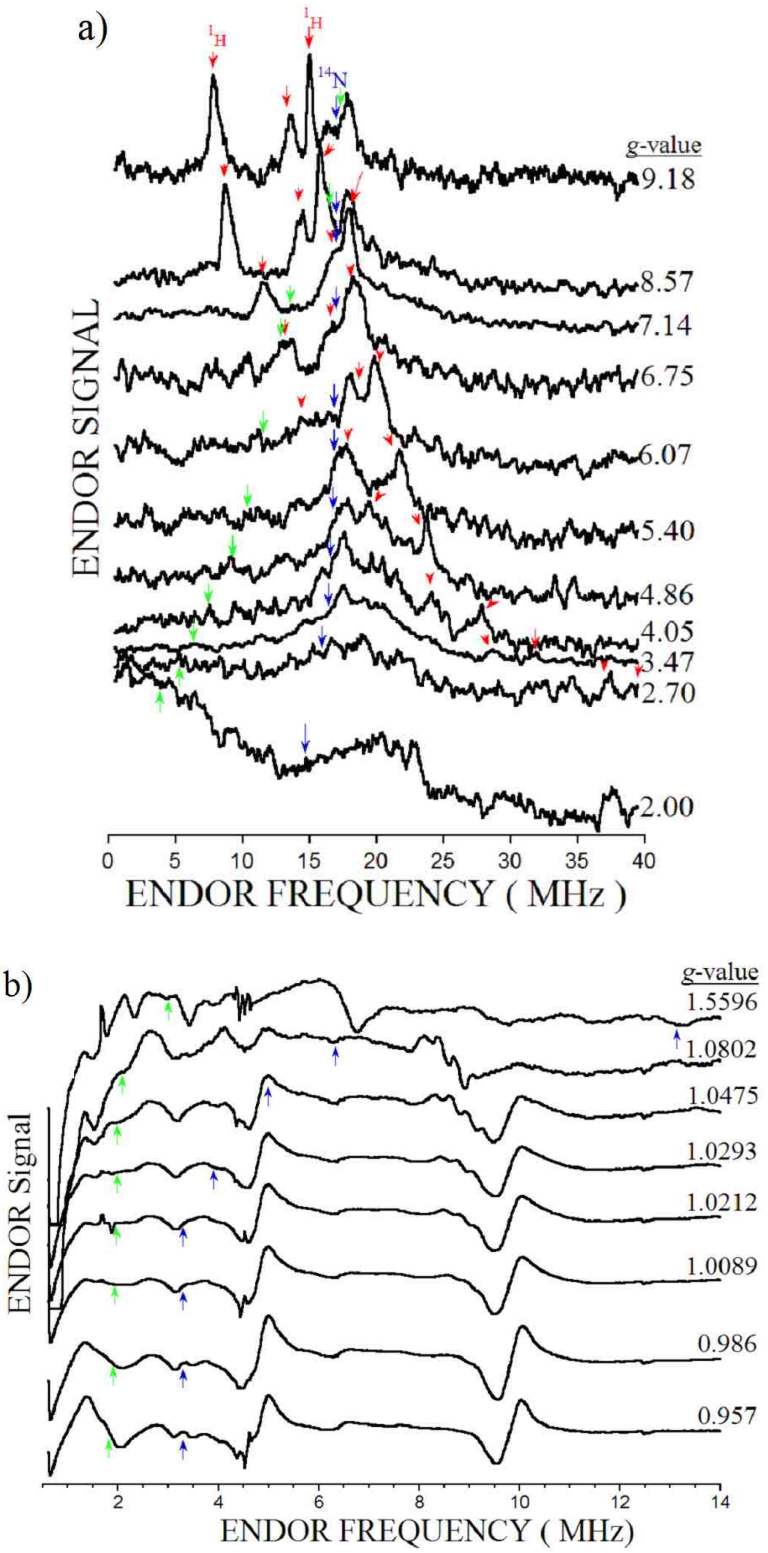

Figure A3.5 Predicted $(A_{Fermi})/2$ ^{14}N peak locations by Eq. 4.6 with A_{int}=11.8 MHz (blue), and according to $A_{obs}/2=g_{eff}A_{int}/(2g_e)$ with A_{int}=7.68 (green); a) Q-band and b) X-band.

a)

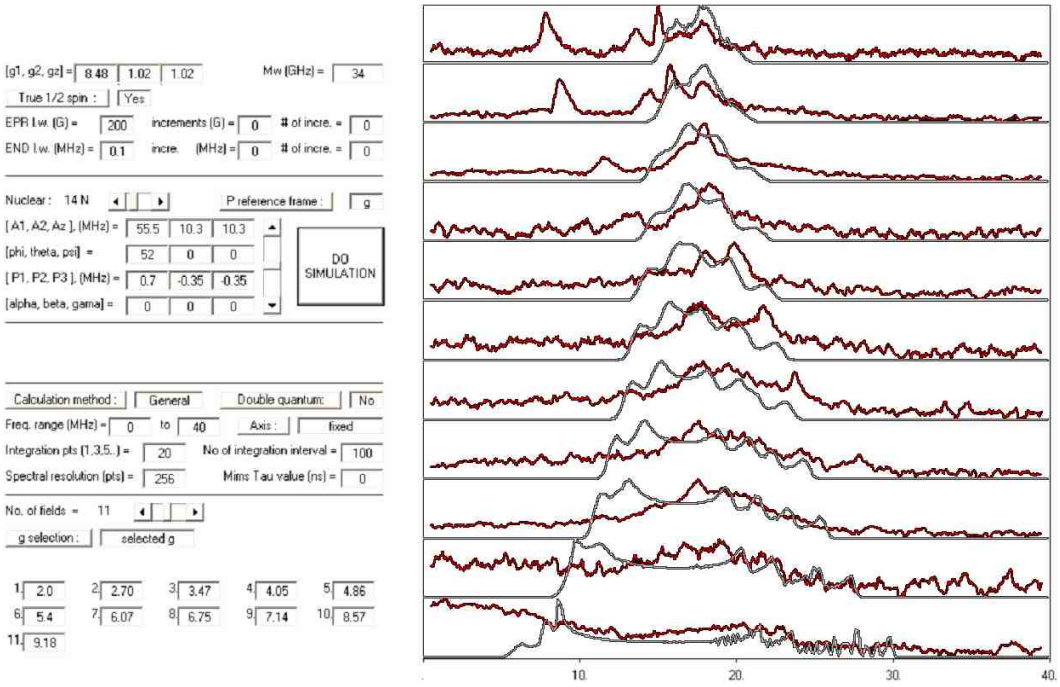

b)

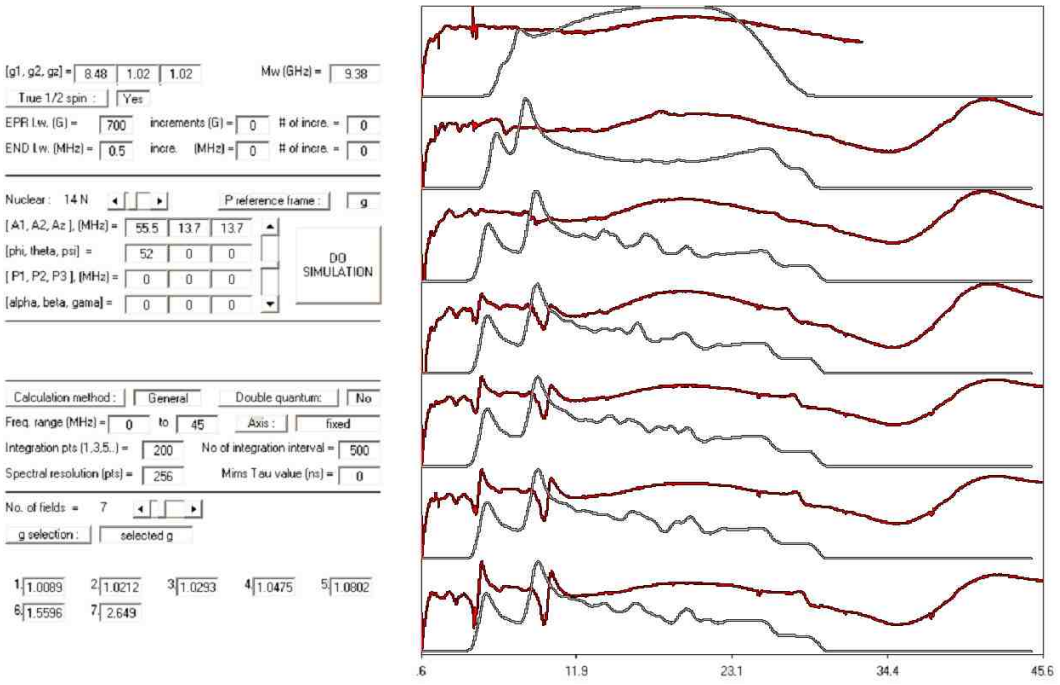

Figure A3.6 Angle-selected GENDOR v2.3 simulations of coordinating ^{14}N at a) Q-band and b) X-band. Data is in red and simulations are in white. The X-band data was collected as a derivative.

a)

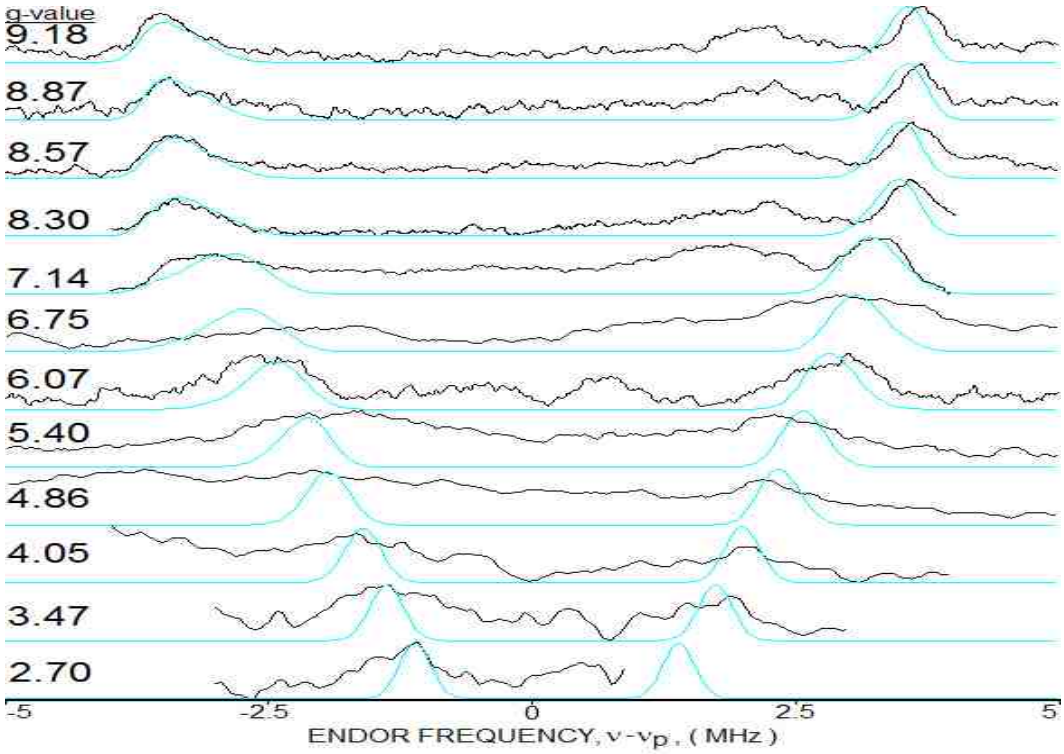

b)

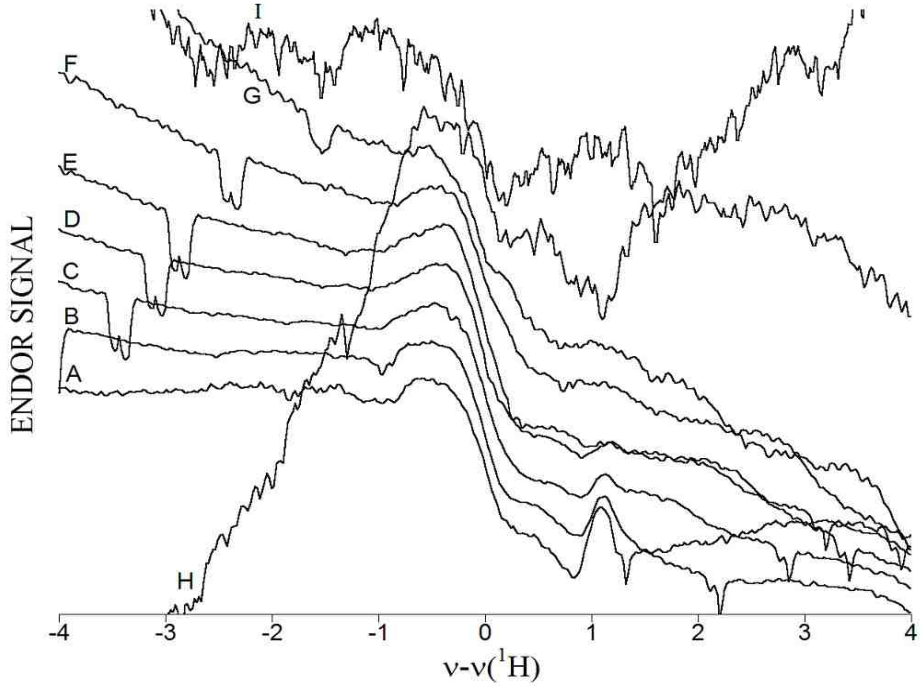

Figure A3.7 The ^{1}H region of a) Q-band and b) X-Band ENDOR spectra. A) *g*=0.957; B) *g*=0.986; C) *g*=1.009; D) *g*=1.021; E) g=1.029; F) *g*=1.048; G) *g*=1.080; H) *g*=1.560; I) *g*=2.649. The blue Q-band simulation is from GENDOR, A(7.4,1,1). Sample concentration effects broadened the ^{1}H ENDOR line widths.

APPENDIX IV

Supplemental HF NMR Figures

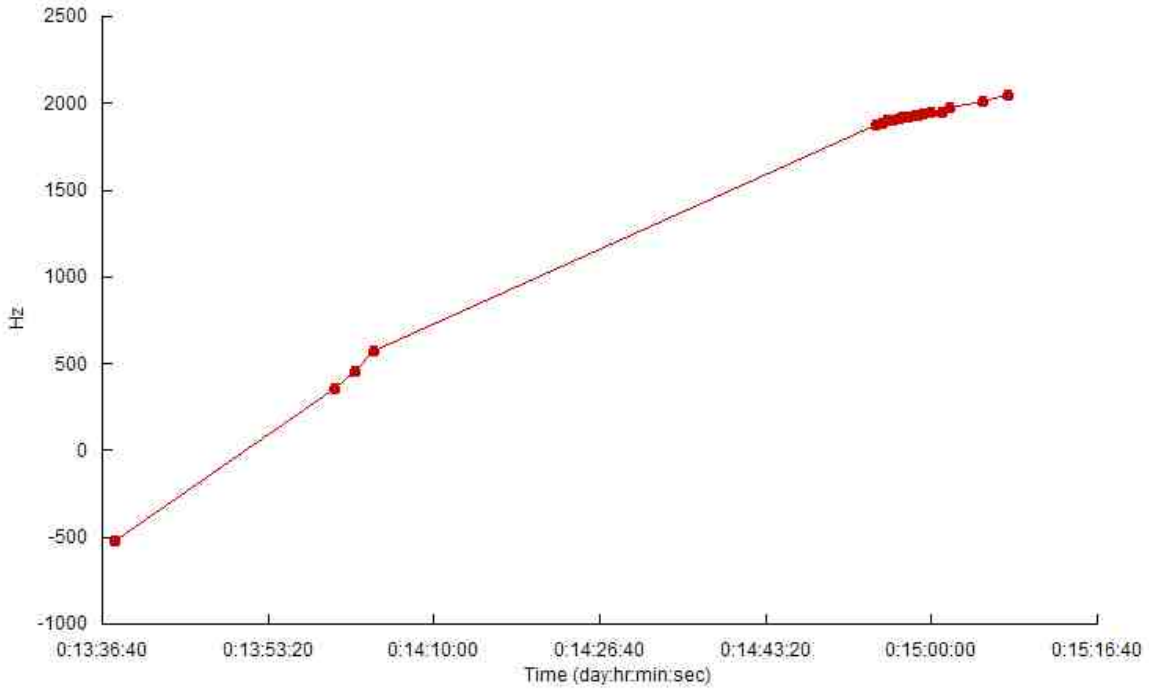

Figure A4.1 Resonance position change as a function of time for 1mM hexaaquochromium(III) in protonated water in a custom built NMR probe tuned to 30.07 MHz. Number of scans = 1. After three hours, little change occurs.

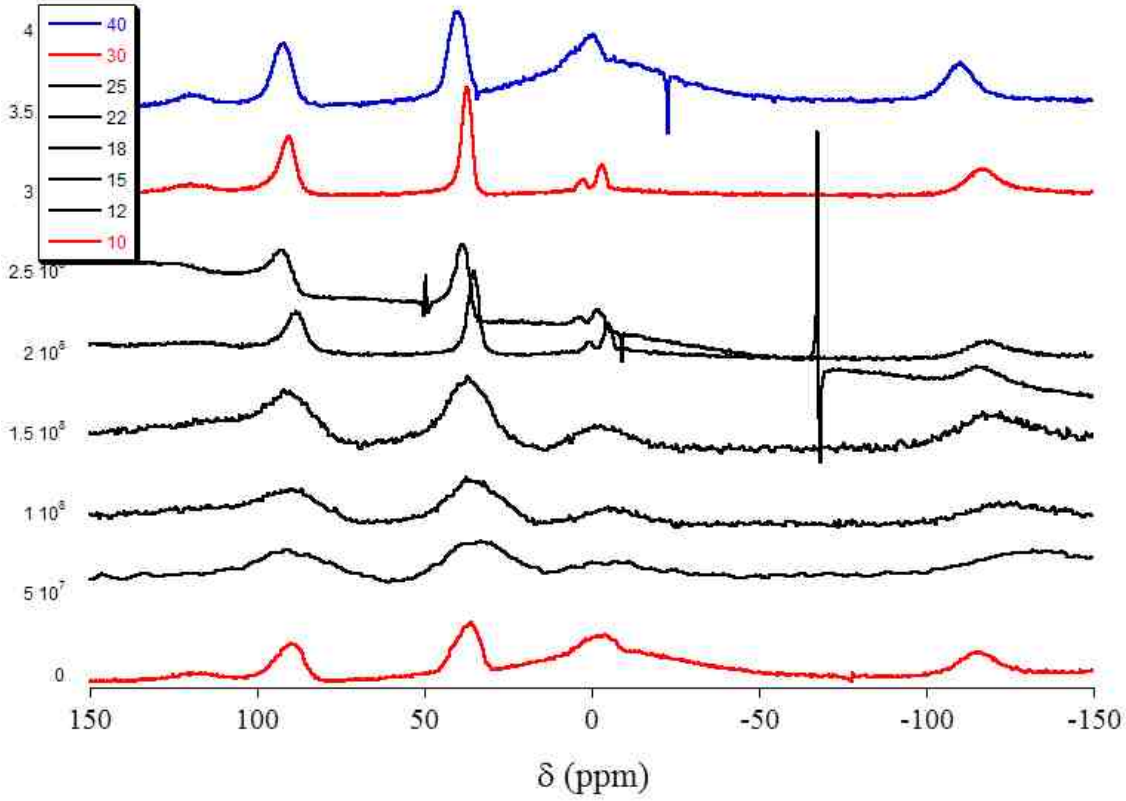

Figure A4.2 NMR data acquired by D. Tierney, using a series of custom probes constructed by the author. 20mM $Co(Tp)_2$ in d8-toluene. The resonant frequency, $\nu(^1H)$, is given in the inset box. The line widths for 12-18 is from field inhomogeneity caused by a magnetic capacitor.

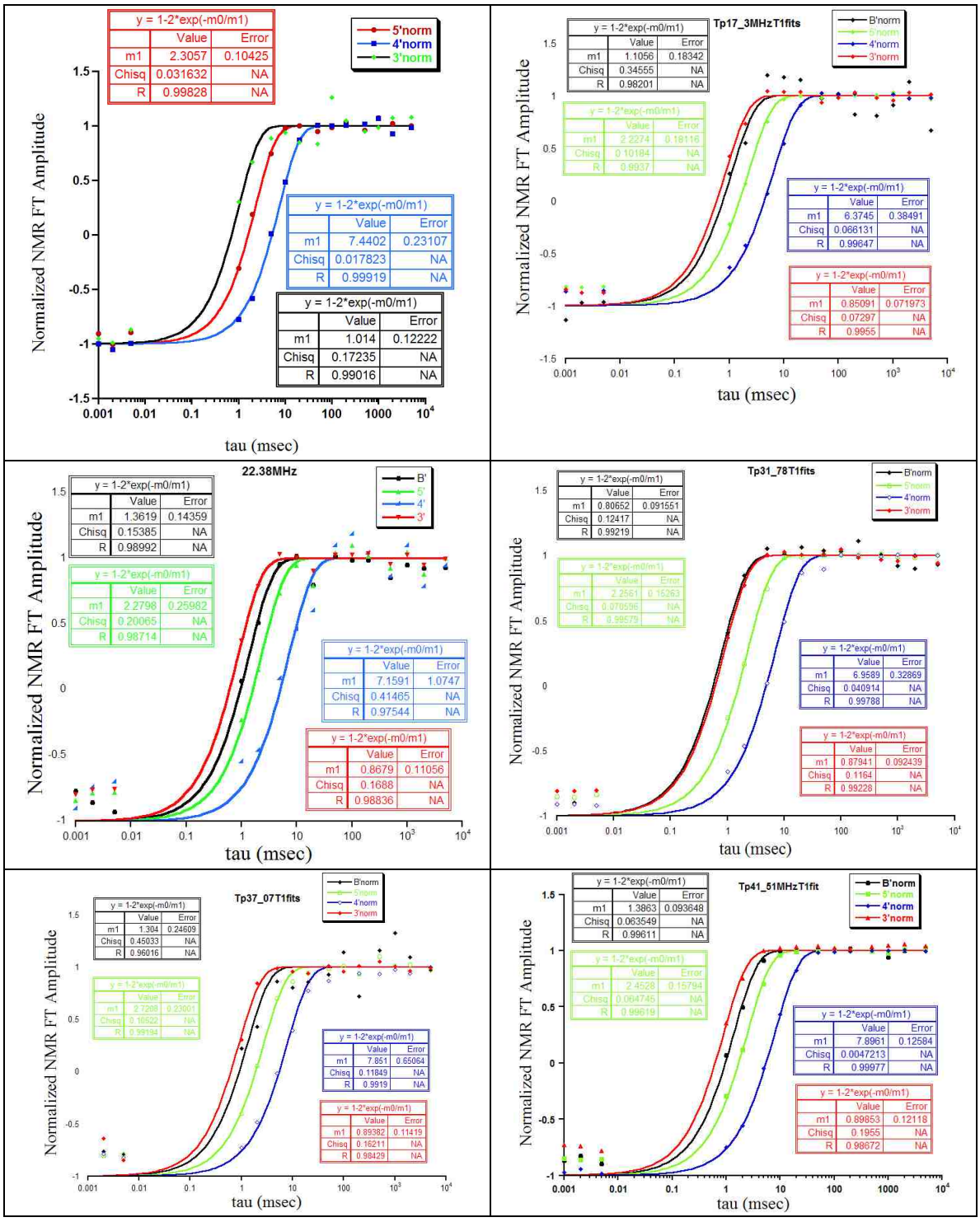

Figure A4.3 Longitudinal relaxation, T_1, fits to peak intensities at 295K.

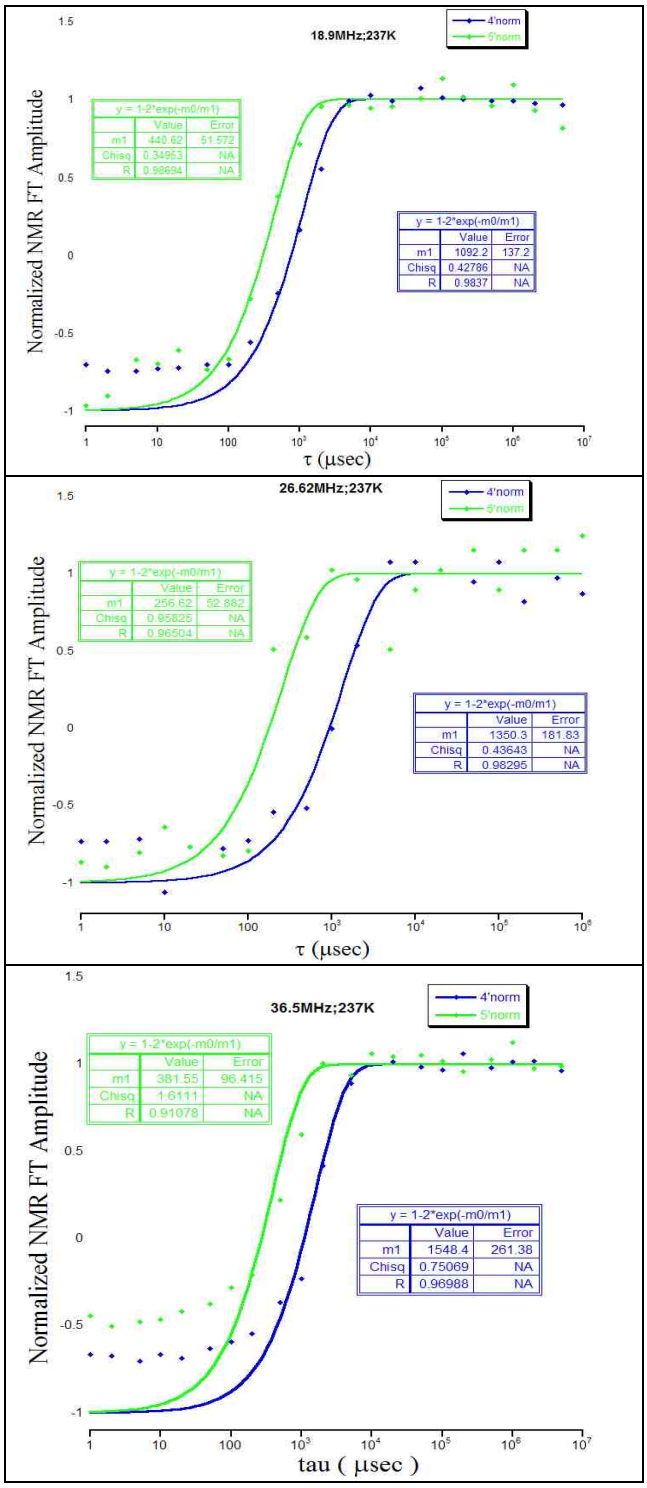

Figure A4.4 Longitudinal relaxation, T_1, fits to peak intensities at 237K.

References

1. Kanan, M. W., Nocera, D. G., In Situ Formation of an Oxygen-Evolving Catalyst in Neutral Water Containing Phosphate and Co2+. *Science* **2008,** 321, (5892), 1072-1075.
2. Maret, W., Vallee, B. L. , Cobalt as Probe and Label of Proteins. *Methods Enzymol.* **1993,** 226C, 52–71.
3. Trofimenko, S., *Scorpionates: The Coordination Chemistry of Polypyrazolylborate Ligands*. Imperial College Press: London, 1999.
4. Parkin, G., Synthetic Analogues Relevant to the Structure and Function of Zinc Enzymes. *Chem. Rev.* **2004,** 104, 699-767.
5. Myers, W. K., Duesler, E. N., Tierney, D. L., Integrated Paramagnetic Resonance of High-Spin Co(II) in Axial Symmetry: Chemical Separation of Dipolar and Contact Electron-Nuclear Couplings. *Inorganic Chemistry* **2008,** 47, (15), 6701-6710.
6. Jesson, J. P., Optical and Paramagnetic Resonance Spectra of Some Trigonal Co(II) Chelates. *J. Chem. Phys.* **1966,** 45, 1049–1056.
7. Jesson, J. P., Theory of Isotropic Nuclear Resonance Shifts in Octahedral Co2+ Systems. *J. Chem. Phys.* **1967,** 47, (2), 579–581.
8. Jesson, J. P., Isotropic Nuclear Resonance Shifts in Some Trigonal Co(II) and Ni(II) Chelate Systems. *The Journal of Chemical Physics* **1967,** 47, (2), 582-591.
9. McGarvey, B. R., Theory of the Isotropic NMR Shifts in Trigonal Cobalt(II) Complexes. *J. Chem. Phys.* **1970,** 53, (1), 86–91.
10. Abragam, A., Pryce, M. H. L., The theory of paramagnetic resonance in hydrated cobalt salts. *Proc. Roy. Acad. Sci., A* **1951,** 206, (173-190).
11. Thornley, J. H. M., Windsor, C. G., Owen, J., Concerning the magnetic properties of covalent octahedral cobalt complexes. *Proc. Roy Soc. (London)* **1965,** 284, 252–271.
12. Ballhausen, C. J., *Introduction to Ligand Field Theory*. McGraw-Hill Book Company: New York, 1962.
13. Ballhausen, C. J., *Molecular Electronic Structures of Transition Metal Complexes*. McGraw Hill, Inc.: London, 1979.
14. Griffith, J. S., *The Theory of Transition-Metal Ions*. Cambridge University Press: London, 1961.
15. Ostrovsky, S. M., Falk, K., Pelikan, J., Brown, D. A., Tomkowicz, Z., Haase, W., Orbital Angular Momentum Contributions to the Magneto-Optical Behavior of Binuclear Cobalt(II) Complex. *Inorganic Chemistry* **2006,** 45, 688-694.
16. Fink, K., Wang, C., Staemmler, V., Superexchange and Spin-Orbit Coupling in Chlorine-Bridged Binuclear Cobalt(II) Complexes. *Inorganic Chemistry* **1999,** 38, 3847-3856.
17. Abragam, A., Pryce, M. H. L., Theory of the nuclear hyperfine structure of paramagnetic resonance spectra in crystals. *Proceedings of the Royal Society (London)* **1951,** A206, 135-153.
18. Drago, R., *Physical Methods for Chemists*. Surfside Scientific Publishers: Gainesville, FL, 2002.
19. van Kooten, J. J., Sieverts, E. G., Ammerlaan, C. A. J., Electron-nuclear double resonance of interstitial positively charged iron in silicon. *Physical Review B* **1988,** 37, (15), 8949-8957.

20. G. L. Miessler, D. A. T., *Inorganic Chemistry*. Prentice Hall: Upper Saddle River, New Jersey, 1991.
21. Makinen, M. W. K., L. C.; Yim, M. B.; Wells, G. B.; Fukuyama, J. M.; Kim, J. E., *J. Am. Chem. Soc.* **1985,** 107, 5245–5255.
22. Hanson, G. R., Gates, K. E., Noble, C. J., Griffin, M., Mitchell, A., Benson, S., XSophe-Sophe-XeprView. A computer simulation software suite (v. 1.1.3) for the analysis of continuous wave EPR spectra. *Journal of Inorganic Biochemistry* **2004,** 98, 903-916.
23. Bennett, B., EPR of Cobalt-Substituted Zinc Enzymes. *unpublished*.
24. Hagen, W. R., EPR Spectroscopy of Iron Sulfur Proteins. *Adv. Inorg. Chem.* **1982,** 38, 165-222.
25. Pilbrow, J. R., Effective g Values for S=3/2 and S=5/2. *J. Magn. Reson.* **1978,** 31, 479-489.
26. Larrabee, J. A., Alessi, C. M., Asiedu, E. T., Cook, J. O., Hoerning, K. R., Klingler, L. J., Okin, G. S., Santee, S. G., Volkert, T. L., Magnetic Circular Dichroism Spectroscopy as a Probe of Geometric and Electronic Structure of Cobalt(II)-Substituted Proteins: Ground-State Zero-Field Splitting as a Coordination Number Indicator. *J. Am. Chem. Soc.* **1997,** 119, 4182–4196.
27. Ugulava, N. B., Gibney, B. R., Jarrett, J. T., Iron-Sulfur Cluster Interconversions in Biotin Synthase: Dissociation and Reassociation of Iron during Conversion of [2Fe-2S] to [4Fe-4S] Clusters. *Biochemistry* **2000,** 39, 5206-5214.
28. Bennett, B., EPR of Cobalt-Substituted Zinc Enzymes. **unpublished**.
29. Bennett, B., Personal Communication. In 2005.
30. Bertini, I., Luchinat, C., Parigi, G., *Solution NMR of Paramagnetic Molecules; Applications to Metallobiomolecules and Models*. Elsevier: Amsterdam, 2001.
31. Breece, R. M., Costello, A., Bennett, B., Sigdel, T. K., Matthews, M. L., Tierney, D. L., Crowder, M. W., A Five-coordinate Metal Center in Co(II)-substituted VanX. *J. Biol. Chem.* **2005,** 280, 11074-11081.
32. Krzysztof P. B., M., A., Swierczek, S. I., Ringe, D., Petsko, G. A., Bennett, B., Holz, R. C., Kinetic, Spectroscopic, and X-Ray Crystallographic Characterization of the Functional E151H Aminopeptidase from Aeromonas proteolytica. *Biochemistry* **2005,** 44, 12030-12040.
33. McGregor, W. C., Swierczek, S. I., Bennett, S., Holz, R. C., argE-Encoded N-Acetyl-L-Ornithine Deacetylase from Escherichia coli Contains a Dinuclear Metalloactive Site. *J. Am. Chem. Soc.* **2005,** 127, 14100-14107.
34. Mabbs, F. E., Collison, D., *Electron Paramagnetic Resonance of d Transition Metal Compounds*. Elsevier: Amsterdam, 1992.
35. Jacobsen, F. E.; Breece, R. M.; Myers, W. K.; Tierney, D. L.; Cohen, S. M., Model Complexes of Cobalt-Substituted Matrix Metalloproteinases: Tools for Inhibitor Design. *Inorganic Chemistry* **2006,** 45, (18), 7306-7315.
36. Puerta, D. T., Lewis, J. A., Cohen, S. M.,, *J. Am. Chem. Soc.* **2004,** 126, 8388-8389.
37. Breece, R. M., Jacobsen, F. E., Myers, W. K., Cohen, S.M., Tierney, D. L. In *Model Complexes of Cobalt-substituted Matrix Metalloproteinases.*, Rocky Mountain Conference for Analytical Chemistry: EPR Symposium, Breckenridge, CO, July 27, 2008; Breckenridge, CO, 2008.

38. Krzystek, J., Zvyagin, S. A., Ozarowski, A., Fiedler, A. T., Brunold, T. C., Telser, J., *J. Am. Chem. Soc.* **2004,** 126, 2148–2155.
39. Brueggemann, W., Niklas, J. R., Stochastic ENDOR. *Journal of Magnetic Resonance, Series A.* **1994,** 108, (1), 25-29.
40. Morse, P. D., II *EPR Data Acquisition System*, 2.41A - ENDOR; Scientific Software Services: Bloomington, IL 61701, 1987-1993.
41. Walsby, C. J.; Krepkiy, D.; Petering, D. H.; Hoffman, B. M., Cobalt-Substituted Zinc Finger 3 of Transcription Factor IIIA: Interactions with Cognate DNA Detected by 31P ENDOR Spectroscopy. *Journal of the American Chemical Society* **2003,** 125, (25), 7502-7503.
42. Hoffman, B. M., DeRose, V. J., Doan, P. E., Gurbiel, R. J., Houseman, A. L. P., Telser, J., EMR of Paramagnetic Molecules. In *Biological Magnetic Resonance, Vol. 13: EMR of Paramagnetic Molecules*, Berliner, L. J., Reuben, J., Ed. Plenum: New York, 1993.
43. Werst, M. M.; Davoust, C. E.; Hoffman, B. M., Ligand spin densities in blue copper proteins by q-band proton and nitrogen-14 ENDOR spectroscopy. *Journal of the American Chemical Society* **1991,** 113, (5), 1533-1538.
44. Usov, O. M.; Choi, P. S. T.; Shapleigh, J. P.; Scholes, C. P., ENDOR of NO-Ligated Cytochrome c'. *Journal of the American Chemical Society* **2006,** 128, (15), 5021-5032.
45. Usov, O. M.; Choi, P. S. T.; Shapleigh, J. P.; Scholes, C. P., ENDOR Investigation of the Liganding Environment of Mixed-Spin Ferric Cytochrome c'. *Journal of the American Chemical Society* **2005,** 127, (26), 9485-9494.
46. Veselov, A. V.; Osborne, J. P.; Gennis, R. B.; Scholes, C. P., Q-Band ENDOR (Electron Nuclear Double Resonance) of the High-Affinity Ubisemiquinone Center in Cytochrome bo3 from Escherichia coli. *Biochemistry* **2000,** 39, (11), 3169-3175.
47. Sienkiewicz, A., Smith, B. G., Veselov, A., Scholes, C. P., , Tunable Q-band resonator for low temperature electron paramagnetic resonance / electron nuclear double resonance. . *Rev. Sci. Instrum.* **1996,** 67, 2134-2138.
48. Hoffman, B. M., Gurbiel, R. J., *J. Magn. Reson.* **1989,** 82, 309-317.
49. Van Camp, H. L., Sands, R. H., Fee, J. A., Electron-nuclear double resonance on copper (II) tetraimidazole. *J. Chem. Phys.* **1981,** 75, 2098-2107.
50. Doan, P. E. *GENDOR*, 2.3; Evanston, IL, 2004.
51. Neese, F., Personal Communication. In 2008.
52. Hartree, D. R., Hartree, W., *Proceedings of the Royal Society (London), Series A* **1949,** 193, 299-304.
53. Weil, J. A., Bolton, J. R., Wertz, J. E., *Electron Paramagnetic Resonance*. Wiley: New York, 1994.
54. Stoll, S., Schweiger, A., EasySpin, a comprehensive software package for spectral simulation and analysis in EPR. *Journal of Magnetic Resonance* **2006,** 178, 42-55.
55. Claridge, T. D. W., *High-Resolution NMR Techniques in Organic Chemistry*. Pergamon: New York, 1999; Vol. 19.
56. Weber, R. T., Magnetic Stability. In Myers, W. K., Ed. Billerica, MA, 2008.
57. Sternlicht, H., Nuclear Relaxation Induced by Paramagnetic Ions Having Anisotropic g Factors. *J. Chem. Phys.* **1965,** 42, 2250.
58. Bertini, I., Luchinat, C., Mancini, M., Spina, G., *J. Magn. Reson.* **1984,** 59, 213.

59. Gueron, M., *J. Magn. Reson.* **1975,** 19, 58.
60. Dahlin, S., Reinhammar, B., Angstrom, J., Proton-Metal Distance Determination in Cobalt(II) Stellacyanin by 1H Nuclear Magnetic Resonance Relaxation Measurements Including Curie-Spin Effects: A Proposed Structure of the Metal-Binding Region. *Biochemistry* **1989,** 28, 7224-7233.
61. Swift, T. J., Connick, R. E., NMR-Relaxation Mechanisms of 17O in Aqueous Solutions of Paramagnetic Cations and the Lifetime of Water Molecules in the First Coordination Sphere. *The Journal of Chemical Physics* **1962,** 37, (2), 307-320.
62. Riley, E. A.; Petros, A. K.; Smith, K. A.; Gibney, B. R.; Tierney, D. L., Frequency-Switching Inversion-Recovery for Severely Hyperfine-Shifted NMR: Evidence of Asymmetric Electron Relaxation in High-Spin Co(II). *Inorganic Chemistry* **2006,** 45, (25), 10016-10018.
63. Bertini, I. G., C.; Luchinat, C.; Parigi, G., A computer program for the calculation of paramagnetic enhancements of nuclear-relaxation rates in slowly rotating systems. *J. Magn. Reson. Ser. A* **1995,** 113, (1995), 151-158.
64. Sharp, R. R., Nuclear-spin relaxation in paramagnetic solutions when the electronic zero-field splitting and Zeeman interactions are of arbitrary magnitude. *J. Magn. Reson.* **1992,** 100, 491-516.
65. Schaefle, N., Sharp, R., Four complementary theoretical approaches for the analysis of NMR paramagnetic relaxation. *J. Magn. Reson.* **2005,** 176, 160-170.
66. Abragam, A., Bleaney, B., *Electron Paramagnetic Resonance of Transition Ions*. 2 ed.; Clarendon Press: Oxford, 1970.